Monthly Notices
of the
ROYAL ASTRONOMICAL SOCIETY

MNRAS **543,** 3249–3302 (2025) https://doi.org/10.1093/mnras/staf1540

The dawn of discs: unveiling the turbulent ionized gas kinematics of the galaxy population at $z \sim 4$–6 with *JWST*/NIRCam grism spectroscopy

A. Lola Danhaive[1,2★] Sandro Tacchella[1,2] Hannah Übler[3] Anna de Graaff[4] Eiichi Egami[5] Benjamin D. Johnson[6] Fengwu Sun[5] Santiago Arribas[7] Andrew J. Bunker[8] Stefano Carniani[9] Gareth C. Jones[1,2] Roberto Maiolino[1,2] William McClymont[1,2] Eleonora Parlanti[3,9] Charlotte Simmonds[1,2] Natalia C. Villanueva[10] William M. Baker[11] Daniel T. Jaffe,[10] Daniel Eisenstein[6] Kevin Hainline[5] Jakob M. Helton[5] Zhiyuan Ji[5] Xiaojing Lin[12] Yichen Liu[5] Dávid Puskás[1,2] Marcia Rieke[5] Pierluigi Rinaldi[5] Brant Robertson[13] Jan Scholz[1,2] Christina C. Williams[14] and Christopher N. A. Willmer[5]

[1] *Kavli Institute for Cosmology, University of Cambridge, Madingley Road, Cambridge CB3 0HA, UK*
[2] *Cavendish Laboratory, University of Cambridge, 19 JJ Thomson Avenue, Cambridge CB3 0HE, UK*
[3] *Max-Planck-Institut für extraterrestrische Physik (MPE), Gießenbachstraße 1, D-85748 Garching, Germany*
[4] *Max-Planck-Institut für Astronomie, Königstuhl 17, D-69117 Heidelberg, Germany*
[5] *Steward Observatory, University of Arizona, 933 N. Cherry Avenue, Tucson, AZ 85721, USA*
[6] *Center for Astrophysics | Harvard & Smithsonian, 60 Garden St, Cambridge, MA 02138, USA*
[7] *Centro de Astrobiología (CAB), CSIC-INTA, Cra. de Ajalvir Km. 4, E-28850, Torrejón de Ardoz, Madrid, Spain*
[8] *Department of Physics, University of Oxford, Denys Wilkinson Building, Keble Road, Oxford OX1 3RH, UK*
[9] *Scuola Normale Superiore, Piazza dei Cavalieri 7, I-56126 Pisa, Italy*
[10] *Department of Astronomy, The University of Texas at Austin, 2515 Speedway, Stop C1400, Austin, TX 78712-1205, USA*
[11] *DARK, Niels Bohr Institute, University of Copenhagen, Jagtvej 128, DK-2200 Copenhagen, Denmark*
[12] *Department of Astronomy, Tsinghua University, Beijing 100084, China*
[13] *Department of Astronomy and Astrophysics, University of California, Santa Cruz, 1156 High Street, Santa Cruz, CA 95064, USA*
[14] *NSF National Optical-Infrared Astronomy Research Laboratory, 950 North Cherry Avenue, Tucson, AZ 85719, USA*

Accepted 2025 September 9. Received 2025 September 9; in original form 2025 April 8

ABSTRACT

Recent studies of gas kinematics at high redshift have reported discy systems that appear to challenge models of galaxy formation, but it is unclear whether they are representative of the underlying galaxy population. We present the first statistical sample of spatially resolved ionized gas kinematics at high redshift, comprised of 213 H α emitters in GOODS-S and GOODS-N at redshifts $z \approx 3.9$–6.5, observed with *James Webb Space Telescope*/NIRCam slitless spectroscopy and imaging from JADES, FRESCO, and CONGRESS. The sample probes two orders of magnitude in stellar mass ($\log(M_\star[\mathrm{M}_\odot]) \approx 8$–10) and star formation rate (SFR ≈ 0.3–$100\,\mathrm{M}_\odot\,\mathrm{yr}^{-1}$), and is representative down to $\log(M_\star[\mathrm{M}_\odot]) \approx 9$. Using a novel inference tool, GEKO, we model the grism data to measure morphological and kinematic properties of the ionized gas, as probed by H α. Our results are consistent with a decrease of the rotational support v/σ_0 and increase of the velocity dispersion σ_0 with redshift, when compared to $z < 3$, with $\sigma_0 \approx 100\,\mathrm{km\,s^{-1}}$ and $v/\sigma_0 \approx 1$–2 at $z \approx 3.9$–6.5. We study the relations between σ_0 and v/σ_0, and different star formation tracers and find a large scatter and diversity, with the most significant correlation between σ_0 and SFR. We find no evolution of the fraction of rotationally supported systems ($v/\sigma_0 > 1$) from $z \sim 5.5$ to $z \sim 4.5$, measured at $f = (34 \pm 5)$ per cent in both redshift bins, for galaxies with masses $9 < \log(M_\star[\mathrm{M}_\odot]) < 10$. Overall, discs do not dominate the turbulent high-redshift galaxy population in the mass range probed by this work, but they remain a sizeable population. When placed in the context of studies up to cosmic noon, our results are consistent with a needed increase of disc-like systems with cosmic time.

Key words: galaxies: evolution – galaxies: high-redshift – galaxies: kinematics and dynamics – galaxies: structure.

1 INTRODUCTION

In the Lambda cold dark matter framework, galaxy evolution is driven by four key processes: the accretion of cold gas, the formation of stars from the collapse of the gas, the feedback from both stars and black holes, and galaxy–galaxy mergers. The morphology and kinematics

---

★ E-mail: ald66@cam.ac.uk

of a galaxy trace these processes and are hence deeply connected to the galaxy's evolutionary stage and mass assembly history. In this work, we focus on constraining the kinematics and stellar populations of galaxies in the first 2 Byr of the Universe's history (redshifts $z = 3.9$–6.5) to shed new light on to the interplay between these different physical processes in the assembly of galaxies.

In the simple analytical models of galaxy formation, gas flows into the centre of dark matter haloes and cools to form stars. The gas conserves most of its angular momentum as it falls into the halo, approximately reflecting the size of the halo at the time of accretion. This means that gas cooling at later times will have higher angular momentum and settle further out into an extended star-forming disc (Fall & Efstathiou 1980; Mo, Mao & White 1998). This formalism implies that galaxies are expected to grow from the inside-out, with new stars forming in the disc.

Beyond this simple model, feedback from stars and black holes also plays an important role in regulating star formation. Stars inject momentum into the interstellar medium (ISM) through supernovae, stellar winds, and radiation pressure (Ostriker & Shetty 2011; Newman et al. 2012; Shetty & Ostriker 2012; Rathjen et al. 2023). These processes heat and disrupt surrounding gas, and sufficiently strong feedback can drive strong outflows, which eject gas from the galaxy entirely (Oppenheimer & Davé 2008; Oppenheimer et al. 2010; Brook et al. 2012; Übler et al. 2014). Such processes redistribute gas and affect the kinematics of cold (≈ 100 K, e.g. CO and [C II]) and, in particular, warm ionized ($\approx 10^4$ K, e.g. H α and [O III]) gas. Similarly, the accretion of baryons on to a nuclear supermassive black hole, hence triggering an active galactic nucleus (AGN), can generate powerful outflows and heavily disrupt the star formation and dynamics of its host galaxy (Silk & Rees 1998; Cattaneo et al. 2009; Kormendy & Ho 2013; Reines & Volonteri 2015; Harrison 2017; Florian et al. 2020; D'Eugenio et al. 2024; Oh et al. 2024). Furthermore, complex processes such as the formation of dust (Inoue 2011; Marshall et al. 2022; Matharu et al. 2023; Le Bail et al. 2024; Li et al. 2024; Schneider & Maiolino 2024) and metals (Mannucci et al. 2010; Wuyts et al. 2016a; Simons et al. 2021; Sharda et al. 2021; Boardman et al. 2023; Venturi et al. 2024), galaxy–galaxy interactions and mergers (Wright et al. 2009; Qu et al. 2010; Duan et al. 2024; Nakazato, Ceverino & Yoshida 2024; Puskás et al. 2025), and violent gas inflows (Dekel et al. 2009; Klessen & Hennebelle 2010; Gabor & Bournaud 2014; Forbes et al. 2023) can affect the morphology and kinematics of the galaxy by introducing clumpy star formation and turbulence (van den Bosch 2001; Bournaud, Elmegreen & Elmegreen 2007; Mandelker et al. 2017; Oklopčić et al. 2017). These effects are especially important at early cosmic times when the gas fractions and overall densities are higher, causing more intense star formation, and galaxies have lower stellar masses, and are therefore less resistant to feedback processes due to their shallow potential wells (El-Badry et al. 2016; Hopkins et al. 2023). Such effects are thought to be the cause of the highly variable, or 'bursty', star formation, which has been identified at high redshift (Tacchella et al. 2023; Endsley et al. 2024; Looser et al. 2024; Baker et al. 2025b; McClymont et al. 2025a; Witten et al. 2025). The direct impact of bursty star formation on the kinematics has not been directly studied; however, it has been associated with massive gas inflows and outflows on short time-scales (Tacchella, Forbes & Caplar 2020; Zhu et al. 2025; McClymont et al. 2025a; Saldana-Lopez et al. 2025) and rapid morphological evolution, including the fluctuations of galaxy sizes (El-Badry et al. 2016; McClymont et al. 2025b), implying that the impact on kinematics is likely important.

Observational studies of the local Universe paint a picture of a variety of galaxy dynamical states and morphologies, which are outcomes of their complex mass assembly history (Sales et al. 2012; Dubois et al. 2016; Tacchella et al. 2016b, 2019). Galaxies are often separated into two broad categories – star-forming spiral disc galaxies with younger stellar populations and bulge-dominated quiescent galaxies with older stellar populations (e.g. Hubble 1926; Kormendy & Kennicutt 2004; Simard et al. 2011). However, various dynamical studies have shown that the picture is more complex, with the kinematics and morphology not always tracing the state of star formation. This can be seen through the structural and dynamical variety of early-type galaxies, which are made up of both fast and slow rotators (e.g. review by Cappellari 2016), in part due to environmental effects (Barsanti et al. 2025; Foster et al. 2025).

The theoretical framework outlined above allows us to reproduce well the large population of $M_* = 10^{9-11}\,\mathrm{M}_\odot$ disc galaxies found in the local Universe (van der Wel et al. 2014; Zhu et al. 2018; Wang et al. 2020; Rigamonti et al. 2024). Studies of both ionized and molecular gas kinematics find that these star-forming discs are characterized by high rotational support and low velocity dispersions of the order of 10–20 $\mathrm{km\,s^{-1}}$ (Dib, Bell & Burkert 2006; Walter et al. 2008; Tacconi et al. 2013; Yu et al. 2019). Studies of stellar kinematics, the key tracer of mass assembly history, have found trends with stellar age, mass, and environment, where age seems the strongest (e.g. Croom et al. 2024). This supports the idea that the young stellar populations in star-forming discs have low stellar velocity dispersions compared to the older bulge-dominated elliptical systems (Cappellari et al. 2007, 2011; Emsellem et al. 2007; Krajnović et al. 2011; Naab et al. 2014; van de Sande et al. 2018), although quiescent galaxies have been found in a variety of kinematic states (Bezanson et al. 2018; Newman et al. 2018; Ji et al. 2024). Studies of stellar kinematics at high redshift are difficult due to detection limits of current observational facilities, with current measurements reaching $z \approx 2$–3 (Newman, Belli & Ellis 2015; D'Eugenio et al. 2024).

The studies from the local Universe out to cosmic noon (at $z \sim 1$–3) agree that star-forming discs grow inside out at these epochs (Muñoz-Mateos et al. 2007; Wuyts et al. 2011; van der Wel et al. 2014; Nelson et al. 2016; Ji & Giavalisco 2023), which aligns with predictions from theoretical models and cosmological simulations (Mo et al. 1998; Hasheminia et al. 2024). However, the picture becomes more complex at cosmic noon, where the bulk of the cosmic star formation occurs (Madau & Dickinson 2014). Star-forming discs exist at these epochs but they are less massive, more turbulent, thicker, and more gas-rich than in the local Universe (Genzel et al. 2017; Förster Schreiber & Wuyts 2020; Tacconi, Genzel & Sternberg 2020), and kinematic studies have shown that they are characterized by a range of dark matter profiles (Genzel et al. 2020; Bouché et al. 2022; Nestor Shachar et al. 2023). Furthermore, these star-forming galaxies have significant bulges in their cores and their specific star formation rate (sSFR) radial profiles are roughly flat, indicating little inside-out growth on average (Tacchella et al. 2015; Mosleh et al. 2020; Jain, Tacchella & Mosleh 2024).

Spatially resolved studies of ionized gas kinematics have shown that the median rotational support v/σ_0[1] of galaxies decreases with redshift, while the intrinsic velocity dispersion σ_0 increases, from $\sigma_0 \sim 10$–$20\ \mathrm{km\,s^{-1}}$ to average values of $\sigma_0 \sim 50\ \mathrm{km\,s^{-1}}$ at $z \sim 2.5$ (Wisnioski et al. 2015, 2019; Price et al. 2016, 2020; Simons et al. 2017; Turner et al. 2017b; Übler et al. 2019) with some systems going up to $\sigma_0 \sim 100\ \mathrm{km\,s^{-1}}$. Some works find that the higher turbulence is mainly driven by gravitational instabilities in the disc,

---

[1] We discuss our definitions of v/σ_0 and σ_0 in Section 3.4.2.

with a less important role of stellar feedback (Krumholz et al. 2018; Übler et al. 2019), while others report that stellar feedback alone is sufficient to explain the measured turbulence in cold gas kinematics across redshifts (Rizzo et al. 2024). Many works find a dependence of σ_0 on global SFR (Arribas et al. 2014; Wisnioski et al. 2015; Simons et al. 2016; Yu et al. 2019; Price et al. 2020), while the relationship with the SFR surface density $\Sigma_{\rm SFR}$ is more debated. Some studies show that the correlation with $\Sigma_{\rm SFR}$ is stronger than with SFR (Varidel et al. 2020; Mai et al. 2024), but others highlight no local dependence of σ_0 on $\Sigma_{\rm SFR}$, whose detection would strongly support a scenario of stellar feedback-induced turbulence (Übler et al. 2019). However, most works agree on the large scatter in the σ_0–z relation, which could be caused by the non-disc systems probing different origins of turbulence (including mergers) from their rotationally supported disc counterparts. Some of the increase in the measured σ_0 could also be explained by an increased contribution of diffuse ionized gas, which typically has higher σ_0 than gas emitted from H II regions (Della Bruna et al. 2020), to the H α flux at high redshift (Ejdetjärn et al. 2024).

All of these works highlight the importance of linking resolved studies of star formation to the stellar and gas kinematics of galaxies. Studying the dependence of σ_0 and v/σ_0 on both redshift and physical galaxy properties such as SFR and its evolution with cosmic time beyond $z > 3$ is crucial to understand when and how galaxies settle into rotationally supported systems.

Many galaxy simulations predict that, on average, disc galaxies only become prominent at $z < 4$ (Zolotov et al. 2015; Pillepich et al. 2019; Lapiner et al. 2023; Hopkins et al. 2023; Semenov et al. 2024c), but observations in the last decade, first with the Atacama Large Millimeter Array (ALMA), and now with the *James Webb Space Telescope* (*JWST*), have unveiled a different picture. Studies of molecular gas kinematics with ALMA have found dynamically cold (typically $v/\sigma_0 \gtrsim 4$) discs out to $z \sim 6$ (Rizzo et al. 2020; Lelli et al. 2021; Pope et al. 2023), with a $v/\sigma_0 \sim 11$ system found as early as $z = 7.31$ (Rowland et al. 2024). Studies of ionized gas kinematics are now possible out to similar redshifts, and down to lower masses ($\log(M_\star[{\rm M}_\odot]) < 9$) and SFR regimes, with *JWST*, both with the NIRSpec integral field unit (IFU) and slit spectrograph (e.g. Arribas et al. 2024; de Graaff et al. 2024a; Übler et al. 2024), and with NIRCam slitless spectroscopy (Li et al. 2023; Nelson et al. 2023). Taken at face value, these studies imply that galaxies are able to settle into cold discs much earlier than many models are able to explain. However, it is unclear whether these studies probe a representative sample of star-forming galaxies.

None the less, recent theoretical work has explored mechanisms to generate discs at high redshift, and some simulations have been successful in promoting the formation of discs beyond $z \sim 4$ through smooth accretion of cold gas from the cosmic web filaments (Feng et al. 2015; Kohandel et al. 2024) and high resolution on-the-fly modelling of the cold ISM (Semenov et al. 2025a; Semenov, Conroy & Hernquist 2025b). While such efforts are encouraging, it is now crucial to understand the kinematics of high-redshift galaxies with representative statistics in order to inform the next generation of models. While purely morphological studies support this idea, with disc-like morphologies found out to $z \sim 7$ (Ferreira et al. 2022, 2023; Robertson et al. 2023; Tohill et al. 2024; Baker et al. 2025a), there has thus far been no systemic study of ionized gas kinematics on a large galaxy sample beyond $z = 4$.

The NIRCam grism mode offers a unique opportunity to address the questions arising from these recent results in a statistically significant way. Its $R \sim 1600$ ($\Delta v = 80\,{\rm km\,s^{-1}}$ at $\lambda = 3 - 5\,\mu$m) spectral resolution allows for the study of kinematic signatures in the resolved 2D spectra. This mode is only available in the long-wavelength filters, yielding a spatial resolution of ≈ 0.12–0.16 arcsec (≈ 0.9 kpc at $z \approx 5$). One of the main benefits of slitless spectroscopy is that each exposure contains spectra for all of the galaxies in the instrument's field of view, resulting in a (relatively) unbiased large sample of galaxies to analyse (e.g. Covelo-Paz et al. 2025). This is in contrast with slit spectrographs such as the NIRSpec micro-shutter assembly (MSA), which can benefit from greater sensitivity and higher spectral resolution, with point source resolution up to $R \sim 4000$–5000 (de Graaff et al. 2024a), and lower sky background noise, but covers fewer galaxies, which are also usually specifically selected, introducing a bias that is hard to quantify. Also, the slit typically only covers part of a galaxy. However, recent efforts in using slit-stepping strategies with the NIRSpec MOS have been shown to produce integral field spectrograph (IFS) data with a significant gain in efficiency over the NIRSpec IFU (Barišić et al. 2025; Ju et al. 2025). The latter benefits from high spatial resolution (≈ 0.1–0.2 arcsec) pixel-by-pixel spectra that provide resolved constraints on the kinematics of the galaxy, ideal for detailed studies of interesting systems (e.g. Arribas et al. 2024; Jones et al. 2024; Parlanti et al. 2024; Übler et al. 2024). However, the IFU's limited field of view generally implies that these studies are restricted to single objects, or relatively small samples. In order to push our understanding of if and how discs form at high redshift, the large samples offered by the NIRCam grism are crucial in order to place single/few object observations with NIRSpec MOS and IFU into a broader picture.

In this paper, we present a systematic study of ~ 250 H α emitters at $z = 3.9$–6.5 found in the First Reionization Epoch Spectroscopically Complete Observations survey (FRESCO; Oesch et al. 2023, PI: Oesch, PID: 1895), in both GOODS fields (Giavalisco et al. 2004), and the COmplete Nircam Grism REdShift Survey (CONGRESS, PIs: Egami, Sun, PID: 3577), in the GOODS-N field. We use a new tool, the Grism Emission-line Kinematics tOol (GEKO; Danhaive et al. in preparation), to combine NIRCam *F444W* grism measurements with NIRCam multiband imaging from the *JWST* Advanced Deep Extragalactic Survey (JADES; Bunker, NIRSPEC Instrument Science Team & JADESs Collaboration 2020; Rieke 2020; Eisenstein et al. 2023, PIs: Rieke and Lützgendorf) in order to infer morphological and kinematic constraints on the H α emission for each galaxy in the sample.

This paper is organized as follows. The data and their reduction are presented in Section 2, along with the description of the sample selection. In Section 3, we introduce GEKO and outline the techniques used to forward-model the NIRCam grism instrument and infer the spatially resolved kinematics of an emission line using a Bayesian inference framework and well-motivated choices of analytical models for the morphology and kinematics of the galaxy. We present our results on the redshift evolution of ionized gas and its relation to stellar populations in Section 4, analysing the observed trends and comparing them to studies at lower redshift. Finally, we interpret our results in the context of the fraction of rotationally supported systems and the build-up of discs with cosmic time (Section 5), and we summarize our findings in Section 6. Throughout this work we assume $\Omega_0 = 0.315$ and $H_0 = 67.4\,{\rm km\,s^{-1}\,Mpc^{-1}}$ (Planck Collaboration VI 2020).

2 OBSERVATIONS AND FINAL SAMPLE

We will begin by describing the data used in this work, along with its reduction, then proceed to outline the selection criteria used to obtain our final sample.

2.1 NIRCam grism

In this work, we use *JWST*/NIRCam wide field slitless spectroscopy (WFSS) observations in the $F444W$ filter (3.9–5.0 µm) in both GOODS fields obtained with FRESCO (Oesch et al. 2023) and in the $F356W$ filter (3–4 µm) with CONGRESS (PIs: Egami, Sun, PID: 3577) in GOODS-N. The observations for both surveys are all taken using the row-direction grisms (GRISMR mode) with modules A and B, and the spectral resolution is $R \sim 1400$–1650 across the filters used.

The data reduction for these observations is described in detail in Sun et al. (2023b) and Helton et al. (2024a), so we will only provide a brief overview here. The raw data are first reduced to stage-1 products using the standard *JWST* pipeline. The stage-1 data are corrected by flat-fields and the sigma-clipped median sky background is subtracted from each individual exposure, and a world coordinate system is assigned. We then use the corresponding long wavelength (LW) images taken after each grism exposure to assign every trace to an object and hence apply wavelength calibration to the 2D spectra of each galaxy. The LW images are astrometrically calibrated using the simultaneous short wavelength exposures taken in parallel with the grism. The spectral tracing, grism dispersion, and sensitivity functions are obtained from commissioning and Cycle-1 calibration data (PID: 1076, 1536, 1537, 1538; Sun et al. 2022, 2023b). In order to obtain 2D continuum-subtracted emission-line maps from the grism data, we use row-by-row median filtering (Kashino et al. 2023) in order to remove residual continuum from the object itself and any neighbouring objects that may leave traces in the spectrum. The two-step (iterative) median filtering used in this technique aims to ensure that the continuum is accurately removed but the emission-line flux is not harmed.

Due to the ~ 3–5 µm range probed by the FRESCO and CONGRESS surveys, we are able to study star-forming galaxies, through their H α emission, at $z \approx 3.9$–6.5. Our sample is built following the technique from Helton et al. (2024a) and Sun et al. (2024) to accurately search for H α emitters at these redshifts. First, photometric redshifts are estimated using EAZY (Brammer, van Dokkum & Coppi 2008) using the templates and parameters described in Helton et al. (2024a) and Hainline et al. (2024). We select sources based on their EAZY photometric redshifts z_{phot} and confidence intervals $\Delta z_{\mathrm{phot}} < 1$, then extract their grism spectrum following the method outlined above. The extracted 2D spectra are then collapsed to 1D spectra using a boxcar aperture of 0.31 arcsec (five NIRCam LW pixels). For high signal-to-noise S/N>5 detections, we assign an emission-line solution that minimizes the difference between the spectroscopic and photometric redshifts, then perform visual inspection to confirm the redshifts. For the final H α emitter catalogue, the 1D spectra are optimally extracted with Gaussian profiles to obtain accurate spectroscopic redshifts, emission-line fluxes, and their corresponding integrated S/N. We find good agreement with the catalogue described in Covelo-Paz et al. (2025), used to obtain the H α luminosty function at $z \sim 4$–6.5 from FRESCO and CONGRESS. We obtain 393 galaxies in CONGRESS and 189 in FRESCO that have H α detections verifying S/N > 10, for a total of 582 emitters (Helton et al. 2024b, Lin et al., in preparation).

2.2 NIRCam imaging

There is a wealth of NIRCam data in the GOODS fields. The FRESCO and CONGRESS grism programs obtained parallel imaging data in the $F182M$ and $F210M$, and $F090W$ and $F115W$ filters, respectively. In addition, the FRESCO and CONGRESS footprints have a large overlap with JADES (Eisenstein et al. 2023; Rieke et al. 2023), a Guaranteed Time Observations (GTO) programme of the NIRCam and NIRSpec instrument teams that obtained imaging of an area of ~ 175 arcmin^2 in the GOODS-S and GOODS-N fields with an average exposure time of 20 h with 8–10 filters. For 497 out of the 582 galaxies in our S/N > 10 sample, we were able to complement the FRESCO and CONGRESS imaging with wide band $F090W$, $F115W$, $F150W$, $F200W$, $F277W$, $F356W$, and deeper $F444W$ observations, and medium band $F335M$ and $F410M$ observations from JADES. For certain regions in our sample, we also use additional medium bands $F182M$, $F210M$, $F430M$, $F460M$, and $F480M$ from the JWST Extragalactic Medium Band Survey (JEMS; Williams et al. 2023) in GOODS-S. Specifically, we use high-resolution data and photometric catalogues obtained from drizzled mosaics, and the full details on the data reduction, catalogue generation, and photometry can be found in Rieke et al. (2023), and are also detailed in Robertson et al. (2024). This wide range of filters allows us to obtain tight constraints on the stellar population from spectral energy distribution (SED) fitting (Section 3.1) and accurate morphology priors for our inference tool (Section 3.4).

Table 1. Summary of the sub-samples defined in this work and their selection criteria. The extended sample is a sub-sample of the gold and silver samples. For each category, we report the number of galaxies N it contains, the S/N cut-off, the morphological PA $\mathrm{PA_{morph}}$ cut-off, and the size r_{e} requirement. We add constraints on whether the velocity gradient at r_{e} has to be resolved, $\frac{v_{\mathrm{re}}}{\Delta v_{\mathrm{re}}} > 1$, where $\Delta v(r = r_{\mathrm{e}})$ is the 1σ lower limit, and constraints regarding the extent r_{obs} of the observed grism emission-line map.

Sample	N	S/N	$\lvert\mathrm{PA_{morph}}\rvert$ (°)	r_{e} (arcsec)	$\frac{v_{\mathrm{re}}}{\Delta v_{\mathrm{re}}}$	r_{obs}
Gold	37	> 20	< 60	> 0.12	> 1	$> r_{\mathrm{e}}$
Silver	126	> 10	< 75	> 0.12	> 1	–
Unresolved	50	> 10	< 75	–	–	–
Extended	133	> 10	< 75	> 0.12	> 1	$> r_{\mathrm{e}}$

2.3 Sample selection

From the emission-line catalogue described above, there are > 1000 H α detections in the FRESCO and CONGRESS grism data. We introduce an S/N cut for the integrated H α emission of S/N > 10, following recovery tests done on mock data (Danhaive et al. in preparation), narrowing the sample down to to a total of 582 galaxies. Below this S/N, we are not able to reliably constrain key kinematic properties σ_0 and v/σ_0, as we discuss in Appendix E (see Fig. E1), where we present results from the testing process of our tool GEKO (Section 3.3). We then introduce additional cuts to separate our final sample into three categories, which are summarized in Table 1 and described below:

(i) *Gold sample:* This is the sample containing the galaxies for which we have the most reliable constraints. These galaxies have high integrated H α S/N (S/N > 20) and have a position angle (PA) distinct from the dispersion direction (which is at $\mathrm{PA_{disp}} = 90^{\circ}$[2]): $\lvert\mathrm{PA_{morph}}\rvert < 60^{\circ}$. $\mathrm{PA_{morph}}$ is measured from the imaging data (see Section 3.2). Throughout the paper, this sample of 37 galaxies is plotted with squares.

(ii) *Silver sample:* This sample contains the galaxies with S/N ≥ 10 and has a looser PA cut $\lvert\mathrm{PA_{morph}}\rvert < 75^{\circ}$. Throughout the paper, this sample of 126 galaxies is plotted with circles.

---

[2] We adopt a convention where the PAs $\lvert\mathrm{PA_{morph}}\rvert$ and $\lvert\mathrm{PA_{kin}}\rvert$ are defined from the vertical spatial y-axis in a clockwise way.

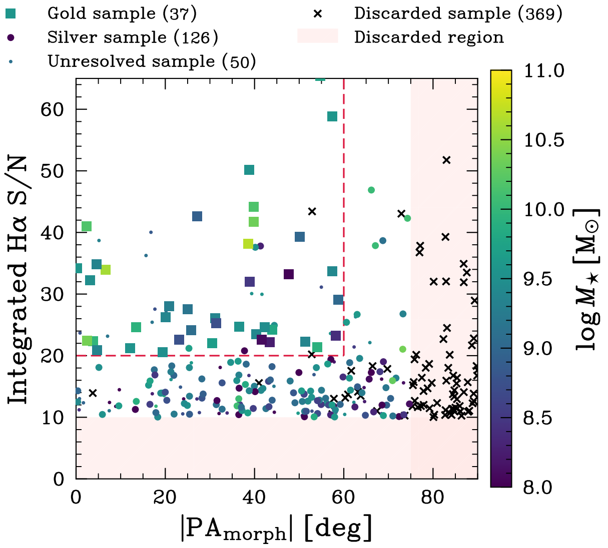

Figure 1. Selection of our sample in the plane of H α S/N and $|\mathrm{PA}_{\mathrm{morph}}|$, colour-coded by stellar mass. The discarded region highlights the parameter space in which galaxies are discarded due to low S/N and/or a PA that is too close to the dispersion direction (PA $= 90^\circ$). The S/N $= 20$ and $|\mathrm{PA}_{\mathrm{morph}}| = 60^\circ$ cut-off for the gold sample is highlighted with the red dashed line. The small dots represent the unresolved sample of galaxies that have a spatial resolution below the FWHM of the *F444W* PSF and/or for which we do not measure a resolved velocity gradient. Based on the selection cuts described in Section 2.3, we obtain 37 galaxies in the gold sample, 126 in the silver sample, and 50 in the unresolved sample (see Table 1).

(iii) *Unresolved sample:* This sample contains the galaxies whose inferred r_e is smaller than half of the full width at half-maximum (FWHM) of the *F444W* PSF and/or whose velocity gradient is unresolved, i.e. its value is consistent with zero within 1σ. We hence qualify galaxies as unresolved if $|\mathrm{v(r = r_e)}|/\Delta\mathrm{v(r = r_e)} < 1$, where $\Delta v(r = r_{\rm e})$ is the 1σ lower limit. This final cut can of course only be done after the kinematic fitting is completed (Section 3.4). This sample of 50 galaxies will be plotted with dots.

(iv) *Extended sample:* This sample contains 133 galaxies that are in the gold or silver sample and have grism data that extend beyond the best-fitting effective radius of the H α emission.

(v) *Discarded sample:* This sample of 369 galaxies is not included in the paper. It contains galaxies whose fits provided large residuals (often due to clumpy/merging morphology) and hence need further analysis. As shown on Fig. 2, the clumpy/merging sample appears evenly spread in mass and hence should not introduce biases in terms of mass or size. It also contains galaxies that are almost parallel to the dispersion direction $|\mathrm{PA}_{\mathrm{morph}}| > 75^\circ$ and therefore cannot be kinematically constrained, and galaxies with a low H α integrated S/N (S/N < 10). These cuts are all based on testing done on mock data (Danhaive et al. in preparation). Finally, we also discard galaxies whose best-fitting kinematic and morphological PAs are in disagreement $|\mathrm{PA}_{\mathrm{kin}} - \mathrm{PA}_{\mathrm{morph}}| > 30^\circ$.

The gold, silver, and unresolved categories make up a total sample of 213 H α emitters. Fig. 1 shows the separation of the sample in these categories to highlight the cuts made. In the rest of the paper, we will plot these different samples in similar ways as this plot to distinguish them. In the 393 (CONGRESS) plus 189 (FRESCO) galaxies with S/N> 10, we found (and discarded) 108 additional objects that showed a merging structure in the NIRCam imaging. These objects do not show clustering in their SFRs or stellar masses (Fig. 2), so discarding them should not impact our sample in this plane of parameter space. We discuss the impact of excluding these systems on our inferred disc fraction in Section 5.1. Additionally, 14 systems were classed as AGNs due to their broad H α emission in the NIRCam grism spectra, indicative of an AGN broad line region (BLR). Out of these AGN candidates, seven are confirmed little red dots (Matthee et al. 2024). We exclude these objects from our sample as they require multiple component modelling to account for the BLR, which is an opportunity for future study but out of the scope of this work.

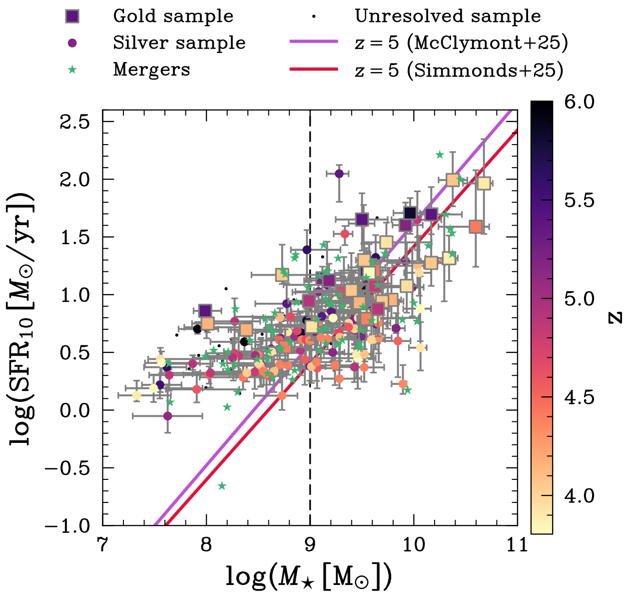

Figure 2. Star formation rates (SFR$_{10}$) and stellar masses ($M_\star$) of our sample, derived with PROSPECTOR, colour-coded by the spectroscopic redshifts. The SFRs are averaged over 10 Myr. We compare our sample to SFMS prescriptions from McClymont et al. (2025a) and Simmonds et al. (2025). Our sample is representative of the star-forming galaxy population at $M_\star > 10^9$ M$_\odot$ (indicated by the vertical dashed line). Below this stellar mass, because our sample selection is based on S/N in H α (Fig. 1), it is biased towards high SFRs relative to the SFMS. The discarded merger sample (green stars) is evenly spread across the parameter space and discarding it does not bias our results.

We obtain SFRs and stellar masses from PROSPECTOR modelling of both photometry from NIRCam imaging and emission-line fluxes from NIRCam grism (details in Section 3.1), and find that our sample is representative of galaxies on the star-forming main sequence (SFMS) at $z \sim 5$, as shown on Fig. 2, using the SFMS prescription from Simmonds et al. (2025). This SFMS is derived from PROSPECTOR modelling of JADES galaxies from $z = 3$–9, 90 per cent complete in stellar mass down to $\log(M_\star\ [\mathrm{M}_\odot]) \approx 7.5$, presented in Simmonds et al. (2024) for GOODS-S and extended to include galaxies in GOODS-N (Simmonds et al. 2025).

We also include the prescription from the THESAN-ZOOM simulations (Kannan et al. 2025), presented in McClymont et al. (2025a). Our sample lies on the relations above $M_\star \approx 10^9$ M$_\odot$, but we note that, due to our S/N cut, the low-mass end ($M_\star \lesssim 10^9$ M$_\odot$) of the SFMS is biased to systems that are brighter and hence more star-forming.

In terms of the redshift distribution of the galaxies in our sample, we show in Fig. 3 that galaxies in the lower redshift region ($3.8 < z < 5$) have more galaxies and span a wider range in stellar mass. On the other hand, the higher redshift ($5 < z < 6.5$) galaxies are, in comparison, biased to higher masses, where most gold and silver sample systems are lying above $M_\star \sim 10^9$ M$_\odot$. The effective radii, measured from rest-frame near-UV imaging, indicate that our galaxies are representative of the population at $z \sim 4$–6, consistent with Allen et al. (2025) (see also Danhaive et al. in preparation). At fixed stellar mass, galaxies span a wide range of sizes, as can be seen from the colour-coding in Fig. 3. The distribution of the UV sizes in arcseconds for the gold and silver sample galaxies (see Appendix A, Fig. A1) does not show a strong bias, although our gold sample galaxies do not probe the extended tail visible for the silver sample. Our S/N cut likely causes this bias, since at fixed stellar mass, more compact galaxies have a higher integrated S/N.

3 INFERRING STELLAR POPULATIONS, MORPHOLOGY, AND KINEMATICS

In order to obtain a global view of the objects in our sample, we combine NIRCam imaging and spectroscopy, along with a wide range of techniques, to infer the stellar populations, morphologies, and kinematics of the galaxies in our sample. In Section 3.1, we describe our SED-fitting approach with PROSPECTOR to obtain constraints on the stellar mass and SFRs. Then, we briefly introduce our method for fitting one-component Sérsic models to our data with PYSERSIC (Section 3.2) in order to characterize the galaxy's morphology. Finally, Sections 3.3 and 3.4 introduce a novel code GEKO and describes how we use it to infer key kinematic and morphological parameters for the emission lines probed by the grism data.

3.1 SED modelling

In order to characterize the stellar populations in the galaxies in our sample, we use the SED inference code PROSPECTOR (Johnson et al. 2021). We fit all of the available photometry from the JADES survey, which contains all of the NIRCam wide and some medium band filters ($F070W$, $F090W$, $F115W$, $F150W$, $F162M$, $F200W$, $F250M$, $F277W$, $F300M$, $F335M$, $F356W$, $F410M$, and $F444W$), the MIRI filters $F770W$ and $F1280W$, and in certain regions also included medium bands from the JEMS and FRESCO surveys ($F182M$, $F210M$, $F430M$, $F460M$, and $F480M$). We also use photometry from the *Hubble Space Telescope* (*HST*) Advanced Camera for Surveys (ACS) bands $F435W$, $F606W$, $F775W$, $F814W$, and $F850LP$ (the GOODS survey; Dickinson et al. 2004; Giavalisco et al. 2004). Following Tacchella et al. (2023), we self-consistently model the photometry with H α line fluxes from NIRCam grism data from the FRESCO and CONGRESS surveys, and, for FRESCO galaxies in the GOODS-N field, we also include, when detected, [O III]5007 Å, [O III]4959 Å, Hβ, and [S III]9533 Å fluxes from the CONGRESS survey.

Within PROSPECTOR, there is the option to allow for an overall rescaling of the input emission-line fluxes, in order to account for potential discrepancies in the flux calibrations of the different instruments. This rescaling factor then becomes a free parameter of the model, and a difference in calibrations would likely manifest as a similar 'constant' best-fitting factor found throughout our sample. However, we find no overarching consistent rescaling factor, meaning the best-fitting value changes significantly between objects. Because the best-fitting values for stellar masses and SFRs remain consistent within the uncertainties in both cases, with and without rescaling, we adopt the model with no rescaling. We also use the spectroscopic redshifts derived from the grism spectra to fix the redshift in the fits, which allows us to break the degeneracy between redshift and physical properties such as stellar mass.

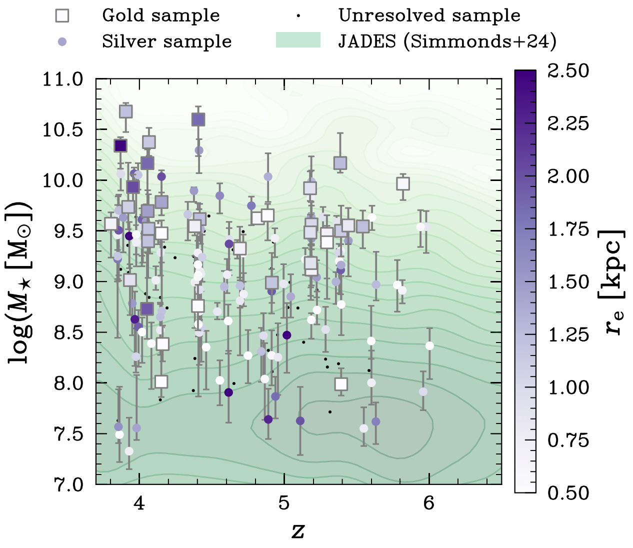

Figure 3. Distribution of our sample in the stellar mass ($M_\star$)-redshift plane. Our gold sample spans a wide range in stellar mass, but lies preferentially at $z < 5$. There are overall fewer galaxies at $z > 5$, with only few low-mass systems ($M_\star \lesssim 10^9$ M$_\odot$) falling in the gold and silver samples. Overall, our sample probes the high-mass end of photometric candidates, as shown by the green contours representative of the JADES sample from Simmonds et al. (2024, 2025), which is expected from our S/N cut. We colour-code galaxies in the gold and silver samples by their effective radius r_e in the rest-frame near-UV, highlighting that although more massive galaxies are typically larger, at fixed stellar mass, galaxies span a wide range of sizes.

In terms of priors, we assume a non-parametric continuity star formation history (SFH) prior (Leja et al. 2019) with six SFR bins. We assume a Student's t-distribution, with a width of $\sigma = 0.5$, for the ratio of the SFR in each bin, which allows for more variable SFHs than the standard continuity prior (Tacchella et al. 2022). We assume a two-component dust attenuation model (Charlot & Fall 2000; Conroy, Gunn & White 2009), where the first component (a birth-cloud component) only affects the nebular and stellar emission from young stars formed in the last 10 Myr, and the second acts on the full emission from the galaxy (a diffuse component). We use the attenuation curve from Kriek & Conroy (2013) for the diffuse dust component, where the dust bump at 2175 Å is directly coupled to the dust index n, which is modelled as an offset from the Calzetti et al. (2000) attenuation curve. We include self-consistent modelling of the nebular emission, coupling the number of Lyman-continuum photons to the SFH (Byler et al. 2017).

Using the wide range of photometry and the additional constraints from the grism data, we infer key properties such as stellar mass, SFR, and dust attenuation for all of the galaxies in our sample. PROSPECTOR also produces the best-fitting SFH for each galaxy, which can help inform us on the burstiness of star formation and the overall mass assembly history. Finally, we note that the definition of stellar mass that we use in this paper is the mass of stars and remnants, and not the full integral of the SFH. This effectively means that we correct the SFH integral by removing mass that is put back in the ISM.

3.2 Inferring morphology

In order to obtain constraints on the morphological parameters of our galaxies, we use the fully Bayesian code PYSERSIC (Pasha & Miller 2023). PYSERSIC models imaging data from any filter to infer the best-fitting Sérsic profile(s) parameters. We fit photometry in relevant filters (see Section 3.4) with a one-component Sérsic model for every galaxy in our sample to obtain estimates of the PA θ, ellipticity e, Sérsic index n, light centroid (x_0, y_0), and half-light radius r_e. We note that prior to fitting, the images from JADES (Section 2.2) are PA-matched to the grism data in order to compare the morphological PA to the dispersion direction. Also, as described in Section 3.3.1, we assume an intrinsic axis ratio q_0 when deriving the inclination from the ellipticity. Through this modelling, we are able to highlight mergers through their strong residual in single component fits. Because of how we define the PA from the vertical y-axis, we note the conversion $\mathrm{PA}_\mathrm{morph} = 90 - \theta$ deg, where θ is the PYSERSIC output angle computed from the positive x-axis.

3.3 Inferring the kinematics

In this section, we describe our methods for jointly inferring morphological and dynamical parameters from imaging and grism data using the forward-modelling and Bayesian inference tool GEKO. We follow a similar methodology to Price et al. (2016), which demonstrated such a forward modelling approach for kinematic inference with only one spatial dimension (see also Li et al. 2023; de Graaff et al. 2024a). We will summarize the main aspects of the code here, but refer to an upcoming paper for a full description of the code and testing on mock and real data (Danhaive et al., in preparation). We note that in this work, we focus on the H α emission, but this methodology can be extended to any other emission line.

3.3.1 Kinematic modelling

The simplest assumption one can make about a galaxy's kinematics is to approximate the galaxy as a thin rotating disc, which is a good assumption for the disc galaxies we observe in the local Universe. Because these exponential discs are embedded in dark matter haloes, their kinematics are well modelled by the arctangent function (Courteau 1997; Miller et al. 2011):

$$V_\mathrm{rot}(r_\mathrm{int}, r_\mathrm{t}, V_a) = \frac{2}{\pi} V_a \arctan \frac{r_\mathrm{int}}{r_\mathrm{t}}, \tag{1}$$

where V_rot is the rotational velocity at a given radius r_int in the intrinsic galaxy plane, V_a is the asymptotic value that the arctangent rotation curve tends to at large radii $r_\mathrm{int} \rightarrow \infty$, and r_t is the turn-around radius of the rotation curve. To project this velocity on the observation plane, we need to account for the galaxy's inclination i:

$$V_\mathrm{obs}(x, y) = V_\mathrm{rot}(r_\mathrm{int}, r_\mathrm{t}, V_a) \cdot \sin i \cdot \cos \phi_\mathrm{int}, \tag{2}$$

where ϕ_int is the polar angle coordinate in the galaxy plane. Because galaxies are thought to be thicker at high-redshift (van der Wel et al. 2014), we compute the inclination assuming an intrinsic disc axis ratio, which is the ratio of scale height to scale length, $(b/a)_0 = q_0 = 0.2$ (Wuyts et al. 2016b; Genzel et al. 2017; Price et al. 2020; Übler et al. 2024), where $q_0 = 0$ corresponds to the thin disc approximation. This gives for the inclination i

$$\cos i = \left(\frac{q^2 - q_0^2}{1 - q_0^2} \right)^{1/2}, \tag{3}$$

where $q = b/a$ is the measured axis ratio. We note that the choice of q_0 between common values of $q_0 = 0.0 - 0.2$ does not strongly affect the inferred kinematics properties (Förster Schreiber & Wuyts 2020; Price et al. 2020). Our choice of $q_0 = 0.2$ can cause an overestimation of the velocities by $1 - 13$ per cent for true values $q_0 = 0.25 - 0.50$. We model a constant isotropic velocity dispersion σ_0 across the disc based on deep adaptive optics imaging spectroscopy studies at lower redshift (Genzel et al. 2008; Förster Schreiber et al. 2018). Although some high-resolution observations of molecular and atomic gas in the local Universe have shown radially declining velocity dispersions, the observed radial changes are well below the NIRCam grism spectral resolution (for a more detailed discussion see Übler et al. 2019, and references therein). We also introduce a velocity offset v_0, which acts as an effective redshift offset in the observed wavelength of H α by shifting the full 2D emission-line map. For this disc model, the free parameters are therefore the inclination i, the PA PA_kin, the asymptotic velocity V_a, the turn-around radius r_t, the intrinsic velocity dispersion σ_0, and the net velocity offset v_0. We fix the centre of the velocity map to the centre of the light distribution (x_0, y_0), which is fit simultaneously to the kinematics (Table 2). It is important to note that no assumption is made on the nature of the gravitational support (rotation or pressure). The only assumption we do is that the gaseous disc is infinitely thin, without any constraint on the amplitude of the velocities or velocity dispersions.

3.3.2 Morphological modelling

In order to model the flux distribution of the chosen emission line, GEKO has a parametric and non-parametric option. For the scope of this study, the parametric flux modelling was chosen due to the small observed sizes of our galaxies ($r_{e,\mathrm{H}\alpha} \lesssim 3$ kpc), and we will not expand on the non-parametric model here. We parametrize the flux distribution with a Sérsic profile (Sersic 1968):

$$I(r) = I_e \exp\left(-b_n \left[\left(\frac{r}{r_\mathrm{e}} \right)^{1/n} - 1 \right] \right), \tag{4}$$

where I_e is the intensity at the half-light radius r_e and n is the Sérsic index. The radius r is defined based on coordinates centred on (x_0, y_0) on the sky, which are two additional free parameters of the model. For b_n, we use the polynomial expansion from Ciotti & Bertin (1999),[3] which provides a good approximation (Graham & Driver 2005). This morphological model also needs a PA, $\mathrm{PA}_\mathrm{morph}$, which we let differ from the kinematic PA, and an inclination i, which we fix to the kinematic inclination.

In order to correctly sample the inner radii of the Sérsic profile, we oversample our model grid by a factor of 125. In general, the model space has five times the spatial resolution of the observed images and nine times the spectral resolution of the grism data. This is to ensure that we are accurately computing our models on a fine grid before sampling down to the instrument resolution.

We obtain a 3D cube $I(x_0, y_0, \lambda)$ by convolving the arctangent velocity field with our flux profile, with two spatial dimensions and one spectral dimension. This cube can then be collapsed on to the 2D detector plane, going from the high-resolution 3D model space to the low-resolution 2D observation space due to a careful forward-modelling of the instrument.

3.3.3 Instrument modelling

The next step in the forward modelling of grism data is to project our data cube $I(x, y, \lambda)$ on to the NIRCam detector plane. The instrument is defined by a well-calibrated dispersion function dx, which dictates where a pixel at position (x_0, y_0) on the image and emitting at a wavelength λ_0 will end up on the detector $x_d = x_0 + dx$ (for full

---

[3] $b(n) = 2n - 1/3 + 4/405n + 46/25515n^2 + 131/1148175n^3 - 2194697/30690717750n^4$.

Table 2. Description of morphological (top section) and kinematic parameters (bottom section) being fit as free parameters in our GEKO modelling, along with their priors. For all of the parameters p with Gaussian priors based on the Pysersic modelling, we refer to the best-fitting value as μ_p and its uncertainty σ_p.

Name	Parameter description	Prior	Prior description
$\mathrm{PA}_{\mathrm{morph}}$	PA of Hα morphology	$\mathrm{Normal}(\mu_{\mathrm{PA}}, \sigma_{\mathrm{PA}})$	Normal prior, in degrees, based on the image PYSERSIC fit results.
i	Inclination angle	$\mathrm{TruncNormal}_{[0,90]}(\mu_i, \sigma_i)$	Truncated normal prior based on the image PYSERSIC fit results for ellipticity.
A	Amplitude of brightness	$\mathrm{TruncNormal}_{[0,\infty]}(\mu_A, \sigma_A)$	Normal prior, in mJy, based on a Gaussian fit to the integrated 1D emission line.
r_{e}	Effective radius	$\mathrm{TruncNormal}_{[r_{\min}, r_{\max}]}(\mu_r, 2\cdot\sigma_r)$	Truncated normal prior in pixels based on the image PYSERSIC fit results for effective radius with boosted uncertainty.
n	Sérsic index	$\mathrm{Normal}(\mu_n, 2\cdot\sigma_n)$	Normal prior based on the image PYSERSIC fit results with boosted uncertainty.
x_0	X-coordinate of centre	$\mathrm{Normal}(\mu_{x_0}, 2\cdot\sigma_{x_0})$	Normal prior, in pixels, based on the image PYSERSIC fit results with boosted uncertainty.
y_0	Y-coordinate of centre	$\mathrm{Normal}(\mu_{y_0}, 2\cdot\sigma_{y_0})$	Normal prior, in pixels, based on the image PYSERSIC fit results with boosted uncertainty.
$\mathrm{PA}_{\mathrm{kin}}$	PA of kinematics	$\mathrm{Normal}(\mu_{\mathrm{PA}}, \sigma_{\mathrm{PA}})$	Same prior as $\mathrm{PA}_{\mathrm{morph}}$, but fit independently.
V_a	Asymptotic rotational velocity	Uniform(0, 1000)	Uniform prior from 0 to 1000 km s^{-1}, with modifiable upper limit.
σ_0	Intrinsic velocity dispersion	Uniform(0, 500)	Uniform prior from 0 to 500 km s^{-1}, with modifiable upper limit.
r_t	Turnover radius	Uniform(0, r_{e})	Uniform prior from 0 to r_{e} pixels.
v_0	Systemic velocity	Normal(0, 50)	Normal prior with mean 0 and standard deviation 50 km s^{-1}.

details, see Sun et al. 2023a). This function is calibrated for each filter/pupil/module combination. Due to the limited spectral extent of the region we are modelling (the emission line), we assume no spectral tracing, $dy = 0$. Before projecting the cube on to the detector grid $\mathrm{D}(x, y)$, we convolve it with the filter-specific point spread function, $\mathrm{PSF}(x, y)$ and the line-spread function $\mathrm{LSF}(x, y)$

$$I(x, y, \lambda) \otimes \mathrm{PSF}(x, y) \otimes \mathrm{LSF}(\lambda) \rightarrow \mathrm{D}(x, y).$$

The convolution is done in the high-dimensional 3D model space, before collapsing to the spatial x-axis and resampling the model down to the instrument resolution. We approximate the PSF in each filter using the model PSFs (mPSFs) from Ji et al. (2024) constructed by mosaicing WebbPSF models repeatedly over the field identically to our exposure mosaics and then measuring the average PSF. The model PSFs are then resample down to the grism resolution. The wavelength-dependent one-dimensional LSF is modelled as the sum of two Gaussian distributions, to account for the broader wings. It was calibrated using SMP-LMC-058, a compact planetary nebula in the LMC (see also Jones et al. 2023) using extraction from *JWST* commissioning, Cycle-1 and 2 calibration observations (Sun et al., in preparation). The spectral resolution as function of wavelength is similar to the pre-launch measurements (Greene et al. 2017). Based on the measurement for the four combination of modules (A or B) and dispersion directions (R or C), we estimate a typical error on the LSF of 10 per cent. We can now join our analytical models for galaxy morphology and kinematics with the forward modelling of the instrument in a Bayesian inference framework.

3.4 Fitting

To place the forward modelling in an inference framework, GEKO uses the Bayesian inference tool NUMPYRO (Phan, Pradhan & Jankowiak 2019), which is based on JAX, a python library tailored for array-oriented numerical computation, with automatic differentiation and just-in-time (JIT) compilation, and optimized for running code on graphic processing units. This state-of-the-art approach allows us to run GEKO on a large number of galaxies, with $\sim 20-60$ min per galaxy depending mainly on the S/N.

3.4.1 Physically motivated priors

A key step when using Bayesian inference is choosing appropriate priors. In order to set informed priors for the morphological modelling, we run PYSERSIC on the $F150W$ (or $F182M$) imaging for all of our objects (Section 3.2), obtaining PSF-deconvolved measurements of the effective radius r_e, the PA $\mathrm{PA}_{\mathrm{morph}}$, the inclination i, the Sérsic index n, and the light centroid (x_0, y_0). In our redshift range $z \sim 3.9-6.5$, $F150W$ and $F182M$ probe the near-UV continuum ($\lambda_{\mathrm{rest}} \sim 2000$ Å), which probes similar star formation time-scales as Hα emission in the early Universe.

Another method for estimating the spatial extent of Hα is to subtract the continuum, estimated from neighbouring filters, from a filter containing both the line and the continuum. However, this method for inferring Hα morphologies directly from the photometry only applies in the redshift ranges where Hα falls in a wide band and outside neighbouring medium bands. Also, it would be less precise at $z > 5$ where Hα falls in the $F444W$ filter, since most of the FRESCO and CONGRESS footprints have no $F460M$ or $F480M$ imaging, with the exception of the JEMS area where the overlap is minimal. For these reasons, we instead use the near-UV morphology, as a loose, consistent prior for all the galaxies in our sample. Using a shorter wavelength filter also has the benefit of a smaller PSF and hence more accurate measurements.

We use Gaussian priors for all of these morphological parameters, doubling the uncertainty obtained from PYSERSIC since we are not measuring the true emission-line morphology. The prior for the total Hα flux is derived from Gaussian fits of the integrated spectrum. For the kinematic parameters, we use uniform priors on σ_0, V_a, and r_t, where this last parameter is bounded by r_e, motivated by lower redshift studies finding $r_t \sim 0.25\, r_{\mathrm{e}}$ (Miller et al. 2011). The prior for the kinematic PA $\mathrm{PA}_{\mathrm{kin}}$is the same as for $\mathrm{PA}_{\mathrm{morph}}$. The free parameters of our model and their priors are summarized in Table 2.

For a given set of parameters, the likelihood is computed by comparing the grism model and observations and assuming a pixel-by-pixel normal distribution. In order to sample our posterior, we use the No U-Turn Sampler (NUTS; Hoffman & Gelman 2011), which is an optimized Hamiltonian Monte Carlo sampler. We fit the grism data, centred on the emission line of interest, to derive the posterior distributions of all of the free parameters of the model: i, $\mathrm{PA}_{\mathrm{kin}}$, r_t,

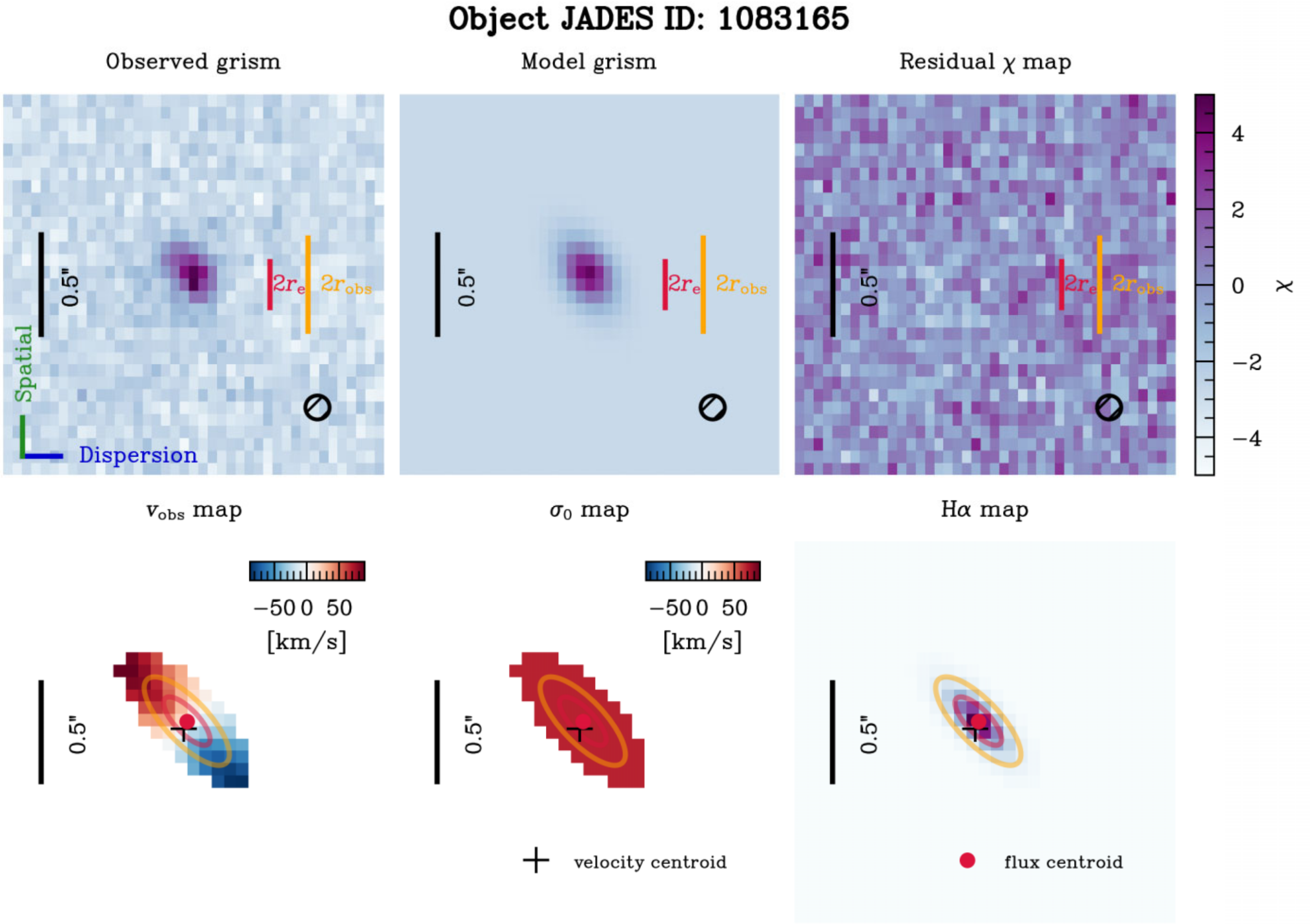

Figure 4. Example science products obtained with GEKO for a galaxy in our gold sample. In the top panels, we show the observed grism data, the best-fitting model, and the corresponding residuals computed with the χ metric. The plotting range is $\chi = [-5, -5]$. We also highlight the best-fitting effective diameter $D_e = 2r_{\rm e}$ for the Hα emission, the (projected) diameter of the S/N > 3 observed map, and the FWHM of the PSF (black circle). In the bottom panel, we show the derived best-fitting velocity field, velocity dispersion field (which has the same velocity scale as the velocity field plot), and the intrinsic Hα emission map. In all of the panels on the left side, we show the scale in arcseconds (black) along with the velocity centroid (black cross). In each row, we show the physical meaning of the axes (spatial versus dispersion).

V_a, σ_0, v_0, PA$_{\rm morph}$, $r_{\rm e}$, I_e, n, x_0, and y_0. We note that the neighbouring [N II] line is undetected or extremely faint for all of the objects in our sample, so we do not account for it in our fitting procedure.

Figs 4 and 5 show an example of the outputs of GEKO. On the top panel of Fig. 4, we show the observed continuum subtracted grism data centred on Hα, followed by our best-fitting model and the residual χ map which is defined by

$$\chi = \frac{\text{model} - \text{obs}}{\text{obs uncertainty}}, \tag{5}$$

and where the bounds for plotting are $\chi = [-5, 5]$. We also highlight the best-fitting effective radius $r_{\rm e}$ of Hα, which is well probed by the grism data. On the bottom row we show the inferred velocity, velocity dispersion, and intrinsic flux maps for Hα. The centre of the velocity curve is marked by a black cross on all three plots. In Fig. 5 we show the posterior distributions of all of the free parameters of the model. We also highlight the best-fitting values and uncertainties, computed from the 16th and 84th quantiles, for the three key kinematic parameters studied in this work: the intrinsic velocity dispersion σ_0, the rotational support v/σ_0, and the dynamical mass $M_{\rm dyn}$. These last two are not free parameters of the model, and are instead derived from them.

3.4.2 Model-derived parameters

We will now briefly outline our definitions for the model-derived parameters. In kinematic studies, a variety of different prescriptions are used to define rotation and dispersion, depending on how many spatial dimensions are probed by the data and on the focus of the work. In this work, and similar to Price et al. (2016, 2020), we define the intrinsic velocity dispersion σ_0 as constant throughout the galaxy and measure it as a broadening that is equally applied across the system. In IFU studies, the velocity dispersion can be measured at (or averaged over) different radii, which can introduce differences in the derived relations (e.g. see discussion in Stott et al. 2016).

For the rotational velocity $v_{\rm rot}$, and the derived rotational support v/σ_0, the prescriptions are even more varied. Some works measure $v_{\rm rot}$ at a certain radius, such as the effective radius $r_{\rm e}$ (e.g. de Graaff et al. 2024a), $r = 2.2r_{\rm s}$[4] (e.g. Price et al. 2016, 2020), or $r = 2.2r_{\rm e}$ (e.g. Stott et al. 2016). Others instead use the maximal observed velocity gradient across the kinematic axis (e.g. Wisnioski et al.

---

[4] $r_{\rm s}$ is the disc scale length $r_{\rm s} \approx 0.6r_{\rm e}$ (Burkert et al. 2010; Miller et al. 2011).

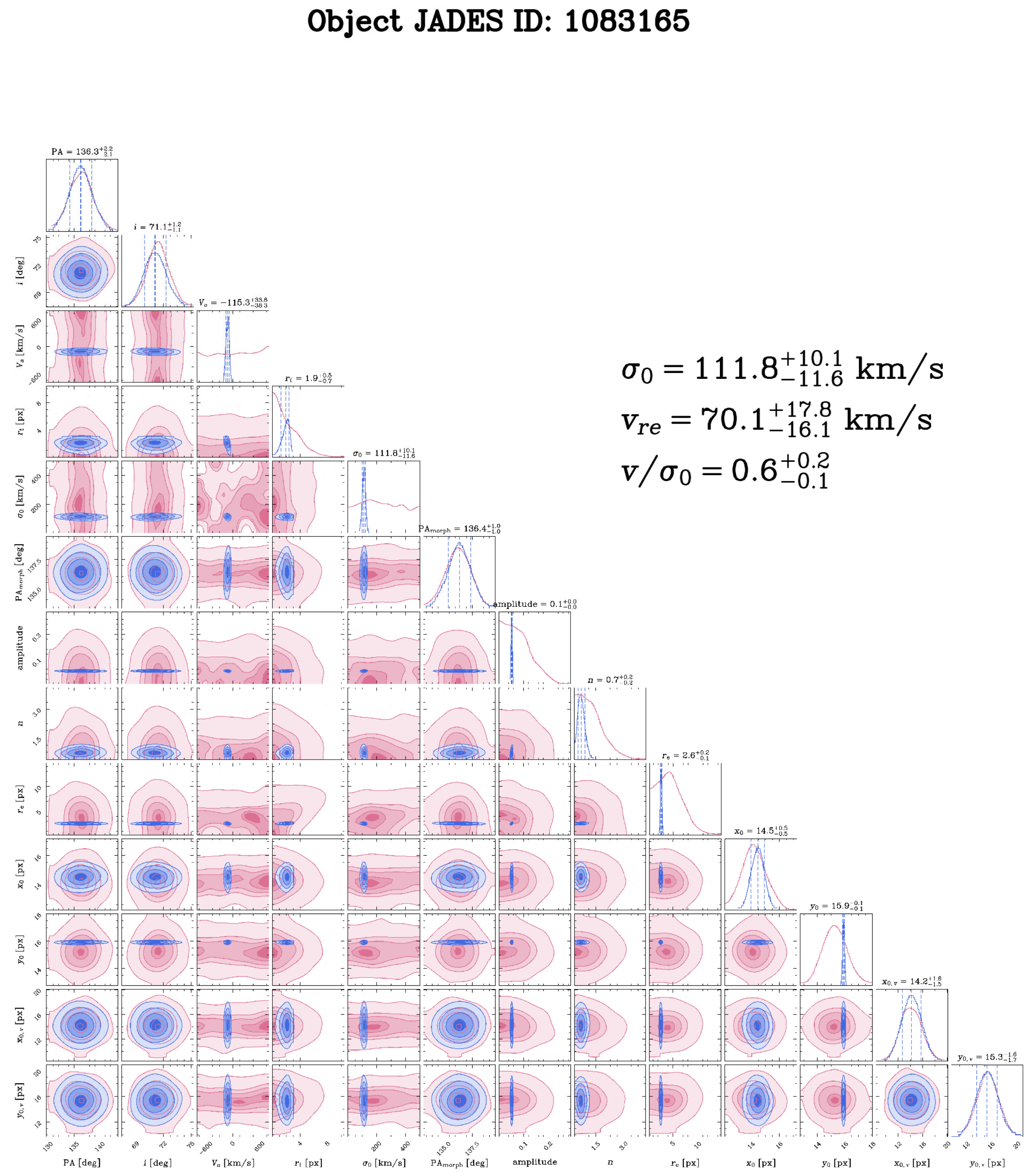

Figure 5. Prior (pink) and posterior (blue) distributions inferred with GEKO for the same gold sample galaxy as in Fig. 4, for the free parameters of our model (Table 2). From these, we derive the posterior distributions for the rotational velocity at $v_{\rm re}$ and the rotational support v/σ_0, whose best-fitting values and uncertainties, computed from the 16th and 84th quantiles, are shown on the top right corner.

2015), or the maximum observed rotational velocity (e.g. Rowland et al. 2024). Due to the grism sensitivity constraints, we do not probe Hα emission to large enough radii and hence measurements at $r = 2.2r_{\rm s}$ or $r = 2.2r_{\rm e}$ would be extrapolations. In this work, we choose to measure the rotational velocity at the effective radius $r_{\rm e}$ because that is where we have constraints from our data. We also explore using the maximal observed rotational velocity $v_{\rm rot} = v_{\rm obs,max}$, but we do not find significant changes in our conclusions (see Appendix C for

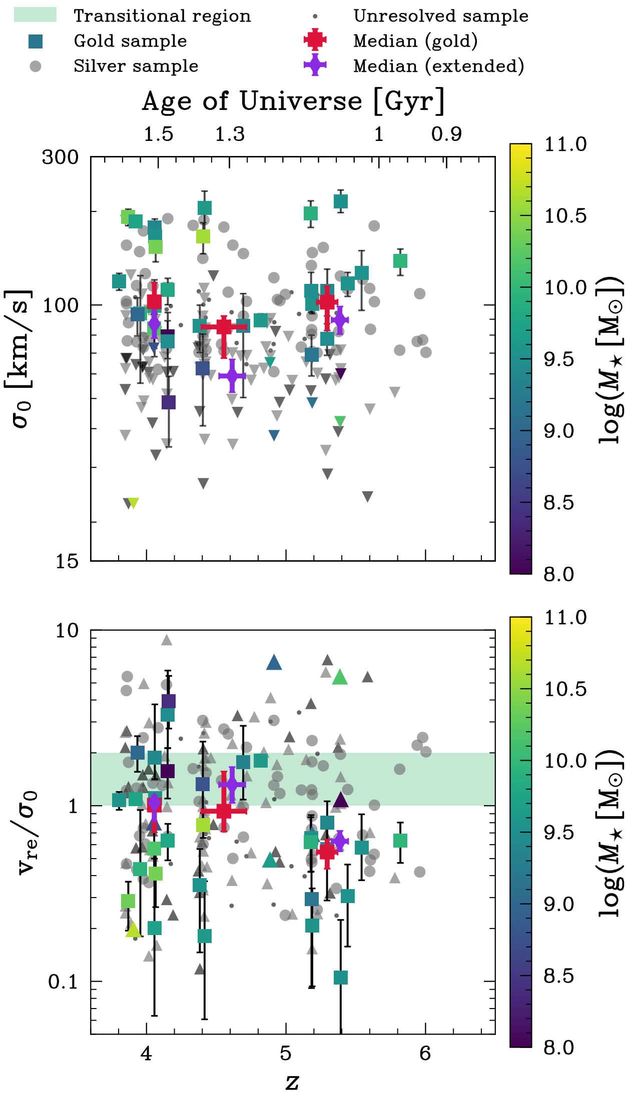

Figure 6. Redshift evolution of the intrinsic velocity dispersion σ_0 (top) and the rotational support v/σ_0 (bottom) for the Hα emitters in the gold sample (squares), silver (big circles), and unresolved (small dots) samples. The medians for the gold (red squares) and extended sample (purple diamonds) show a mild redshift evolution, for both σ_0 and v/σ_0, between $z \sim 4$ and $z \sim 6$. Most of our sample lies in the dispersion supported regime ($v/\sigma_0 < 1$) and the transitional regions ($v/\sigma_0 = 1 - 2$; green shaded region), in part due to the high dispersions measured $\sigma_0 \approx 100$ km s^{-1}.

full discussion), although the quantitative trends slightly change (by $\lesssim 10$ per cent).

In order to infer constraints on dynamical masses, we first need to compute circular velocities $v_{\rm circ}$. The circular velocity is computed assuming an asymmetric drift correction to account for the pressure support (Newman et al. 2013; Wuyts et al. 2016b), which is even more prominent in the turbulent high-redshift galaxies in our sample. We hence defined this term as in Price et al. (2020)

$$v_{\rm circ}(r) = \sqrt{v_{\rm rot}^2(r) + 2(r/r_{\rm s})\sigma_0^2}. \tag{6}$$

At the effective radius r_e, where we compute the circular velocity $v_{\rm circ}(r_{\rm e})$, we have $2(r_{\rm e}/r_{\rm s}) = 3.36$ under the assumption of an exponential disc. We compute the total dynamical mass following

$$M_{\rm dyn} = k_{\rm tot}\frac{r_{\rm e} v_{{\rm circ}(r_{\rm e})}^2}{G}, \tag{7}$$

where G is the gravitational constant and $k_{\rm tot}$ is the virial coefficient (Price et al. 2020). Because we have modelled our galaxies with $q_0 = 0.2$, we choose $k_{\rm tot} = 1.8$ as it is the coefficient for galaxies with $q_0 = 0.2$ and $n \sim 1 - 4$ (Price et al. 2022). The virial coefficient $k_{\rm tot}$ allows us to infer the total dynamical masses based on measurements out to $r_{\rm e}$.

4 THE INTERPLAY BETWEEN KINEMATICS AND STELLAR POPULATIONS FROM $z = 0 - 6.5$

Studies out to $z < 4$ describe the star-forming galaxy population as apparently evolving from turbulent thick discs at cosmic noon to thin discs with ordered rotation in the local Universe. In this section we extend relations between kinematics, redshift, and star formation out to $z \gtrsim 4$ in order to understand how galaxies are growing in the early Universe. We present results from modelling with GEKO and PROSPECTOR on our final sample of ~ 250 Hα emitters. We begin by discussing the redshift evolution of the velocity dispersion σ_0 and rotational support v/σ_0 in our sample, and compare our findings to cosmological simulations and low-redshift measurements (Section 4.1). Then, in Section 4.2, we analyse the relation between these two key kinematic parameters and stellar population parameters, such as stellar mass and SFRs. The median values of σ_0 and v/σ_0 presented in this section are summarized in Appendix A (Tables A2 and A1), along with the kinematic and star-forming properties of every object in the gold sample (Table A3). The fits for the gold sample are shown in Appendix G (Fig. G1). The uncertainties on all of the medians presented in this work are computing using bootstrapping.

4.1 Redshift evolution of ionized gas kinematics from $z = 0$ to $z \sim 6.5$

4.1.1 Kinematics at $z \sim 3.9 - 6.5$

Fig. 6 shows the evolution of the intrinsic Hα velocity dispersion σ_0 and the rotational support v/σ_0 as a function of redshift for the galaxies in this work. Colour-coded by stellar mass, we plot objects in our gold, silver, and unresolved samples, including upper[5] and lower limit[6] detections for which the value at 1σ is plotted instead. We compute (and report in Appendix A) the medians values of v/σ_0 and σ_0, for three redshift bins probing ≈ 250 Myr, for the gold sample only (Table A2) and for the extended galaxies in the gold and silver samples (Table A1). We define galaxies as extended when the grism data extends beyond the best-fitting Hα effective radius

---

[5] For v/σ_0, we mark a measurement as a upper limit when the 16th quantile of the posterior distribution of $v_{\rm re}$ includes zero. All of the unresolved objects fall into this category. For σ_0 measurements, upper limits are defined in a similar way but we loosen the requirement to the 16th quantile being smaller than 30 km s^{-1}, due to resolution limits.

[6] If the σ_0 measurement is an upper limit for a given v/σ_0 point, then this point is marked as a lower limit, since the ratio diverges when $\sigma_0 \to 0$. If a given v/σ_0 verifies both upper and lower limits criteria, meaning its posterior distribution both coincides with zero and has a long tail, then we mark it as a lower limit since the velocity constraint is more secure than the velocity dispersion, which is rarely zero and likely only hits the limit due to resolution effects.

(see Section 2.3 and Table 1). In both cases we report measured for $v_{\rm rot} = v_{\rm re}$ as well as $v_{\rm rot} = v_{\rm obs,max}$ in (Tables A1 and A2). The medians are computed from the combined posterior distributions of all of the galaxies in a given bin, and their uncertainties are measured using bootstrapping.

We do not find an evolution in the median values for the velocity dispersion σ_0 from $z \sim 4$ to $z \sim 6$ for both the gold sample and the extended sample, with $\sigma_0 = 102^{+15}_{-15}$ km s^{-1} to $\sigma_0 = 102^{+19}_{-13}$ km s^{-1}, and with $\sigma_0 = 87^{+10}_{-8}$ km s^{-1} to $\sigma_0 = 89^{+9}_{-9}$ km s^{-1}, respectively. We do not find significant differences between the medians for these two subsamples. This is consistent given that they probe similar stellar mass distributions (Fig. A2). Where the high- and low-redshift bins probe similar stellar masses, the median mass in the central bin $(4.2 < z < 5.0)$ is $\sim 0.3 - 0.4$ dex lower (Tables A1 and A2), which could explain the lower median value of σ_0 found (see Section 4.2). The medians for the resolved sample are lower in all bins, which is most likely driven by their lower median masses (Tables A1 and A2). We investigate the overall mass dependence of the $\sigma_0 - z$ evolution but find no distinct trend in our data, although an overall mass trend is investigated in a broader redshift range in Sections 4.1.2 and 4.1.3.

We find an overall mild decrease of the rotational support with redshift between $z \sim 4$ and $z \sim 6$ for both the gold sample and the extended sample, with $v/\sigma_0 = 1.0^{+0.1}_{-0.3}$ to $v/\sigma_0 = 0.5^{+0.1}_{-0.1}$ and $v/\sigma_0 = 1.0^{+0.1}_{-0.2}$ to $v/\sigma_0 = 0.6^{+0.1}_{-0.1}$, respectively. Similarly to the trends for σ_0, we do not find significant differences in the median values for these two subsets. These low values of v/σ_0 highlight the turbulent nature of the galaxy population at high redshift, with medians falling in the dispersion-dominated regime by $z \sim 6$. At the redshifts studied in this work, the medians fall in and below the transition region where galaxies have some rotational support but are unstable.

The large observed scatter, spanning ≈ 0.6 dex in σ_0 and ≈ 2 dex in v/σ_0, can in part be attributed to measurement uncertainties, which can reach ≈ 0.3 dex in σ_0 and ≈ 0.5 dex in v/σ_0. However, it also highlights an intrinsic scatter in the galaxy population probed in this work, with resolved velocity dispersions spanning $\sigma_0 \sim 50 - 200$ km s^{-1}. This can also be seen in the measurements of v/σ_0, with many galaxies being consistent with a dispersion-dominated state, but others reaching values $v/\sigma_0 \sim 2 - 4$, which are consistent with turbulent discs.

Although many simulations predict that gas discs at high redshift are not highly rotationally dominated (El-Badry et al. 2018; Pillepich et al. 2019), consistent with what we see in this work, some works also highlight the key role of undisturbed co-planar and co-rotating gas accretion in building and sustaining rotation-dominated discs (Dekel et al. 2009; Sales et al. 2012; Kretschmer, Agertz & Teyssier 2020; Kretschmer, Dekel & Teyssier 2022; Kohandel et al. 2024). These discs survive until they are destroyed by external effects such counter-rotating streams and mergers, which happen of the order of a few orbital times (Dekel & Burkert 2014; Zolotov et al. 2015; Tacchella et al. 2016b, a; Dekel et al. 2020; Kretschmer et al. 2022). The effect of these processes on the measured rotational support of the gas could explain the range of v/σ_0 values we measure on Fig. 6, where we probe galaxies in different stages of these fluctuations between disc build-up and dismantling.

4.1.2 *The evolution of the ionized gas velocity dispersion*

We now place our measurements in the context of the other studies targeting cold and warm ionized gas across cosmic time (see Appendix F for details of each survey). For the rest of this paper, we use the term cold gas for tracers such as CO and [C II], in contrast with tracers of warmer (ionized) gas such as Hα and [O III]. We show the evolution of the velocity dispersion σ_0, shown in Fig. 7. The high values $\sigma_0 \gtrsim 70 - 100$ km s^{-1} we find lie above measurements from cosmic noon (Wisnioski et al. 2015; Simons et al. 2016; Tiley et al. 2016; Genzel et al. 2017; Turner et al. 2017a; Übler et al. 2019; Price et al. 2020). It is important to note that many of these works restrict their analyses to rotationally supported systems with $v/\sigma_0 > 1$, which could reduce the number of systems with high σ_0 in their samples.

In order to quantify the evolution of σ_0 from $z \sim 0$ to $z \sim 6$, we fit our sample in conjunction with the KMOS3D sample at $z \sim 1 - 3$ (Übler et al. 2019) and the SAMI galaxy survey at $z \sim 0$ (Varidel et al. 2020). We fit a power law form allowing for both a stellar mass and redshift dependence,

$$x_0 = x_{0,z=3}\left(\frac{1+z}{4}\right)^{\alpha}\left(\frac{M_\star}{10^9\ \mathrm{M}_\odot}\right)^{\beta}, \qquad (8)$$

where x is replaced by σ_0 or v/σ_0. We plot our best-fitting relations on the left panel in Fig. 7, including and excluding the upper limits, as well as including and excluding the $z \sim 0$ measurements. The latter is done to specifically study the evolution from cosmic noon to $z > 4$ and understand the impact of including measurements from the local Universe. The relations are all plotted for a fixed mass $M_\star = 10^{9.5} M_\odot$. We summarize the best-fitting model parameters for each scenario in Table 3, and find consistent values across the three fits. Our results show a close to linear dependence of σ_0 on $(1+z)$, with $\alpha = 0.86 \pm 0.02$ when the full three samples are fit. The relation becomes linear, $\alpha = 1.03 \pm 0.07$, when only the cosmic noon and high-redshift samples are fit, pointing to a stronger evolution in σ_0. On the other hand, the mass dependence is weak, $\beta = 0.02 \pm 0.01$, and only increases slightly to $\beta = 0.06 \pm 0.02$ when excluding the SAMI sample at $z \sim 0$. This implies that at fixed redshift, we do not find evidence for a strong dependence on the stellar mass. We find consistent results when excluding upper limits from the fit, but the overall normalization $\sigma_{0,z=3}$ and redshift dependence α are increased by ~ 10 per cent.

We compare our fit to the linear relation $\sigma_0 = az + b$ from Übler et al. (2019), which is given by $a = 9.8 \pm 3.5$ km s^{-1}, $b = 23.3 \pm 4.9$ km s^{-1}, and is computed using median measurements from surveys at $z = 0 - 3.5$. We find good agreement with the extrapolation of this relation to the $z \sim 4 - 6$, which highlights the increase of turbulence with redshift. As highlighted on Fig. 7, our best-fitting relation predicts a steeper evolution of σ_0 between $z \sim 2$ and $z > 4$. It is however important to note that the fit from Übler et al. (2019) does not account for a mass dependence, whereas our fit is plotted for an arbitrary stellar mass $M_\star = 10^{9.5} M_\odot$, making a one-to-one comparison difficult. When our best-fitting $\sigma_0 - z$ relation is placed in the context of other measurements across redshifts (right panel of Fig. 7), it offers a good representation of the overall evolution despite the large variation between measurements from different samples. Our velocity dispersions are in the same ranges as probed by the ionized gas measurements from Parlanti et al. (2023), although they probe higher stellar masses in general, most of which also lie above our relation. de Graaff et al. (2024a) find low values of σ_0 that lie below the expected evolution of $\sigma_0 - z$, which could be in part driven by the low stellar masses probed $\log M_\star[\mathrm{M}_\odot] \approx 8$. We do not find evidence for a strong mass dependence at fixed redshift, but we are also not sensitive to the low masses probed by de Graaff et al. (2024a).

When looking at cold gas tracers (i.e. CO, [C I], [C II]), the dynamically cold systems reported at high redshift (Swinbank et al.

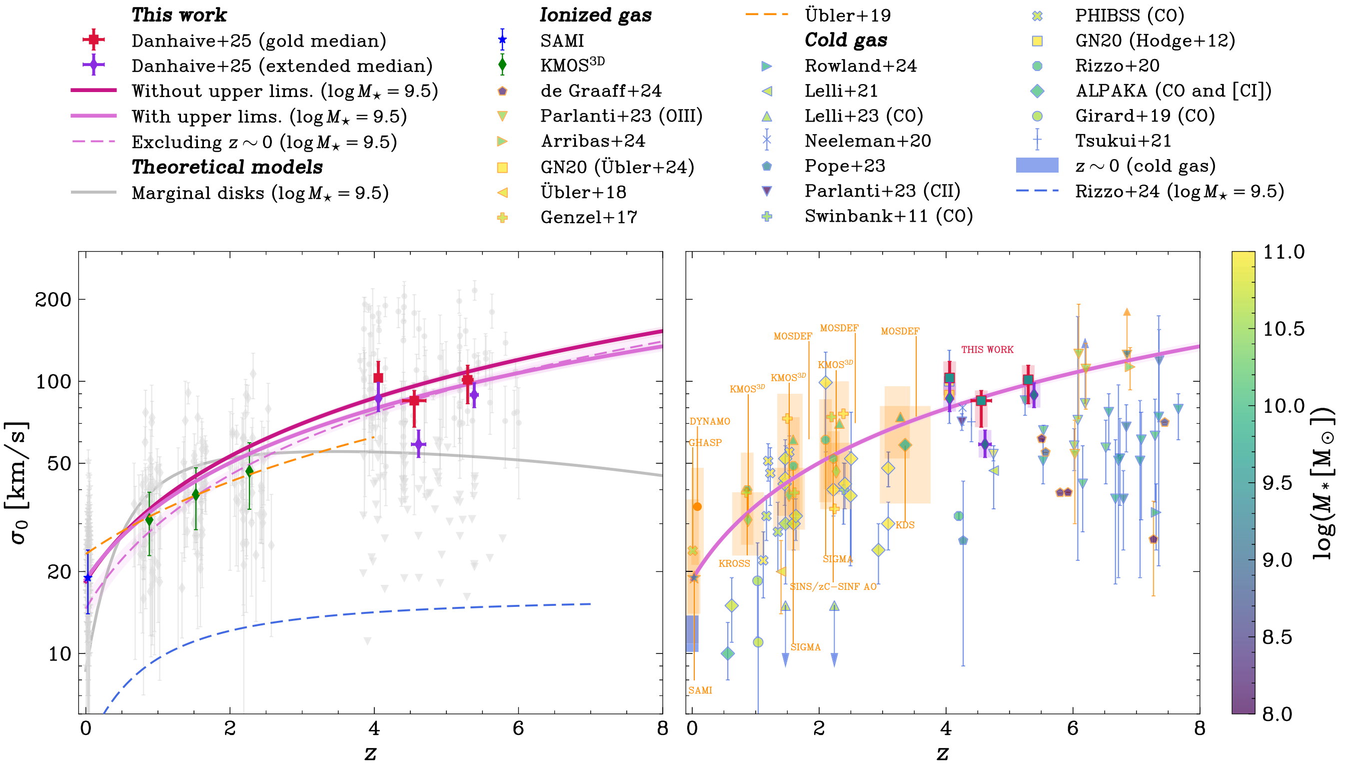

Figure 7. Evolution of the intrinsic Hα velocity dispersion σ_0 as a function of redshift. (left) We study the evolution of σ_0 through three samples: the SAMI sample at $z\sim0$ (blue star, Varidel et al. 2020), the KMOS3D sample at $z\sim1-3$ (green diamonds, Übler et al. 2019), and our gold (red squares) and silver samples at $z\sim4-6$. The best-fitting relations (equation 8), plotted at $\log M_\star[\mathrm{M}_\odot]=9.5$, are shown for fits including σ_0 upper limits from our sample (light purple curve), excluding them (dark purple curve), and excluding the $z\sim0$ sample (dashed light purple curve). We compare our predicted evolution with the fit from Übler et al. (2019) (light red – long dashes), which is defined out to $z\sim4$. Similarly, we also include the fit for cold gas measurements at fixed mass from Rizzo et al. (2024) (dark blue – long dashes) defined out to $z\sim7$, which highlight a similar evolution of σ_0 tracing the cold gas, albeit with a factor 2–3 lower normalization. In grey, we show the prediction from the marginal disc model at $\log M_\star[\mathrm{M}_\odot]=9.5$. (right) We place our median points and fits in the context of studies of warm ionized gas (i.e. Hα and [O III]; orange outlines) and cold gas (i.e. H I, CO, and [C II]; blue outlines) kinematics across redshifts. The medians for the gold and extended samples are plotted in red squares and purple diamonds, respectively. Our results are consistent with a decrease of σ_0 with cosmic time when compared to surveys from cosmic noon (KMOS3D, Wisnioski et al. 2015; KROSS; Johnson et al. 2018; MOSDEF, Price et al. 2016, 2020; KDS, Turner et al. 2017b, a; SIGMA, Simons et al. 2016; SINS/zC-SINF, Förster Schreiber et al. 2006, 2018; PHIBSS, Tacconi et al. 2013; ALPAKA, Rizzo et al. 2023, and points from Swinbank et al. 2011, Genzel et al. 2017, Girard et al. 2019, and Lelli et al. 2023) and the local Universe (SAMI, Epinat et al. 2010; GHASP, Varidel et al. 2020; DYNAMO, Green et al. 2014; EDGE-CALIFA, Bolatto et al. 2017; HERACLES, Leroy et al. 2009; THINGS, Walter et al. 2008, and Dib et al. 2006; blue shaded region). We compare our measurements with works at similar redshifts (Parlanti et al. 2023; Arribas et al. 2024; de Graaff et al. 2024a; Übler et al. 2024), as well as detection of dynamically cold systems at high-redshift (Hodge et al. 2012; Neeleman et al. 2020; Rizzo et al. 2020; Lelli et al. 2021; Tsukui & Iguchi 2021; Pope et al. 2023; Rowland et al. 2024).

Table 3. Best-fitting parameters and uncertainties for $\sigma_0 = \sigma_{0,z=3}\left(\frac{1+z}{4}\right)^{\alpha}\left(\frac{M_\star}{10^9\ \mathrm{M}_\odot}\right)^{\beta}$ (equation 8) based on the SAMI sample at $z\sim0$, the KMOS3D sample at $z\sim1-3$, and our gold and silver samples at $z\sim4-6$.

	w/ upper lims.	w/o upper lims.	w/o $z\sim0$
$\sigma_{0,z=3}$ (km s^{-1})	64 ± 1	70 ± 1	65 ± 2
α	0.86 ± 0.02	0.93 ± 0.02	1.03 ± 0.07
β	0.02 ± 0.02	0.01 ± 0.01	0.06 ± 0.02

2011; Neeleman et al. 2020; Rizzo et al. 2020; Lelli et al. 2021; Pope et al. 2023; Rowland et al. 2024) are in good agreement with the prediction from Rizzo et al. (2024), with low dispersions of $\sigma_0\approx20-50$ km s^{-1}, which are characteristic of cold gas tracers.

In the framework of marginally stable discs, the expected evolution of v/σ_0 and σ_0 with redshift can be computed directly from the gas fraction using the Toomre parameter Q (Toomre 1964), which represents the instability of the disc through the turbulence in the ISM. In this empirical model, gas is accreted from the surrounding halo or cosmic web and is expelled through feedback (Förster Schreiber et al. 2006; Genzel et al. 2008; Dekel et al. 2009; Lilly et al. 2013). The Toomre parameter Q measures the equilibrium between the self-gravity of the gas and repelling forces due to turbulence and rotational support. Marginally stable discs are defined by $Q_{\mathrm{crit}}\sim1$, where $Q_{\mathrm{crit}}<1$ indicates an unstable disc. In this model, the redshift evolution of v/σ_0 and σ_0 can be explained by the increase of gas fractions within these marginally stable discs (Genzel et al. 2011; Wisnioski et al. 2015):

$$v/\sigma_0 = \frac{a}{f_{\mathrm{gas}}(z)Q_{\mathrm{crit}}}, \tag{9}$$

where $a=\sqrt{2}$ for a disc with a constant rotational velocity. In order to qualitatively compare this model to our measurements, we plot, on the left panel of Fig. 7, σ_0 as predicted by equation (9) for $Q=1$,

$v = 100\ \mathrm{km\,s^{-1}}$, and the same stellar mass ($M_\star = 10^{9.5} M_\odot$) chosen for our best-fitting relation. We derive the total gas fractions $f_\mathrm{gas} = M_\mathrm{gas}/(M_\mathrm{gas} + M_\star)$ from the empirical relation derived in Tacconi et al. (2018) and Tacconi et al. (2020), where $f_\mathrm{gas}(z)$ depends on total stellar mass, sSFR, and the distance from the SFMS. We plot this relation for galaxies on the main sequence.

Interestingly, the observed increase of σ_0 with z is not well reproduced by the marginal disc model, which shows an increase of σ_0 until cosmic noon ($z \approx 2-3$) but then decreases slowly towards higher redshifts. This could point to sources of turbulence beyond the gravitational instabilities described in the marginal disc model, such as feedback and mergers (see Sections 5.1 and 5.2) More importantly, this model relies on assumptions of equilibrium and isotropy which may not be applicable to the clumpy gas-rich discs studied at $z > 1$ (Romeo, Burkert & Agertz 2010; Romeo & Agertz 2014). Furthermore, it assumes an infinitesimally thin gas disc and is not able to account for the stabilizing effect of the gas vertical stratification (see Bacchini et al. 2024; Rizzo et al. 2024, for in-depth discussions).

4.1.3 The evolution of the rotational support across cosmic time

As highlighted on the right panel of Fig. 8, works from the local Universe (Epinat et al. 2010) to cosmic noon (Wisnioski et al. 2015; Simons et al. 2016; Price et al. 2020; Genzel et al. 2020) show that v/σ_0 declines from an average of $\mathrm{v}/\sigma_0 \sim 10$ at $z \sim 0-1$ to $\mathrm{v}/\sigma_0 \sim 2-4$ by $z \sim 2.5-3.5$ for galaxies with stellar masses $\approx 10^9 - 10^{11}\ \mathrm{M_\odot}$. In the local universe, star-forming galaxies have stellar masses up to $\approx 10^{11}\ \mathrm{M_\odot}$, whereas studies at cosmic noon probe lower masses on average, partly driving the observed trend. These studies imply that star-forming discs are turbulent at cosmic noon and only settle into dynamically cold discs at later times. We find a further decrease to medians of $\mathrm{v}/\sigma_0 \approx 1$ by $z \sim 3.9-6.5$, consistent with predictions of a smooth decline of v/σ_0 from the Illustris-TNG50 simulations, for the kinematics probed by Hα (Pillepich et al. 2019).

On the left panel of Fig. 8, we study this evolution in more detail by fitting the same samples as for σ_0 for both their mass and redshift dependence (equation 8), and plot the best-fitting relations at a fixed mass of $M_\star = 10^{9.5} M_\odot$. Because the mass range of the KMOS3D data is $\log M_\star[\mathrm{M_\odot}] \sim 10-11$, whereas the SAMI data spans a similar mass range to our sample ($\log M_\star[\mathrm{M_\odot}] \sim 8-10$), the best-fitting curves at $M_\star = 10^{9.5} M_\odot$ cut below the bulk of the KMOS3D data. The values of the fit parameters are summarized on Table 4. The slope of the redshift dependence is close to linear when upper limits are both included and excluded, $\alpha = -1.06 \pm 0.05$ and $\alpha = -0.88 \pm 0.05$, respectively, but becomes much steeper when the $z \sim 0$ sample is excluded from the fit, with $\alpha = -1.68 \pm 0.10$. Similarly to σ_0, this behaviour suggests that the redshift evolution is steeper from $z \sim 1-3$ to $z > 4$ than from $z \sim 0$ to $z \sim 1-3$. Even though we find evidence for a stellar mass dependence, Fig. 8 shows that the decrease of v/σ_0 with redshift is apparent even at fixed mass.

Our sample probes a lower mass range than many of the studies in the local Universe and at cosmic noon shown on the right panel of Fig. 8, with the majority of galaxies in the $\log M_\star[\mathrm{M_\odot}] \sim 8-10$ range. The sample from de Graaff et al. (2024a) probes even lower masses $\log M_\star[\mathrm{M_\odot}] \sim 7-9$ but still shows a range of kinematic states. We further compare our results to the sample of ionized ([O III]) and cold ([C II]) gas observations from Parlanti et al. (2023), which reaches out to $z \sim 8$. Many studies have shown that cold gas is typically less turbulent than ionized gas, resulting in overall lower velocity in both observations (e.g. Übler et al. 2019; Varidel et al. 2020; Rizzo et al. 2024) and simulations (e.g. Kohandel et al. 2024). Given these intrinsically lower velocity dispersions, as well as their higher masses (which typically imply higher rotational velocities), the measurements from Parlanti et al. (2023) are consistent with our observations of star-forming galaxies being turbulent at high redshift.

Various high-redshift dynamically cold discs have been reported with ALMA and *JWST* observations (Neeleman et al. 2020; Rizzo et al. 2020; Lelli et al. 2021; Pope et al. 2023; Rowland et al. 2024; Übler et al. 2024), and are plotted on Fig. 8. The first thing to note is their stellar masses. In fact, all of the galaxies reported in these works, with the exception of Pope et al. (2023), have stellar masses $M_\star > 10^{10}\ \mathrm{M_\odot}$ comparable to the star-forming discs observed at $z < 3$. Their high masses indicate that these systems are more evolved than their lower-mass counterparts and are not always representative of the bulk of the galaxy population at $z \sim 3.9-6.5$. For instance, the systems from Lelli et al. (2021), Rowland et al. (2024), and Übler et al. (2024) all lie close to or above the characteristic mass above which the stellar mass function at those redshifts drops exponentially (Weibel et al. 2024; Shuntov et al. 2025; Harvey et al. 2025), indicative of their extreme nature. Furthermore, all of these measurements (with the exception of Arribas et al. 2024; Übler et al. 2024) are based on cold gas tracers (CO and [C II]), which as mentioned previously typically have intrinsically lower velocity dispersions and hence higher rotational support. Finally, where we measure the rotational velocity at r_e, many of these works use different quantities such as the maximum observed velocity, which is typically higher (e.g. Rowland et al. 2024).

In our sample, we find one system with comparable rotational support $\mathrm{v}/\sigma_0 \sim 10$ to these works, which is the massive galaxy previously reported in Nelson et al. (2024) as a rapidly rotating system at $z = 5.2$ with $v_\mathrm{rot}(r_\mathrm{e}) = 240^{+50}_{-50}\ \mathrm{km\,s^{-1}}$. It is also discussed in Li et al. (2023) where they find a similar value of $v_\mathrm{rot}(r_\mathrm{e}) = 211^{+21}_{-18}\ \mathrm{km\,s^{-1}}$. Our best-fitting value of $v_\mathrm{rot}(r_\mathrm{e}) = 231^{+21}_{-15}\ \mathrm{km\,s^{-1}}$ is in good agreement with these works. However, both Nelson et al. (2024) and Li et al. (2023) find relatively low values for the rotational support, $\mathrm{v}/\sigma_0 \sim 2$, in contrast with our finding of $\mathrm{v}/\sigma_0 \sim 10$. This is most likely due to differences in the morphological and kinematic modelling. For example, Nelson et al. (2024) do not forward model the impact of the LSF but subtract it in quadrature, and Li et al. (2023) match the image PSF to the LSF instead of modelling their effects separately.

To compare our findings to the Toomre marginal disc model, we plot equation (9) on Fig. 8 for $Q = 1$, and $M_\star = 10^{9.5} M_\odot$. After a sharp decline from $z = 0$ to $z \sim 2$, this model predicts nearly constant values of v/σ_0 beyond $z > 2$ at fixed stellar mass. This is driven by the strong dependence of gas fractions on stellar mass. In fact, most galaxies assemble the bulk of their stellar mass at cosmic noon where the cosmic SFR density peaks. At later cosmic times, galaxies are overall more massive and hence have lower gas fractions, which drives an increase in v/σ_0 as they settle into cold discs (equation 9). At $z > 2$, the stellar masses probed are low on average $\log M_\star[\mathrm{M_\odot}] < 10$, which is reflected in the high gas fractions and low values of v/σ_0, and, importantly, they evolve slower. However, observations and simulations show that gas fractions increase with redshift at fixed mass (Tacchella et al. 2020; de Graaff, Pillepich & Rix 2024b).

Our measured values of v/σ_0 are broadly consistent with predictions from this simple model, as is the evolution of v/σ_0 at lower redshift. This suggests that gravitational instabilities due to the high gas fraction observed in high-redshift galaxies (Tacconi et al. 2018; Parlanti et al. 2023) can drive the decrease in rotational support. Unstable discs are also qualified by fragmentation and clumpy

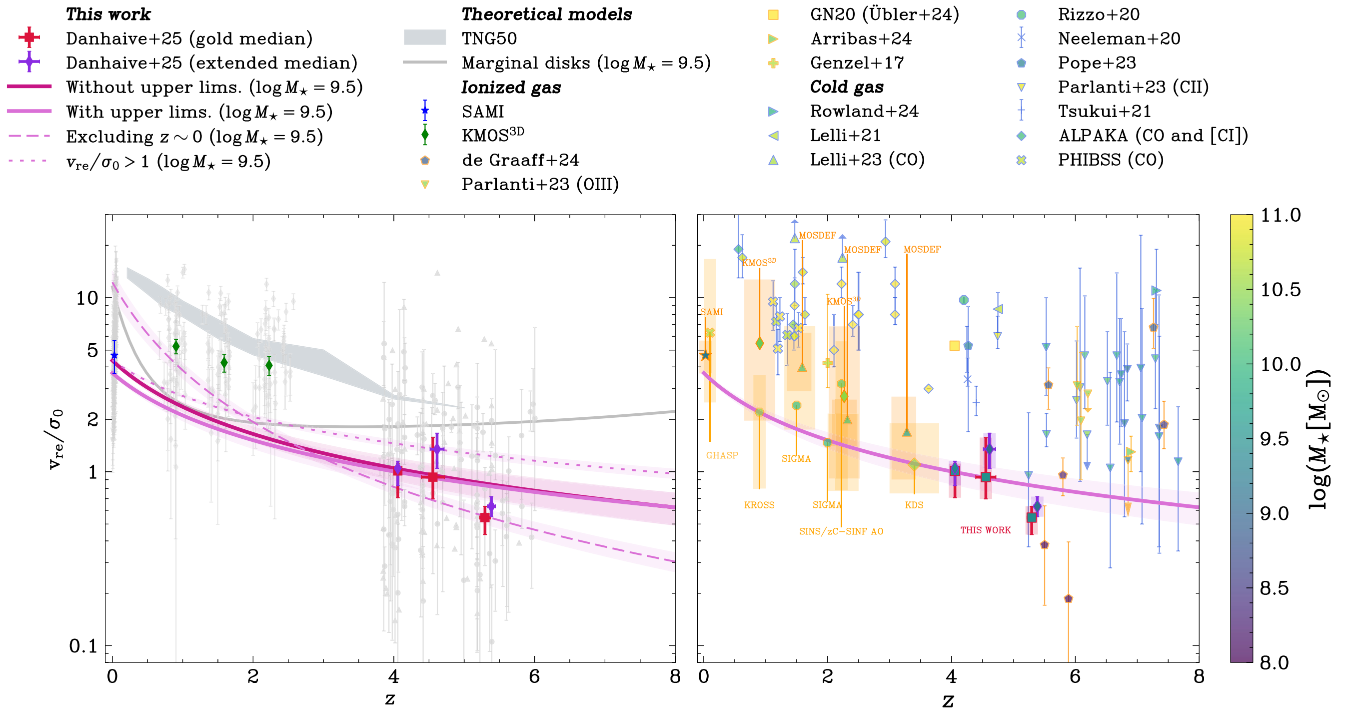

Figure 8. Evolution of the rotational support v/σ_0 with redshift. (left) We study the evolution of v/σ_0 through three samples: the SAMI sample at $z \sim 0$ (blue star; Varidel et al. 2020), the KMOS3D sample at $z \sim 1-3$ (green diamonds, Übler et al. 2019), and our gold (red squares) and silver samples at $z \sim 4-6$. The full samples are plotted behind each median in grey. The best-fitting relations (equation 8), plotted at $\log M_\star[M_\odot] = 9$, are shown for fits including σ_0 upper limits from our sample (light purple curve), excluding them (dark purple curve), and excluding the $z \sim 0$ sample (dashed light purple curve). We also include a fit where we only fit rotationally supported systems ($v/\sigma_0 > 1$, dotted light purple curve). Our measurements are consistent with a decrease of v/σ_0 with redshift as predicted by the TNG50 cosmological simulations (Pillepich et al. 2019), shown with the shaded grey region. Within the context of lower z measurements, our results are consistent with a decline of rotational support with redshift even at fixed mass, in contrast with predictions from the Toomre (in)-stability model described in Wisnioski et al. (2011), indicated with a solid line. (right) Our sample span similar v/σ_0 values as the ones of de Graaff et al. (2024a), despite probing slightly higher masses, and are overall consistent with cold gas ([C II]) measurements (blue outlines) from Parlanti et al. (2023), who find turbulent discs at $z \sim 6-7$. Our results are also placed in the context of surveys (shaded orange regions) of ionized gas (orange outline) from cosmic noon and the local Universe: MOSDEF (Price et al. 2016), KMOS3D (Wisnioski et al. 2015), SIGMA (Simons et al. 2016), SINS/zC-SINF AO (Förster Schreiber et al. 2018), KROSS (Stott et al. 2016; Tiley et al. 2016), KDS (Turner et al. 2017b, a), and GHASP (Epinat et al. 2010). We also include medians from Genzel et al. (2020), and measurements from Übler et al. (2024). We add single-object detections of dynamically cold systems in the early Universe (Hodge et al. 2012; Rizzo et al. 2020; Neeleman et al. 2020; Lelli et al. 2021; Tsukui & Iguchi 2021; Pope et al. 2023; Rowland et al. 2024), which probe higher masses (i.e. more evolved systems) than our sample, and an unsettled disc in a protocluster (Arribas et al. 2024). Finally, we include measurements of cold gas at cosmic noon from PHIBSS (Tacconi et al. 2013), ALPAKA (Rizzo et al. 2024), and Swinbank et al. (2011), Girard et al. (2019).

Table 4. Best-fitting parameters and uncertainties for $v/\sigma_0 = v/\sigma_{0_{z=3}} \left(\frac{1+z}{4}\right)^\alpha \left(\frac{M_\star}{10^9\,M_\odot}\right)^\beta$ (equation 8) based on the SAMI sample at $z \sim 0$, the KMOS3D sample at $z \sim 1-3$, and our gold and silver samples at $z \sim 4-6$.

	w/ upper lims.	w/o upper lims.	w/o $z \sim 0$
$v/\sigma_{0_{z=3}}$	1.4 ± 0.1	1.7 ± 0.1	1.5 ± 0.1
α	-1.06 ± 0.05	-0.88 ± 0.05	-1.68 ± 0.10
β	0.28 ± 0.01	0.27 ± 0.01	0.19 ± 0.04

star formation, which has been observed in this sample and other high-redshift observations (Nakazato et al. 2024). Our dispersion-supported systems naturally lie below this relation and occupy a more unstable regime, with $Q < 1$. The instability in these systems could be in part explained by stellar feedback and mergers, which are not accounted for in the Toomre model. Due to the large quantity of these systems (see Section 5.1), our best-fitting relations lie well below the marginal disc model at $z > 4$, highlighting the need for more complex models to explain the star-forming galaxy population at high-redshift. This is also shown by our fit to only rotationally supported systems ($v/\sigma_0 > 1$, dotted line on the left panel of Fig. 8), whose flatter slope $\alpha = -0.68 \pm 0.03$ is more comparable to the marginal disc model. The slope of our $v/\sigma_0 - z$ relation is consistent with predictions from the TNG simulations (Pillepich et al. 2019), albeit with a lower normalization, which could in part be driven by the lack of bursty star formation in these simulations, which plays a key role at high redshift.

A key complexity of studying the evolution of v/σ_0 is the large variety of different methods and definitions used by different studies. Although quantifying each of these is beyond the scope of this work, we quantify the impact of selecting only rotationally supported systems, as is often done at lower redshift ($z < 4$). As shown on Fig. 8, making this cut increases the intercept ($v/\sigma_{0_{z=3}} = 2.3 \pm 0.1$) and decreases the redshift dependence ($\alpha = -0.68 \pm 0.01$) by ~ 0.2 dex. However, importantly, the decrease of v/σ_0 at fixed mass persists.

In summary, Fig. 8 shows that galaxies become increasingly turbulent at high redshift, with only the most evolved systems being able to settle into cold discs. Our findings underline high turbulence in high-redshift systems, with $\sigma_0 \approx 100\ \mathrm{km\,s^{-1}}$ and $\mathrm{v}/\sigma_0 \approx 1$ at $z \sim 3.9 - 6.5$. To further explore what could be driving this strong increase, we will study how v/σ_0 and σ_0 are related to their stellar populations.

4.2 The effect of star formation on internal kinematics

At high redshift $z > 3$, the bulk of the galaxy population is in its early growth stages, and is characterized by smaller masses and sizes. These systems are hence less stable to perturbations from mergers, gas accretion, and stellar outflows, than their more evolved, low redshift counterparts. One of the characteristics of the large sample of galaxies studied in this work is the large scatter in their kinematic properties. In order to investigate what is driving the observed scatter, and to further understand the main causes of the high turbulence observed at high redshift, we look at how the velocity dispersion and rotational support correlate with other physical properties of the galaxy, specifically stellar mass $M_\star$, SFR averaged over the past 10 Myr (SFR_{10}), the corresponding specific SFR (sSFR_{10}) and SFR surface density ($\Sigma_{\mathrm{SFR}_{10}}$). $\Sigma_{\mathrm{SFR}_{10}}$ is computed assuming that half of the total SFR is arising from inside the half-light radius r_e:

$$\Sigma_{\mathrm{SFR}_{10}} = \frac{\mathrm{SFR}_{10}/2}{\pi r_\mathrm{e}^2}. \tag{10}$$

We use the best-fitting half-light radius of the Hα emission, as it is the most representative of regions of recent star formation, as probed by SFR_{10}. After presenting the results for our sample (Section 4.2.1), we place them in the context of correlations found in other works (Section 4.2.2) and discuss the implications for the evolution of galaxies and the formation of discs at high redshift.

4.2.1 Trends at $z \gtrsim 4$

Fig. 9 shows the evolution of σ_0 and v/σ_0 with $M_\star$, SFR_{10}, sSFR_{10}, and $\Sigma_{\mathrm{SFR}_{10}}$, with medians plotted for the gold and extended samples, and summarized in Tables A1 and A2, respectively. The silver sample, highlighted in grey contours, lies on the lower portion of the σ_0 distribution when compared to the gold sample. This causes the gold sample medians to lie above the bulk of the silver sample measurements. Galaxies in the silver sample typically have lower SFR_{10} and $\Sigma_{\mathrm{SFR}_{10}}$, but on average probe similar stellar masses and sSFR_{10} to the gold sample. This is likely due to our S/N cut, which is more lenient for the silver sample. The gold sample has the brightest Hα galaxies, which hence have higher SFRs and are typically more massive.

The strongest correlation[7] we observe is between σ_0 and SFR_{10}, with Spearman rank coefficient $\rho = 0.42$ and p-value $p < 0.001$, with averages going from $\sigma_0 \approx 70 - 80$ at $\mathrm{SFR}_{10} = 10\,\mathrm{M}_\odot\,\mathrm{yr}^{-1}$ to $\sigma_0 \approx 100$ at $\mathrm{SFR}_{10} = 20 - 100\,\mathrm{M}_\odot\,\mathrm{yr}^{-1}$. This correlation naturally arises from the main physical drivers of turbulence, namely feedback from star formation and the release of gravitational energy through the radial inflow of gas through the disc (Krumholz & Burkhart 2016; Krumholz et al. 2018), as both are connected to star formation activity. Such processes would manifest as non-circular motions of the gas, which have been shown to correlate with the gas velocity dispersion at $z \sim 0.3$ (Mai et al. 2024).

Our results at $z \gtrsim 4$ are broadly in agreement with predictions from gravitational-instability driven turbulence models (Figs 6 and 7). This is consistent with studies finding that gravitational instabilities are the dominant source of turbulence at $1 < z < 3$ (Krumholz & Burkhart 2016; Krumholz et al. 2018; Übler et al. 2019). However, stellar feedback could be a more important driver of turbulence at high-redshift than at cosmic noon and in the local universe (see Section 4.2.2), which could explain the high values of σ_0 that lie above the Toomre marginally stable discs.

We investigate this further, with the relevant results summarized in Appendix D. We first study the relation between σ_0 and the offset from the main sequence $\Delta\mathrm{MS} = \mathrm{SFR}/\mathrm{SFR}_{\mathrm{MS}}$, but find no significant trend (Fig. D2). This is consistent with findings at cosmic noon (Übler et al. 2019) and implies that at fixed stellar masses, galaxies with higher SFRs do not show enhanced σ_0. This lack of enhancement does not support purely stellar feedback driven turbulence. These conclusions do not change if we include only galaxies in the conservative range of $\log(M_\star\ [\mathrm{M}_\odot]) = 9 - 10$. We also find no trend between σ_0 and sSFR_{10}. We explore the placement of galaxies around the MS, in Fig. D3, in relation to their kinematic properties. Although we find no overarching trend, as indicated by the lack of correlations with $\Delta\mathrm{MS}$, it appears that many of the systems with high rotational support $\mathrm{v}/\sigma_0 > 3$ lie close to the main sequence, particularly for the gold sample. An object-by-object analysis is needed to study the link between migrations around the MS and kinematics, but this is beyond the scope of this work.

The observed $\sigma_0 - \mathrm{SFR}_{10}$ correlation ($\rho = 0.42$ and $p < 0.001$) appears more significant than the one between σ_0 and $M_\star$ ($\rho = 0.37$ and $p = 0.001$), which suggests the latter is mainly driven by the SFMS. This is supported by predictions from theoretical models (Pillepich et al. 2019). None the less, the weak correlation between σ_0 and $M_\star$, and the overall distribution of the gold sample points (as seen on Fig. 9) suggests that higher mass galaxies appear to have higher velocity dispersions in our sample. Although this is somewhat physically motivated by the SFMS, it could also be due, in part, to selection effects. The less massive galaxies are typically smaller, so we could be bias to low-σ_0 systems at lower masses because the higher σ_0 systems are too faint (see Section 5.3.1 for further discussion). To investigate this further, we conduct a partial correlation coefficient (PCC) analysis, presented in Appendix B. Although our sample size is small and hence not optimal for this technique, we find that the correlation between σ_0 and v/σ_0 and SFR is more fundamental than that with stellar mass. SFR is also the key driver of the correlation with sSFR_{10}.

Finally, we find that σ_0 weakly correlates with $\Sigma_{\mathrm{SFR}_{10}}$ ($\rho = 0.30$ and $p = 0.007$), although we probe a relatively small range of parameter space. This correlation supports the idea that more compact star-forming systems have increased turbulence, and is consistent with weak correlation between σ_0 and Hα size found in the PCC analysis (Fig. B1).

Interestingly, we find significant negative correlations between v/σ_0 and both stellar mass ($\rho = -0.41$ and $p < 0.001$) and SFR ($\rho = -0.39$ and $p < 0.001$). These negative correlations could be mainly driven by the existing correlations with σ_0, as supported by the fact that the rotational velocities do not strongly correlate with either of these properties (see Fig. D4). The strong dependence on σ_0 is confirmed by the PCC analysis which highlights σ_0 as the main intrinsic correlation. Furthermore, as found for σ_0, SFR is a more important factor than $M_\star$ in determining v/σ_0. As discussed in Section 4.1.1, at fixed stellar masses, galaxies probe a range of kinematic states depending on external influences such as gas accretion and mergers, which can either promote or completely disrupt the formation of the disc. These processes leave imprints on the rotational velocities and can create the observed scatter within

---

[7] We only discuss the correlations and medians for the extended sample, as presented on Fig. 9, but the medians of gold sample follow similar trends.

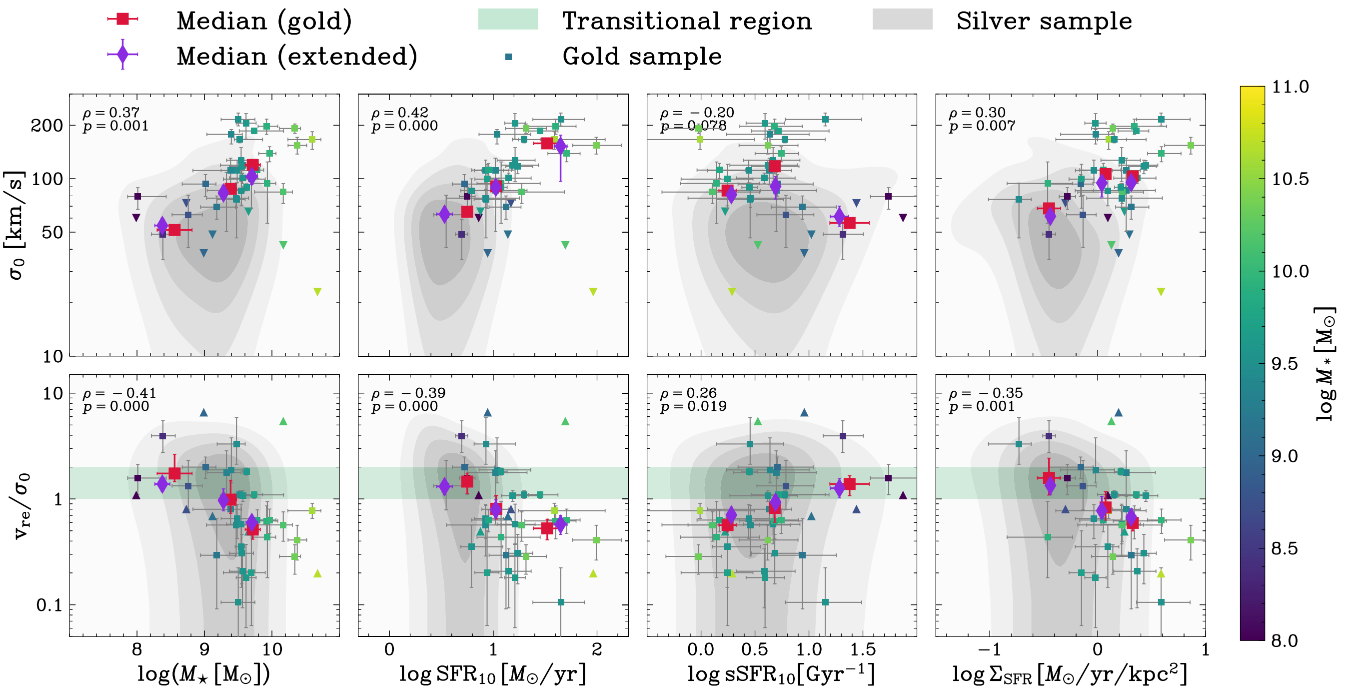

Figure 9. Dependence of the intrinsic velocity dispersion σ_0 (top panels) and rotational support v/σ_0 (bottom panels) on $M_\star$, SFR_{10}, sSFR_{10}, and SFR surface density $\Sigma_{\mathrm{SFR}_{10}}$ for our gold (squares) and silver sample (grey contours). We find a significant correlation between σ_0 and SFR_{10}, which is highlighted by the running medians, for the gold sample (red squares) and for the extended sample (purple diamonds), and the Spearman rank coefficient ρ and p-value p for the resolved sample. Both σ_0 and v/σ_0 show a (weaker) correlation with $\Sigma_{\mathrm{SFR}_{10}}$, highlighting the role of surface density in efficiently driving turbulence in the gas. The trends with SFR_{10} and $\Sigma_{\mathrm{SFR}_{10}}$ are stronger for σ_0 than v/σ_0, which could be caused by the fact that we probing many dispersion-supported systems ($v/\sigma_0 < 1$) and systems in the transitional regions (green shaded region) between dispersion and rotation support, where stable rotation has not yet been established.

galaxies sharing similar masses and star-forming properties. Hence, the measured rotational support v/σ_0 in our sample at $z \sim 4-6$ is mainly driven by the state of turbulence of the gas at the time of observation. As such, we expect that the kinematics of the ionized gas in these galaxies are, on average, not dominated by undisturbed circular motions, as can be seen by the low values of v/σ_0.

From studies out to cosmic noon, we would expect more massive galaxies to be more stable and hence more rotationally supported, which would result in a positive $v/\sigma_0 - M_\star$ relation, as found in many observation and simulation-based works (e.g. Wisnioski et al. 2015; Pillepich et al. 2019; Price et al. 2020). At high redshift, this is not necessarily intuitive given some key differences such as the increased occurrence of mergers and the smaller orbital time-scales. Furthermore, as shown in Tsukui et al. (2025), low-mass galaxies ($M_\star < 10^{10}$ $\mathrm{M}_\odot$) at high-redshift ($z > 1$) are not able to form thin gas discs due to, in part, their high gas fractions, which could also explain the lack of expected correlation.

As we discuss in Section 4.2.2, we would, independent of redshifts, expect a flattening in the v/σ_0-$M_\star$ relation in the lower mass end ($M_\star < 10^{10}$ $\mathrm{M}_\odot$) explored in this work. The medians for both the gold and extended samples hint at such a flattening. The observed decrease, when looking at the gold sample measurements, of v/σ_0 with mass $M_\star$ could be driven in part by observational biases, since, as previously discussed, we may be biased to low σ_0 systems at low masses, which would decrease the number of low v/σ_0 objects detected at low masses. However, this trend is also driven by the higher mass ($\log M_\star[\mathrm{M}_\odot] > 9.3$) dispersion-dominated systems. These systems have very high velocity dispersions $\sigma_0 \sim 100-200$ $\mathrm{km\,s^{-1}}$, not comparable to the similar-mass galaxies seen in the local Universe. It is possible that the highest-mass systems in our sample are the result of recent major mergers, as they probe the tail end of the stellar mass functions at $z \sim 4-6$. Such an event would heavily disrupt the disc and could explain the high σ_0 values measured. It is important to note that this trend decreases in strength and significance ($\rho = -0.12$ and $p = 0.416$) when we only include rotationally supported systems $v/\sigma_0 > 1$ (see Appendix C, including Table C1).

Overall, despite a large scatter in our measurements, we find that σ_0 correlates with star formation already at $z \sim 4-6$. The high values of σ_0 we find could be explained by gravitational instabilities in the disc caused by radial inflows of gas, as well as a potential increase in the role of stellar feedback in injecting turbulence in the ISM.

4.2.2 *Drivers of turbulence across cosmic time*

We now put the correlations we find between kinematic parameters and stellar populations in the context of results reported by other works across redshifts, as shown in Fig. 10. We focus on trends with $M_\star$ and SFR, and compare our running medians to medians from studies of the local Universe (MANGA, Yu et al. 2019; SAMI, Varidel et al. 2020; MUSE, Bacon et al. 2010; Swinbank et al. 2017; Johnson et al. 2018), cosmic noon (KMOS3D, Wisnioski et al. 2015; MOSDEF, Price et al. (2020), SIGMA, Simons et al. 2016; KROSS, Johnson et al. 2018; SINS/zC-SINF AO, Förster Schreiber et al. 2018), and high redshift $z \sim 4-8$ (Parlanti et al. 2023; de Graaff et al. 2024a). We again note that many of these works restrict their analyses to rotationally supported systems $v/\sigma_0 > 1$, which could also reduce the number of systems with high σ_0 in their sample.

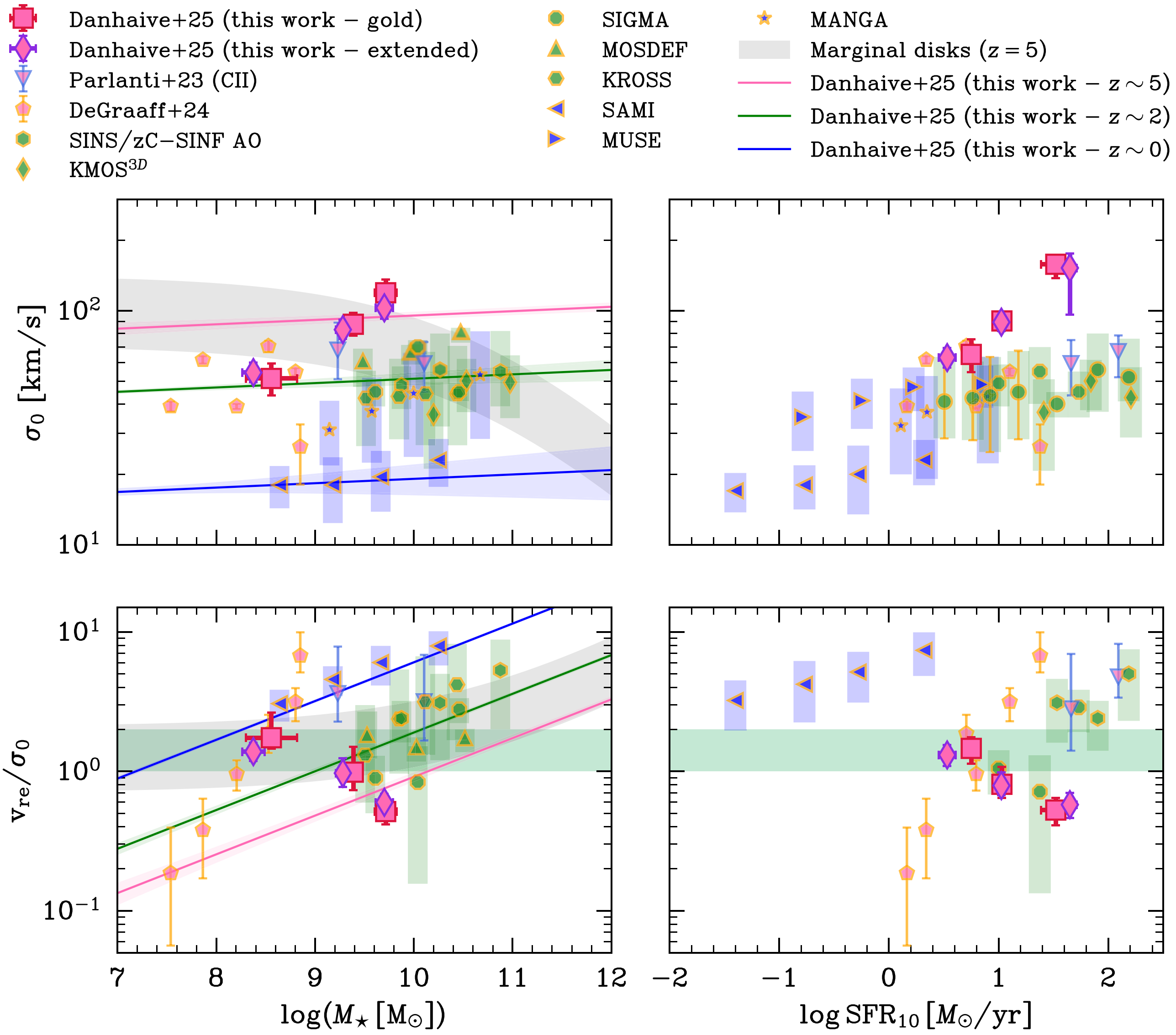

Figure 10. Dependence of σ_0 (top panels) and v/σ_0 (bottom panels) on stellar mass and SFR for our sample (red squares and purple diamonds) in the context of other high-redshift works (in pink; Parlanti et al. 2023; de Graaff et al. 2024a), and works at cosmic noon (in green; see Fig. 7) and the local Universe (in blue; MANGA (Yu et al. 2019), SAMI (Allen et al. 2015; Green et al. 2018; Varidel et al. 2020), and MUSE (Swinbank et al. 2017)). We plot our fit to equation (8) at fixed redshift $z \sim 0$ (blue), $z \sim 2$ (green), and $z \sim 5$ (pink). The σ_0-SFR relation holds across redshifts, for both ionized (Hα; orange outline) and cold ([C II]; blue outline) gas, although we find higher values of σ_0 and a steeper slope. Some works at lower redshift find a similar weak increasing trend for the $\sigma_0 - M_\star$ relation as our sample (Wisnioski et al. 2015; Förster Schreiber et al. 2018; Yu et al. 2019; Price et al. 2020), while Simons et al. (2017) finds no significant trend. The trends for v/σ_0 are less clear, but our results could indicate a flattening in the v/$\sigma_0 - M_\star$ relation at low masses $\log M_\star[\mathrm{M}_\odot] \lesssim 10$, which is consistent with other works in this mass range and which is predicted by the marginal disc model (grey shaded regions).

We compute correlations for the v/$\sigma_0 > 1$ galaxies in our sample and find no qualitative difference, although the significance of the correlations slightly varies (Table C1).

As shown by the colour-coding of the points by approximate redshift, our measurements of $\sigma_0 \approx 50$–$150\,\mathrm{km\,s^{-1}}$ lie on average above values at cosmic noon (green) $\sigma_0 \approx 30$–$70\,\mathrm{km\,s^{-1}}$, as well as measurements from the local Universe (blue) $\sigma_0 \approx 10$–$50\,\mathrm{km\,s^{-1}}$ which have the lowest dispersions on average (see also Fig. 7).

We discussed in Section 4.2.1 that the $\sigma_0 -$ SFR correlation is predicted by theoretical models in which gravitational instabilities and feedback drive turbulence in the disc. These processes act at all redshifts, and explain why we observe this trend in all the surveys shows in Fig. 10. In the local Universe, several studies find a significant positive correlation of σ_0 with SFR and Σ_{SFR} (Arribas et al. 2014; Yu et al. 2019; Law et al. 2022). These trends seem to hold out to cosmic noon, albeit with higher observed velocity dispersions and weaker correlations, indicative of a turbulent ISM (Förster Schreiber et al. 2009; Genzel et al. 2011; Wisnioski et al. 2015; Simons et al. 2017; Johnson et al. 2018; Übler et al. 2019; Price et al. 2020). In our work, we find that this trend is already in place at $z \sim 4 - 6$.

Also, the turbulence induced by these processes is expected to increase with redshift as galaxies are on average less massive, becoming less stable to gravitational instabilities and disruptions from stellar feedback (Nelson et al. 2019; Pelliccia et al. 2020). The overall decrease of gas fractions with cosmic time also promotes the decrease of turbulence in the ISM (van Donkelaar, Agertz & Renaud 2022), as studies have shown that at high gas surface densities, and high SFR surface densities (Rathjen et al. 2023), the turbulence injected into the ISM from supernovae explosions can rise from $\sigma \sim 5 - 20$ km s^{-1} (Krumholz et al. 2018) to $\sigma \sim 50 - 60$ km s^{-1} due to strong stellar feedback (Hopkins, Quataert & Murray 2011) and high gas fractions (Gatto et al. 2015). All of these factors could explain why the σ_0 − SFR trend is steeper, and has a higher normalization, at high redshift.

The plotted medians from Parlanti et al. (2023) are from measurements of cold gas, which tend to have factors of 2 − 3 lower velocity dispersions (Übler et al. 2019; Rizzo et al. 2024). We also plot the six galaxies from de Graaff et al. (2024a), which probe the low-mass end.

Our observed dependence of σ_0 with $M_\star$ is overall in agreement with past works, which find a weak positive (Wisnioski et al. 2015; Turner et al. 2017b; Förster Schreiber et al. 2018; Yu et al. 2019; Übler et al. 2019; Price et al. 2020) or non-existent (Simons et al. 2017) correlation, although steeper in slope. The intrinsic correlation between stellar mass and SFR, i.e. the SFMS, implies that the σ_0-SFR relation could explain most of the trend observed with stellar mass. At lower redshifts, many attribute the more fundamental correlation to SFR instead of $M_\star$ (Wisnioski et al. 2015; Yu et al. 2019).

We compare observational measurements to predictions from the marginal disc model at $z = 5$, and find this empirical framework predicts a negative relation between σ_0 with $M_\star$. This is in contrast with findings across cosmic time on Fig. 10, which show a flat or increasing trend. The Toomre marginal disc model (equation 9) describes σ_0 based on gas fractions, which are expected to decrease with mass. The observed increase of σ_0 with $M_\star$ suggests either higher gas fractions, than predicted by the model, at high masses, or significant contributions from other sources of turbulence. To better quantify this difference between the data and this model, we plot on Fig. 10 our best-fitting relations, described in Sections 4.1.2 and 4.1.3, of equation (8) at fixed redshifts. We fit our sample in conjunction with the SAMI and KMOS3D surveys, and find that at fixed redshift the mass dependence of σ_0 is very weak. This appears to be driven by the lower redshift samples, as our medians show a steeper slope than the best-fitting relation at $z \sim 5$ (pink curve). Importantly, our best-fitting relations are in contrast with the predictions from the marginal disc model, and are consistent with a flat or rising slope.

The results for v/σ_0 are more difficult to interpret. Starting with the $v/\sigma_0 - M_\star$ relation, it is difficult to conclude on an overarching trend that holds at all masses. Our sample of galaxies at $z \sim 4 - 6$ probes lower masses than lower redshift counterparts, but lies slightly above the masses from de Graaff et al. (2024a). The works from the local Universe to cosmic noon have reported positive correlations, albeit with varying strengths. However, as can be seen on Fig. 10, the trend weakens below $\log M_\star[\mathrm{M}_\odot] \sim 9.5$, and the medians appear to flatten. In fact, we find a significantly shallower mass dependence (equation 8, $\beta = 0.15 \pm 0.02$) when fitting galaxies with $\log M_\star[\mathrm{M}_\odot] < 9.5$ than when fitting the full samples ($\beta = 0.28 \pm 0.01$ as reported on Table 4). The medians from Parlanti et al. (2023) also show no strong evolution between $\log M_\star[\mathrm{M}_\odot] \sim 9 - 10$. Overall, the different regimes in which the positive $v/\sigma_0 - M_\star$ relations holds remain unclear, but this work provides evidence that the dependence of v/σ_0 on $M_\star$ weakens at lower masses. This is in line with predictions from the marginal disc model (equation 9), as is also discussed in Simons et al. (2016).

Similarly to the $v/\sigma_0 - M_\star$ correlation, we find that our negative v/σ_0-SFR correlation is in contrast with measurements from cosmic noon on Fig. 10. As discussed in Section 4.1.3, we find evidence that this is driven by the evolution of σ_0 with SFR. However, we probe lower SFRs and overall more turbulent systems than studies at than cosmic noon, and given the large scatter in our measurement, we cannot draw a strong conclusion.

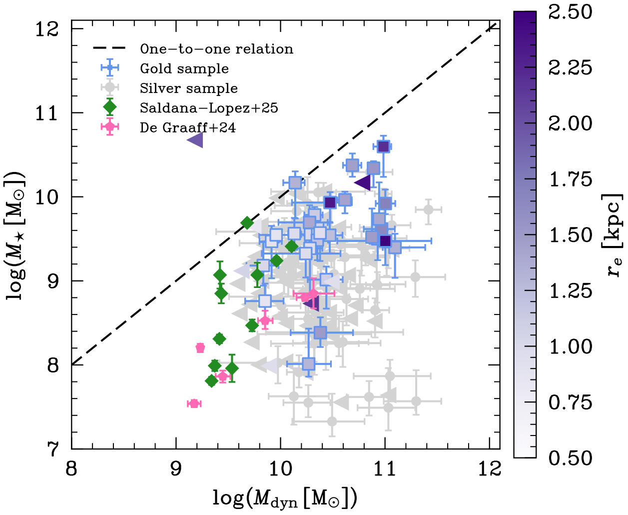

Figure 11. Comparison of the dynamical masses ($M_{\rm dyn}$) inferred from grism data and the stellar masses ($M_\star$) inferred from SED fitting for our gold (blue squares), colour-coded by Hα size, and silver (grey circles) samples. The majority of our systems lie below the one-to-one relation (dashed line), consistent with a significant contribution to the dynamical mass from gas and/or dark matter. Six galaxies lie on the relation, potentially highlighting underestimated uncertainties on σ_0 (see Section 5.3.1). We compare our values to ionized gas measurements from de Graaff et al. (2024a) and Saldana-Lopez et al. (2025).

4.3 Comparing stellar masses and dynamical masses

Using the results from our kinematic modelling, we are able to compute dynamical masses for the objects in our sample. Dynamical masses offer insights into the dark matter content of galaxies, but for the scope of this work we only discuss them in the context of a comparison with stellar mass. We defer a detailed study of the dark matter and baryonic mass contents of our sample to a follow-up paper (Danhaive et al, in preparation).

We use our posteriors inferred with GEKO to compute the posterior distribution of the dynamical mass for each system using equations (6) and (7). Equation (7) assumes that the system is in virial equilibrium and that the measured velocity gradient is not probing non-circular motions such as outflows. In Fig. 11 we compare the dynamical masses $M_{\rm dyn}$ inferred from grism data to the PROSPECTOR stellar masses inferred from SED modelling. We expect the dynamical masses to lie above the stellar masses, as they should also incorporate the gas and the dark matter. However, both methods of inferring masses suffer from uncertainties (as can be seen from the large error bars) and caveats, so comparing the two offers a good benchmark to understand how reliable both estimates are. We note that comparing the masses, both dynamical and stellar, within the effective radius instead of estimating their total values does not affect the observed trends.

Fig. 11 shows a large scatter in dynamical masses, indicating varied kinematic states and gas (and dark matter) fractions. We plot points from de Graaff et al. (2024a) for comparison, which lie well below the one-to-one relation, indicative of high gas and dark matter fractions, and points from Saldana-Lopez et al. (2025) which span a wider range.

We find consistent measurements $M_\star < M_{\rm dyn}$ for the majority of the galaxies in our sample, with the exception of 5 systems which lie above or on the one-to-one relation. It is difficult to evaluate the cause for this discrepancy, as it could be due to the SED fitting, the kinematics fitting, or a mixture of both. We discuss possible sources of error in the stellar mass estimate in Section 5.3.2. For systems σ_0 is only an upper limits, the measurement of $M_{\rm dyn}$ is more uncertain. For example, we could be underestimating the uncertainties on our σ_0 measurements, which has a large impact on the derived upper limits (Section 5.3.1). If the velocity dispersions are underestimated, this would propagate to the dynamical masses and cause the observed discrepancy in these systems.

We find an interesting system (JADES ID: 1082948) that is among the most massive in our sample, with $\log(M_\star\ [\mathrm{M}_\odot]) = 10.6^{+0.1}_{-0.2}$, and yet shows no signs of rotation, resulting in a low dynamical mass of $\log(M_\star\ [\mathrm{M}_\odot]) = 8.9^{+0.4}_{-0.6}$. We investigate possible reasons for this discrepancy. Regarding the kinematic modelling, although we find a good fit of the model to the data, there could be a faint, broad Hα component that isn't being modelled well due to the overpowering brighter central region. Also, the best-fitting results from PROSPECTOR show, despite the large uncertainties, that the galaxy has a declining SFH since the last ~ 20 Myr, after peaking at SFR $\sim 270\ \mathrm{M}_\odot\ \mathrm{yr}^{-1}$. This galaxy could be in a quenching epoch, as it also has a relatively small UV size, $r_{\rm e} = 1.5$ kpc, for its mass, lying below the predicted relations at $z \sim 4$ (Allen et al. 2025; McClymont et al. 2025b). However, it lies close to the SFMS (Fig. 2), so its star formation is decreasing following a burst and it may now be entering a quenching episode. The imaging indicates that this galaxy could be in a post-merger phase. This system passed our visual inspection, where we discarded close pairs as mergers, because the clumps were too close to classify it as a merger.

5 DISCUSSION

Extensive studies of galaxy kinematics from the local Universe to cosmic noon have shown that the star-forming galaxy population evolves from gas-rich star-forming thick discs at $z \sim 2-3$ to dynamically cold thin discs by $z \sim 0$. Despite their increased turbulence (Glazebrook 2013; Wisnioski et al. 2015; Übler et al. 2019; Förster Schreiber & Wuyts 2020; Rizzo et al. 2024), the thick discs at cosmic noon can be described by many of the same key scaling relations, between kinematics and star formation related quantities, that are in place at $z \sim 0$, albeit with some offsets and a larger scatter (e.g. Tiley et al. 2016; Price et al. 2020; Übler et al. 2017; Sharma et al. 2024).

Our work at $z \sim 3.9-6.5$ shows that in the earlier stages of galaxy formation, the picture becomes complex. As we attempt to bridge the gap between the Epoch of Reionization (EoR) and cosmic noon, it is important to remember the importance of stellar mass. Studies from $z \sim 0$ to $z \sim 3$ predominantly probe galaxies with $M_\star \gtrsim 10^{10}\ \mathrm{M}_\odot$, with the typical sample distribution peaking around $M_\star \sim 10^{11}\ \mathrm{M}_\odot$ and $M_\star \sim 10^{10.5}\ \mathrm{M}_\odot$, respectively. At $z \sim 4-6$, we have a galaxy population dominated by systems in a lower mass slice of the parameter space $M_\star \sim 10^8 - 10^{10}\ \mathrm{M}_\odot$. Careful consideration must therefore be given to separate pure redshift evolution from evolution mainly driven by stellar mass.

Studies have shown that even at high redshifts $z \sim 4-5$, some galaxies with stellar masses $\log M_\star[\mathrm{M}_\odot] \gtrsim 10$, comparable to those probed by the star-forming population at cosmic noon, are already able to settle into stable rotating discs (e.g. Neeleman et al. 2020; Lelli et al. 2021). However, it is not surprising that many of the low-mass systems at high redshift are turbulent and have not settled into a stable rotationally supported state (Fig. 8). Their ISM is characterized by elevated velocity dispersions (Fig. 7), which are likely driven by increased gravitational instabilities promoted by their lower masses, high gas fractions, and the overall increase of mergers and starbursts in the early Universe. These instabilities, along with a potential contribution from stellar feedback, drive the observed correlations between SFR, and SFR surface density, and σ_0 (Fig. 9).

Overall, the picture painted in this work is consistent with galaxies at high redshift being turbulent and changing on short time-scales. In this case, we expect the prevalence of discs to be lower at $z \gtrsim 4$ than in the local Universe and at cosmic noon. We investigate and discuss this in the next section.

5.1 The prevalence of discs at $z > 4$

With recent *JWST* and ALMA observations finding disc-like systems in the early Universe ($z > 4$; e.g. Lelli et al. 2021; Pope et al. 2023; Rowland et al. 2024), questions arise as to how these systems are able to form and stabilize in the turbulent, high-redshift environment. To answer the question of how representative these massive rotating discs are of the high redshift star-forming galaxy population, we investigate the fraction of rotationally supported systems $\mathrm{v}/\sigma_0 > 1$ in our sample and place it in the context of lower redshift measurements (Fig. 12). Without spatially resolved velocity maps (such as those obtained with IFUs), it is difficult to classify systems as discs and to compute a disc fraction. This is highlighted by recent resolved studies at high redshift, which find rotationally supported discs that are heavily perturbed by non-circular motions (Arribas et al. 2024; Übler et al. 2024; Tsukui et al. 2024). This motivates our choice of not defining a disc fraction but instead focusing solely on the evolution of the fraction of rotationally supported systems $\mathrm{v}/\sigma_0 > 1$ across cosmic time. However, we require systems to have kinematic and morphological PAs that are relatively aligned $|\mathrm{PA}_{\rm kin} - \mathrm{PA}_{\rm morph}| < 30°$. From our original full sample of Hα emitters in the FRESCO and CONGRESS surveys, we remove all low S/N galaxies (S/N<10), all galaxies with a PA too close to the grism dispersion direction, and all galaxies which are spatially and/or rotationally unresolved. This cut excludes all galaxies that are not in our gold or silver samples (Section 2.3). We focus on the stellar mass range $9 < \log M_\star[\mathrm{M}_\odot] < 10$ where our sample is most representative of the star-forming galaxy population (Fig. 2).

We also need to quantify a fraction of merging systems, which cannot be modelled with our single-component approach (see Section 3.3). This includes both minor and major mergers, and could include clumpy systems that resemble mergers. We select systems with small separations $r_{\rm max} \sim 10$ kpc ($r \lesssim 1.5''$) as mergers, since the single component modelling would not be contaminated by pairs with larger separations. This differs from in-depth studies of merger fractions, which include much larger separations $r_{\rm max} \sim 30-50$ kpc (Duncan et al. 2019; Duan et al. 2025; Puskás et al. 2025). In order to consistently measure the pair fraction in our sample, we exclude

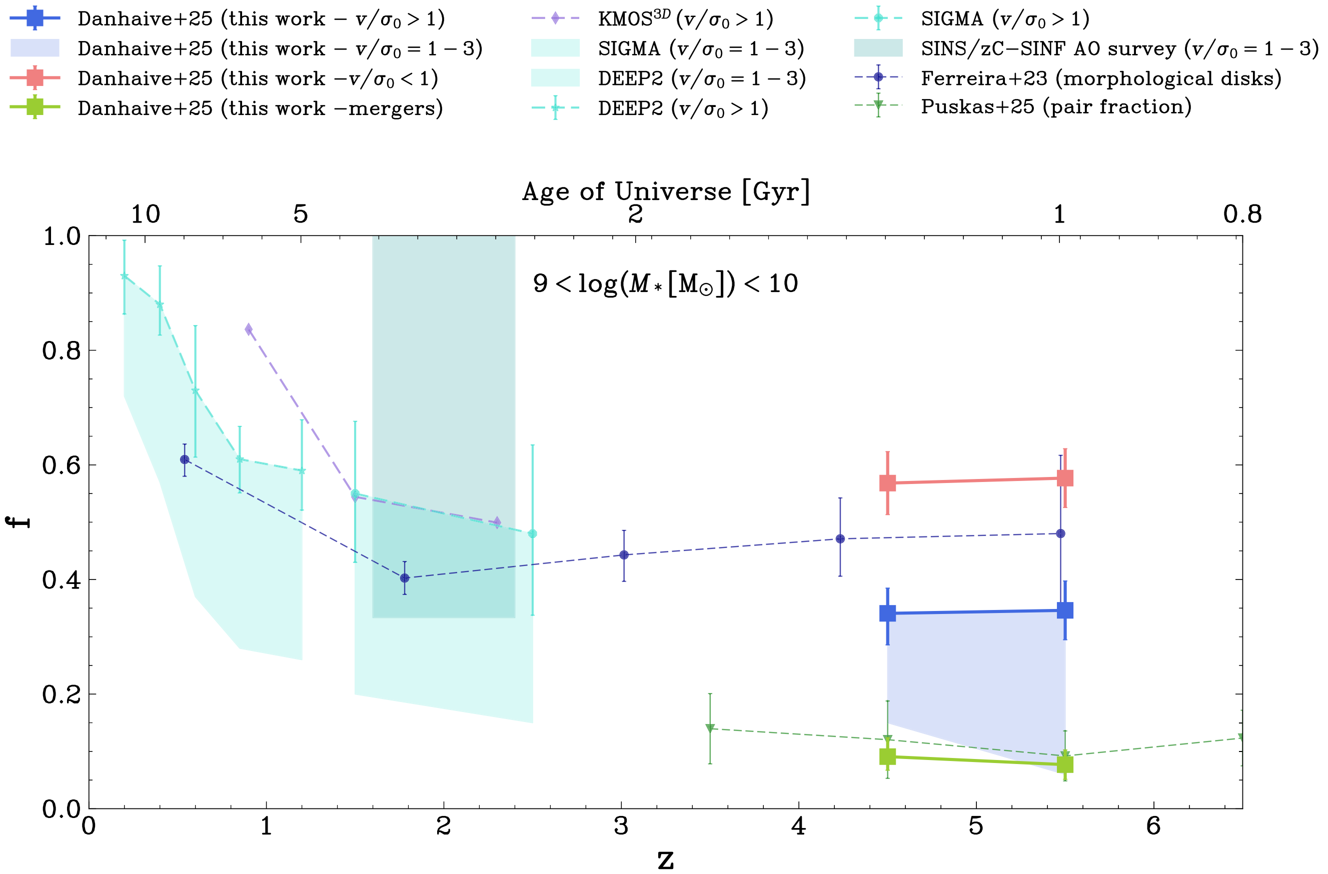

Figure 12. Evolution of the fraction of rotationally supported systems ($v/\sigma_0 > 1$) with redshift for our sample (blue lines) and for kinematic samples (Simons et al. 2017; Förster Schreiber et al. 2018; Wisnioski et al. 2019) and morphological sample (Ferreira et al. 2023) from the literature (blue dashed lines). We find a decrease in the fraction of systems with rotational support with redshift, consistent with predictions from lower redshifts, with fractions significantly lower if we consider a more conservative cut of $v/\sigma_0 > 1-3$ (blue shaded regions), with the lower edge at $v/\sigma_0 > 3$. This result contrasts the (on-average) constant fractions reported by Ferreira et al. (2023). We compare the fraction of pairs (green line), which we discard from our kinematic analysis, to the one reported in Puskás et al. (2025) (green dashed line), and find broadly consistent results.

galaxies which would have not made the cut for kinematic modelling, i.e. galaxies with a low S/N and galaxies with $|\mathrm{PA}_{\mathrm{morph}}| > 75°$ (Section 2.3).

In our sample, we find that the fraction of rotationally supported systems, $f = 0.34 \pm 0.05$, does not vary between $z \sim 5.5$ to $z \sim 4.5$. This fraction drops significantly, to $f = 0.06 \pm 0.03$ and $f = 0.15 \pm 0.04$ at $z \sim 5.5$ and $z \sim 4.5$, when considering systems with $v/\sigma_0 > 3$. This highlights that although a considerable fraction of the galaxies in our sample are rotationally supported, the majority of these systems are found in the transitional region of $v/\sigma_0 = 1-3$. These systems could be starting to build rotational support through co-planar accretion of gas, or conversely could have just undergone a merger or radial accretion event, which has disrupted the formation of a rotating disc. Only a small fraction $f \lesssim 0.1$ of systems has significant rotational support, indicating that disc-like galaxies do not dominate the galaxy population at $z > 4$ at stellar masses $9 < \log M_\star[\mathrm{M}_\odot] < 10$, but that dispersion-supported systems are common.

When placed in the context of works at lower redshift $z < 4$ (Simons et al. 2017; Förster Schreiber et al. 2018; Wisnioski et al. 2019), our results are consistent with a continued decline of rotationally supported systems with redshift. In fact, both Wisnioski et al. (2019) and Simons et al. (2019) find a decrease from $f \approx 0.8-0.9$ at $z < 1$ to $f \approx 0.5$ by cosmic noon ($z \sim 2-3$). The sample from (Förster Schreiber et al. 2018) only contains rotationally support systems, so $f = 1$, but we plot the evolution to $v/\sigma_0 > 3$ as a shaded region in Fig. 12. Our measured fractions of rotationally supported at $z > 4$ lie below the medians from these three samples at cosmic noon, although (Simons et al. 2017) report large errors which overlap our own measurements. We note that these samples from cosmic noon are more sensitive to higher masses $\log M_\star[\mathrm{M}_\odot] > 10$ and hence have a reduced number of galaxies in the mass range we consider here. This overall increase is consistent with Pandya et al. (2024) who classify systems from $z = 0.5-8$ based on their 3D geometry and find an increase of oblate (discy) systems with cosmic time. In their highest redshift bin $z = 3-8$, they find that the fraction of oblate systems is $f \sim 0.2-0.4$ (depending on the modelling technique chosen) for galaxies with stellar masses $\log(M_\star\,[\mathrm{M}_\odot]) \sim 9.25-9.75$.

When compared to the morphological analysis of disc fractions conducted in Ferreira et al. (2022, 2023), we find lower fractions across both redshift bins. However, their work does not apply an upper mass cut-off, as we do here, so this could introduce a bias. More importantly, our fraction of rotationally supported systems is not equivalent to a disc fraction, as shown in part by the significant decrease when considering a higher threshold for rotational support.

We also find that only a fraction of ~ 0.33 of our rotationally supported sample has an Hα morphology with a Sérsic index $0.5 < n < 1.5$, consistent with the exponential profiles we see in local discs. Although systems with $0.5 < n < 1.5$ represent the peak of the n distribution, we find a long tail with rotationally supported systems having Sérsic indices $n \sim 2 - 7$. The wide range of n values offers insight into the perturbed morphologies of galaxies at $z \gtrsim 4$, making it more difficult to identify rotating discs akin to those seen in the local Universe. This is further supported by the predominantly low values of v/σ_0 we find, with ≈ 65 per cent of the rotationally supported systems having $\mathrm{v}/\sigma_0 < 3$. These galaxies could drop out of $\mathrm{v}/\sigma_0 > 1$ disc criterion on short time-scales if enough momentum is injected in their ISM, for instance through a merger, a starburst, or a disruptive accretion event.

Alongside the fraction of discs, we also plot in Fig. 12 our merger fraction obtained from the visual inspection of images of the galaxies in our sample, and compare it to the major merger pair fractions derived in Puskás et al. (2025) (see also Duan et al. 2025). We find excellent agreement, which offers a sanity check for our visual inspection. However, we note that our merger fraction selection differs from that of Puskás et al. (2025). As mentioned above, we probe significantly smaller separations, and in terms of merger time-scales, which quantify how long galaxies appear as pairs, we find that our separation $r_{\max} \sim 10$ kpc implies time-scales of $T_{\mathrm{mg}} \sim 0.3 - 0.5$ Gyr for $\log(M_\star\ [\mathrm{M}_\odot]) = 9 - 10$ at $z = 5$, whereas the separation $r_{\max} \sim 30$ kpc from Puskás et al. (2025) probes time-scales of $T_{\mathrm{mg}} \sim 1.4 - 2.2$ Gyr for the same masses and redshift. These values are derived from a fitting formula based on cosmological dark matter simulations (Huško, Lacey & Baugh 2022). Also, Puskás et al. (2025) only select major mergers (mass ratio $> 1/4$), whereas we include systems with smaller mass ratios as well. We note that our fraction of mergers is low $f \lesssim 0.15$, so discarding these systems does not strongly affect our inferred fractions or the main conclusions of this work.

Overall, the strong decrease of the fraction of disc-like systems from $z < 1$ to $z = 6$ suggests that the majority of the galaxy population only settles into cold discs during and after cosmic noon, when the bulk of the stellar mass is formed. The fraction of rotationally supported systems increases from $z \sim 6$ until the start of cosmic noon $z \sim 2.5 - 3$, where this fraction becomes $f \gtrsim 0.5$, and disc-like galaxies begin to dominate the galaxy population.

5.2 Implications for galaxy evolution across cosmic time

We will now discuss how this work fits into the more global evolution of galaxies and propose explanations for the observed turbulence at high redshift. In Fig. 13, we show a schematic view of our understanding of galaxy evolution from a dynamical point of view, tracing the evolution of local Universe galaxies with $\log M_\star[\mathrm{M}_\odot] = 9, 10, 11$ and 12 back in time by integrating the main sequence from Simmonds et al. (2025), which is consistent with predictions from simulations (Tacchella et al. 2016a; McClymont et al. 2025a). We then colour the $M_\star - z$ plane by gas fraction f_{gas} following the relation from Tacconi et al. (2020).

In the local Universe, most star-forming galaxies have settled into discs, which are increasingly thin at higher masses, as highlighted by stellar kinematics (van der Wel et al. 2014; Cappellari 2016). On the higher mass end, some galaxies have quenched, and their rotational support decreases as they compress and their sizes decrease. At cosmic noon, the star-forming population is predominantly made up of gas-rich thick discs, with the fraction of rotationally supported systems, based on ionized gas measurements, dropping by ~ 30 per cent from $z \sim 0$ for galaxies with stellar masses $9 < \log M_\star[\mathrm{M}_\odot] < 10$ (Fig. 12). As drawn in Fig. 13, these thick discs only settle in dynamically cold discs below $z \sim 1$, which also coincides with a decrease in gas fractions to below $f_{\mathrm{gas}} \lesssim 0.5$. Because of the dependence of gas fractions on stellar mass, this happens sooner for higher-mass systems, which could promote the formation of thin discs with $M_\star \sim 10^{11}\,\mathrm{M}_\odot$ at cosmic noon (Wisnioski et al. 2015; Price et al. 2020). However, mass itself is a key factor in disc formation, as more massive galaxies are more stable to gravitational instabilities, especially when the mass profile becomes centrally concentrated (Hopkins et al. 2023). Even at high gas fractions, massive galaxies can settle into discs if the gas accretion is somewhat smooth. In fact, Dillamore et al. (2024) find that halo mass is an important driver disc formation, which occurs roughly at the mass where galaxies transition from cold- to hot- mode accretion.

With the arrival of *JWST*, we are now able to further constrain the kinematics of galaxies beyond $z \sim 4$ and complement the view of cold gas kinematics from ALMA. The picture that has been constructed in this work, and is supported by other works at high redshift (Parlanti et al. 2023; Arribas et al. 2024), is one of a turbulent epoch of early galaxy formation. Galaxies at masses below $M_\star \sim 10^{10}\,\mathrm{M}_\odot$ are characterized by high gas fractions $f_{\mathrm{gas}} \gtrsim 0.7 - 0.8$, which increase at low masses (Danhaive et al., in preparation.). Although the gas fractions are mildly lower at higher masses, it is likely that the highest-mass systems in our sample have recently undergone mergers. In fact, Puskás et al. (2025) shows that merger fractions at $z \sim 4 - 6$ are high, with $2 - 10$ major mergers per Gyr, and it is therefore reasonable to expect that the higher-mass systems were able to form quickly through major or minor mergers. This would justify why we find many dispersion-dominated systems on the massive end, as mergers can increase turbulence in the ISM and also boost star formation through gas inflows.

At lower masses, $\log M_\star\ [\mathrm{M}_\odot] \lesssim 9.5 - 10$, galaxies become more unstable to disruptions from gravitational instabilities and star formation. Specifically, as also discussed in de Graaff et al. (2024b), simulations predict that stellar feedback starts to play an important role in this mass range, with mass loading factors for stellar winds and supernovae reaching values ~ 30 times larger for low-mass ($\log M_\star\ [\mathrm{M}_\odot] \sim 8$) galaxies than for high-mass ($\log M_\star\ [\mathrm{M}_\odot] \sim 11$) galaxies (Nelson et al. 2019). The shallow potential wells of low-mass galaxies, compared to high mass galaxies, promote outflows as they need less energy to be driven out of the galaxy (Bassini et al. 2023). Recent observational works are consistent with this view, detecting strong outflows in low-mass galaxies out to $z \sim 9$ (Carniani et al. 2024; Zhang et al. 2024). The shallow potential wells of low-mass galaxies also promote inflows of gas that reach the central regions of the galaxy (Dekel & Burkert 2014; El-Badry et al. 2016; Tacchella et al. 2016b; Hopkins et al. 2023; McClymont et al. 2025a). As the gas compacts, it triggers bursts of star formation, whose strong feedback can expel a lot of the remaining gas. These bursts are hence regulated by inflows and outflows, which disrupt disc formation and inject turbulence in the ISM, sustaining high velocity dispersions. Such processes perturb disc formation through misaligned accretion and spin flips (Dekel et al. 2020; Sales et al. 2012).

Many galaxies in our sample have rotational support $\mathrm{v}/\sigma_0 \sim 2$ akin to massive quiescent galaxies at $z \sim 1 - 2$ (Newman et al. 2018; Ji & Giavalisco 2024), found from studies of stellar kinematics, which show slow rotation. This population is distinct from quiescent galaxies which appear to be still be sustaining rapid rotation (D'Eugenio et al. 2024). Some of the galaxies we present here could be progenitors of these slow rotators, without having to undergo

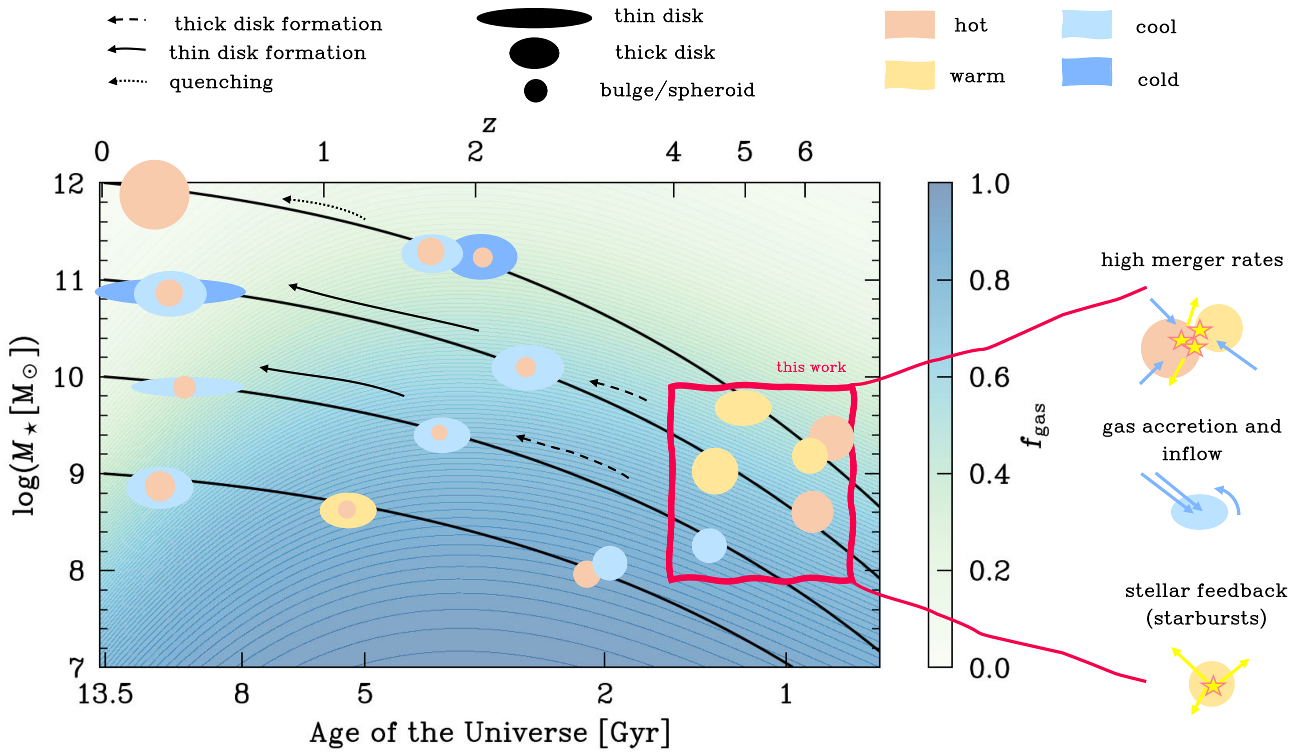

Figure 13. Schematic view of the dynamical evolution of galaxies from $z \sim 8$ to the local Universe, placing the results of our work (red square) in this broader picture. Galaxies are colour-coded by dynamical state, from cold ($\mathrm{v}/\sigma_0 \gtrsim 1$; blue) to hot ($\mathrm{v}/\sigma_0 \lesssim 1$; orange), and shaped according to their thickness/disciness. We show that as galaxies evolve along the main sequence (black curves), they settle into disc-like systems once they reach small enough gas fractions (inferred by the Tacconi et al. 2020 relation), which depend on both mass and redshift. In the redshift and mass range probed by this work, galaxies are gas-rich and have a turbulent ISM, with high velocity dispersions driven by instabilities caused by mergers, gas inflows, and feedback from star formation.

much dynamical transformation. However, it is also likely that many of them will evolve around the main sequence, build up their mass, and build rotational support through accretion of cold gas, becoming the star-forming discs we observe at cosmic noon. Because of the high merger rate at these redshifts, many of these galaxies will undergo numerous major mergers before being able to settle into discs.

Overall, the systems we study in this work are turbulent galaxies in their early stages of formation. Although disc settling is promoted through the smooth accretion of gas with conserved angular momentum, the low masses, high gas fractions, and high merger rates characteristic of the high redshift Universe ($z > 4$) favour bursty and clumpy star formation. Simulations predict that bursty star formation in the early universe hinders disc formation, and the transition from bursty to smooth star formation coincides well with the transition from dispersion-dominated systems to discs (Hopkins et al. 2023; Semenov et al. 2025b).

5.3 Caveats

5.3.1 *Modelling and observational biases*

In the development of GEKO, we have performed recovery tests to understand how robust the constraints are that can be placed on the kinematics in different scenarios, mainly focusing on the orientation of the galaxy with respect to the dispersion direction (PA), the intrinsic kinematics of the galaxy, and the S/N. The key results from these tests are summarized in the Appendix E, but the full description of the code and the tests will be done in Danhaive et al. (in preparation). Specifically, Figs E1 and E2 highlight the uncertainties in the velocity dispersion measurement. It is important to note that grism observations inherently provides a weaker constraints on kinematics than IFU observations, which have been used for measurements in the local Universe (e.g. Law et al. 2022), at cosmic noon (e.g. Genzel et al. 2011; Wisnioski et al. 2015; Stott et al. 2016; Förster Schreiber et al. 2018), and out to $z \approx 11$ with the *JWST*/NIRSpec IFU (e.g. Marconcini et al. 2024; Scholtz et al. 2024; Venturi et al. 2024). This is first due to the line spread function, which in the *F444W* band is $R \sim 1600$, meaning a kinematic resolution of about $\Delta v \sim 80\ \mathrm{km\,s^{-1}}$. Even though we are able to constrain the velocity dispersion below Δv in certain favoured scenarios (e.g. high S/N, see Fig. E1), we still suffer from large uncertainties, especially at the low-σ_0 end, where we can often only place upper limits. Finally, the LSF is calibrated from *JWST* Cycles 0, 1, and 2 observations, and has an average uncertainty of 10 per cent. We do not marginalize over this uncertainty in the inference framework, which could boost errors by a factor of up to 1.5 (for the lowest values of σ_0). The boost is minimal for dispersions larger than the LSF. This is particularly important when the velocity dispersion is only measured as an upper limit, since increasing the errors would automatically increase the value of the inferred upper limit.

Our choice of an arctangent velocity curve model instead of other common functions such as the exponential disc model (Freeman 1970; Wisnioski et al. 2011; Genzel et al. 2017) should not strongly affect our measurements since the grism data does not probe the large radii where these curves differ (see also discussion in Price et al. 2020). Furthermore, the nature of the grism data is the morphology–kinematics degeneracy along the dispersion direction, which is the entire motivation behind GEKO. This means that our constraints are inferred from modelling, which comes with its own assumptions, and are not 'directly' measured. Instruments like IFSs benefit from two spatial axes, where grism only has one,[8] which allows them to have better constraints on the spatially resolved kinematics without strong priors on the emission-line maps or dynamical models.

While it is important to keep all of this in mind, the grism remains a crucial tool for studying the statistical properties of high-redshift galaxies. The power of Bayesian inference is in fully tracking uncertainties using the posterior distributions, which allows us to be realistic about the constraints we are making and the conclusions we are drawing for them.

There are additional caveats that we discuss in terms of the biases they could introduce. The first is related to spatial resolution, as it is difficult to distinguish tightly merging galaxies from discs, and the former are hence often misclassified as discs (Simons et al. 2019). This is one of the reasons why strict criteria need to be applied to define discs. It is also important to note that most of the galaxies in our sample are of relatively low mass: $M_* < 10^{10}\,\mathrm{M}_\odot$, and we could be sensitive to non-circular motions. Their low masses and high gas fractions make them much more sensitive to stellar feedback, and combined with their turbulence and low rotational support, it is possible we are probing outflows alongside rotational velocities. This could bias our sample to high v/σ_0 at low masses, especially since the low masses systems are typically smaller and have less resolution elements. In general, if the thin-ish disc assumption underlying our models does not hold, it becomes difficult to interpret our measurements, especially the correlations. However, the main conclusion of turbulent ionized gas kinematics at $z \gtrsim 4$ would still hold, since high enough rotational support would dominate any contribution from these effects. Overall, caution must be exercised when trying to categorize such systems as discs, even if rotationally supported, and this is why we do not draw conclusions about the fraction of discs but only that of rotationally supported systems. This fraction could however be overestimated if the measured velocities do not come from rotation.

In our kinematic modelling, we assume that the velocity dispersion is isotropic and radially constant. However, some spatially resolved studies at lower redshift find a correlation between the local σ_0 and the local Σ_{SFR} (Yu et al. 2019; Law et al. 2022). In cases of clumpy star formation, which are predicted to be more common at higher redshift (Nakazato et al. 2024; Tan et al. 2024), the constant σ_0 assumption may not hold as well. However, other works report no correlation in systems with highly star-forming clumps (e.g. Übler et al. 2019). Finally, although many studies show central peaks of velocity dispersion, an intrinsically flat σ_0 profile is often recovered when beam smearing effects are accounted for in the kinematic modelling (e.g. De Breuck et al. 2014). A centrally peaked σ_0 could bias our measurements to higher values when compare to studies that measure the intrinsic σ_0 in the outskirts (e.g. Wisnioski et al. 2015)

Furthermore, our calculation of the rotational velocity is based on inclination corrections to the observed velocity, for which we need to assume an intrinsic thickness of the disc (we assume $q_0 = 0.2$). If the value of q_0 is overestimated (underestimated), the inferred dynamical masses could be up to ~ 0.02 dex higher (lower) than the fiducial ones. This does not affect our conclusions, but could help reconcile some of the unphysical measurements in Fig. 7. We also note that the inclination of the galaxy is expected to affect the velocity and velocity dispersion measurements. For σ_0, this is because the line-of-sight dispersion we measure is a mixture of its radial σ_R and vertical σ_z component, and as the galaxy becomes inclined we go from measuring predominantly σ_z in face-on systems to measuring predominantly dispersion σ_R in edge-on systems. Because we expect $\sigma_z < \sigma_R$ (van der Kruit & Freeman 2011), we could be biased towards higher dispersions at higher inclinations (Leroy et al. 2008; Genzel et al. 2011). We have investigated this and see no trend of σ_0 with inclination i. This is probably due to the limited resolution of our data, as was reported in various studies at cosmic noon (Wisnioski et al. 2015; Übler et al. 2019). Mock observations of simulations can help test these various assumptions (Kohandel et al. 2020; Übler et al. 2021).

5.3.2 *Uncertainties in the stellar and dynamical masses*

In order to estimate the mass content of galaxies, we often need to rely on scaling relations linking photometry and kinematics to the underlying baryons and dark matter, and make assumptions on the galaxy's shape and size. We will now discuss the choices made in this work and how they affect our results. We infer stellar masses through SED modelling with PROSPECTOR, a method with many advantages but also many degeneracies. We attempt to break some of the degeneracies by fixing the redshift to the grism spectroscopic redshift, and by simultaneously fitting the photometry with the line fluxes of the available emission lines (see 3.1). Although we are not fitting spectra and only have access to some of the brighter emission lines, PROSPECTOR has been shown to successfully recover emission-line fluxes, when compared to NIRCam grism data, even when fitting with photometry only (Simmonds et al. 2025). Furthermore, our S/N cut implies selecting higher equivalent width galaxies, meaning galaxies whose young stellar population and nebular emission is dominating the SEDs (Boyett et al. 2024; Endsley et al. 2024). This can make it difficult to detect the underlying population of older stars, and hence to constrain the full SFH. This effect is called 'outshining' and can cause an underestimate of the stellar masses, effectively only attributing the stellar mass to the more visible young stellar population (Tacchella et al. 2022, 2023; Papovich et al. 2023; Whitler et al. 2023).

Moving to the dynamical masses, the circular velocities needed to compute them are inferred assuming a virialized rotating disc with an exponential light profile. For galaxies with larger Sérsic indices, this assumption can lead to biased results. Furthermore, for pressure-dominated systems, the choice of the pressure support term multiplying the σ_0 in equation (6) can lead to overestimations or underestimations of the circular velocity (see Price et al. 2022, for detailed analysis). Also, any uncertainties (and caveats) from the kinematic modelling (Section 5.3.1) are propagated to the dynamical masses through the circular velocity. Finally, due to the increased merger rates at high redshift, it is possible we are probing velocity offsets between two systems or velocity gradients induced by the gravitational interaction in a pre- or post-merger phase (see de Graaff et al. 2024a, for an in-depth discussion).

5.3.3 *The impact of dust on kinematics*

An important caveat in this work is that we do not directly measure dust attenuation. Although the early Universe was initially believed

---

[8] If both grism R and C are available (e.g. SAPPHIRES; Sun et al. 2025a, and see an example therein) or if observations are taken with varying PAs (e.g. ALT; Naidu et al. 2024), more spatial information can be obtained.

to be essentially dust free, recent works have revealed a rapid build-up of dust with detections out to $z \sim 7$ with both *JWST* and ALMA (Pallottini & Ferrara 2023; Witstok et al. 2023; Sawant et al. 2025), although these galaxies are typically more massive than the galaxies probed in this work. Furthermore, numerous works have indicated that a significant fraction of the star formation activity in the early Universe is actually occurring in dusty galaxies (Laporte et al. 2017; Sugahara et al. 2021; Inami et al. 2022), with Algera et al. (2023) finding a ~ 30 per cent contribution at $z \sim 7$ and ~ 66 per cent contribution at $z \sim 5$ (Sun et al. 2025b). Still, other works find results consistent with a low dust content at high redshift (Sandles et al. 2024).

In our sample, we infer dust attenuation using SED modelling with PROSPECTOR. Because of the inherent degeneracies in SED fitting, this could bias the SFRs we infer. Our fits show that the amount of dust attenuation increases with stellar mass, and that the relation between S/N and stellar mass has a large scatter, meaning that there are numerous massive galaxies, which also have higher dust content, with low S/N H α detections. This can however also be caused by low SFRs. An example of such a galaxy is the well-known *HST* dark galaxy HDF850.1 (Sun et al. 2024; Herard-Demanche et al. 2025), where the H α from the main component is heavily (>99 per cent) dust-obscured.. Because we are studying the kinematics of ionized gas through H α, we may be missing galaxies on the massive end due to their high dust content, and this could bias our correlations. However, studies at lower redshift suffer from the same biases, so our comparisons should be self-consistent.

6 SUMMARY AND CONCLUSIONS

In this work, we focus on a sample of 213 H α emitters in GOODS-S and GOODS-N at redshift $z \approx 3.9$–6.5 detected using *JWST* NIRCam slitless spectroscopy from the FRESCO and CONGRESS surveys. We select galaxies with high S/N (integrated S/N > 10) and a large enough PA offset from the dispersion direction ($|\mathrm{PA_{morph}}| < 75^{\circ}$) in order to study their ionized gas kinematics and the properties of their stellar populations. Our final sample probes two orders of magnitude in stellar mass ($M_\star \approx 10^{8-10}\,\mathrm{M}_\odot$) and SFR ($\mathrm{SFR}_{10} \approx 0.3$–$100\,\mathrm{M}_\odot\,\mathrm{yr}^{-1}$), and representative of the galaxy population down to $M_\star \approx 10^9\,\mathrm{M}_\odot$.

We use the SED-inference tool PROSPECTOR, with the redshift and H α emission-line fluxes obtained from the grism observations and photometry from JADES, to infer SFRs and stellar masses for our galaxies. We use a novel grism forward-modelling tool GEKO to infer the H α morphology and kinematics and measure rotational velocities, velocity dispersions, and dynamical masses. We use morphological priors from NIRCam imaging from the JADES survey to alleviate the morphology–kinematics degeneracy of the grism data. This method fully forward models the instrument, accounting for LSF, PSF, and pixelization.

We summarize our key results below:

(i) The star-forming galaxies in our sample at $z \approx 3.9$–6.5 are characterized by a highly turbulent ISM, with median ionized gas velocity dispersions of $\sigma_0 \approx 100\,\mathrm{km\,s^{-1}}$, but also a large scatter with velocity dispersions in the range $\sigma_0 = 30$–$200\,\mathrm{km\,s^{-1}}$. These systems also have an average rotational support $\mathbf{v}/\boldsymbol{\sigma_0} \approx \mathbf{1}$, with > 50 per cent of the galaxies being dispersion dominated ($v/\sigma_0 < 1$). Although we do not find significant evolution of σ_0 and v/σ_0 with redshift within our sample, when comparing to measurements at lower redshifts ($z < 4$), we find that the σ_0 (v/σ_0) increases (decreases) with redshift. This is broadly consistent with predictions from the Toomre model for marginal discs and from cosmological simulations.

(ii) We analyse the correlations between v/σ_0 and σ_0 with $M_\star$, SFR, sSFR, and SFR surface density, and find that the strongest correlation is between σ_0 and SFR ($\rho = 0.42$, $p < 0.001$). This is consistent with gravitational instabilities and feedback from star formation, which perturb the build-up of rotational support and inject energy into the ISM. Although it is difficult to distinguish between these two main sources of turbulence, we find no strong evidence for a dominant role of feedback-driven turbulence. The σ_0–SFR correlation is in agreement with results from the literature at $z < 4$, albeit with an offset towards higher σ_0.

(iii) We find a decreasing trend of v/σ_0 with $\log M_\star$, which is mainly driven by the underlying correlation with σ_0. However, a flattening of the v/σ_0–$\log M_\star$ relation below $M_\star \sim 10^{10}\,\mathrm{M}_\odot$ is not in tension with results from studies at $z < 4$ and is predicted by the marginal disc framework.

(iv) The fraction of rotationally supported ($v/\sigma_0 > 1$) systems in our sample does not vary from $z \sim 5.5$ to $z \sim 4.5$ for galaxies with stellar masses $9 < \log M_\star[\mathrm{M}_\odot] < 10$. The measured value of $f = (34 \pm 5)$ per cent indicates that discs do not dominate the star-forming galaxy population at these redshifts, and, when placed in the context of studies at lower redshifts, suggests that stable cold discs only form below $z < 1$, with a smooth increase of rotational support with cosmic time.

Overall, our work describes a turbulent phase in the evolution of galaxies in the early Universe. This epoch constitutes the dawn of discs, where galaxies start to be sustained by rotation but will go through several episodes of instability, caused by internal (feedback, radial inflows, bursty star formation) and external effects (non-smooth accretion, mergers), before settling into the cold discs we observe in the local Universe.

Our work has demonstrated that grism data are a powerful tool for population analyses of galaxy kinematics at high redshifts. Using this data set in harmony with a novel Bayesian inference forward-modelling tool, we were able to paint the first statistically significant picture of ionized gas kinematics at $z > 4$ on a large sample of galaxies. It however remains important to complement our work and future grism kinematics works with high-redshift multiwavelength interferometric and IFU observations from ALMA and NIRSpec IFU to study the complete 2D kinematics structure in more detail and place stronger constraints on the formation of stable discs in the early Universe.

ACKNOWLEDGEMENTS

We thank the referee, Scott Croom, for the helpful comments that greatly improved the paper. We thank Emily Wisnioski and Trevor Mendel for the insightful discussions. ALD thanks the University of Cambridge Harding Distinguished Postgraduate Scholars Programme and Technology Facilities Council (STFC) Center for Doctoral Training (CDT) in Data intensive science at the University of Cambridge (STFC grant number 2742605) for a PhD studentship. ALD and ST acknowledge support by the Royal Society Research Grant G125142. HÜ acknowledges funding by the European Union (ERC APEX, 101164796). Views and opinions expressed are however those of the authors only and do not necessarily reflect those of the European Union or the European Research Council Executive Agency. Neither the European Union nor the granting authority can be held responsible for them. EE, FS, ZJ, MR, and CNAW acknowledge support from the *JWST*/NIRCam contract to the University of Arizona NAS5-02015. SA acknowledges grant PID2021-127718NB-I00 funded by the Spanish Ministry of Science and Innovation/State Agency of Research (MICIN/AEI/10.13039/501100011033). AJB acknowledges funding from the 'FirstGalaxies' Advanced Grant from the European Research Council (ERC) under the European Union's Horizon 2020 research and innovation programme (Grant agreement No. 789056). SC acknowledges support by European Union's HE ERC Starting Grant No. 101040227 – WINGS. GCJ acknowledges support by the Science and Technology Facilities Council (STFC), ERC Advanced Grant 695671 'QUENCH'. RM, CS, and JS acknowledge support by the Science and Technology Facilities Council (STFC), and by the ERC through Advanced Grant 695671 'QUENCH'. RM and CS are also supported by the UKRI Frontier Research grant RISEandFALL. RM also acknowledges funding from a research professorship from the Royal Society. WM thanks the Science and Technology Facilities Council (STFC) Center for Doctoral Training (CDT) in Data Intensive Science at the University of Cambridge (STFC grant number 2742968) for a PhD studentship. NCV acknowledges support from the Charles and Julia Henry Fund through the Henry Fellowship. WMB gratefully acknowledges support from DARK via the DARK fellowship. This work was supported by a research grant (VIL54489) from Villum Fonden. DJE is supported as a Simons Investigator and by *JWST*/NIRCam contract to the University of Arizona, NAS5-02015. DP acknowledges support by the Huo Family Foundation through a P.C. Ho PhD Studentship. BER acknowledges support from the NIRCam Science Team contract to the University of Arizona, NAS5-02015, and *JWST* Program 3215. The research of CCW is supported by NOIRLab, which is managed by the Association of Universities for Research in Astronomy (AURA) under a cooperative agreement with the National Science Foundation.

This work is based on observations made with the NASA/ESA Hubble Space Telescope and NASA/ESA/CSA *James Webb Space Telescope*. The data were obtained from the Mikulski Archive for Space Telescopes at the Space Telescope Science Institute, which is operated by the Association of Universities for Research in Astronomy, Inc., under NASA contract NAS 5-03127 for *JWST*. These observations are associated with program #1180, 1181, 1210 (JADES), #1895 (FRESCO), # 1963 (JEMS), and #3577 (CONGRESS). Support for program #3577 was provided by NASA through a grant from the Space Telescope Science Institute, which is operated by the Association of Universities for Research in Astronomy, Inc., under NASA contract NAS 5-03127. The authors acknowledge the FRESCO team for developing their observing program with a zero-exclusive-access period. The authors acknowledge use of the lux supercomputer at UC Santa Cruz, funded by NSF MRI grant AST 1828315.

DATA AVAILABILITY

The data underlying this article will be shared on reasonable request to the corresponding author. Fully reduced NIRCam images are publicly available on MAST (https://archive.stsci.edu/hlsp/jades) (Rieke et al. 2023; Eisenstein et al. 2023). The NIRCam grism spectra are publicly available on MAST (Oesch et al. 2023).

REFERENCES

Algera H. S. B. et al., 2023, MNRAS, 518, 6142
Allen J. T. et al., 2015, MNRAS, 446, 1567
Allen N. et al., 2025, A&A, 698, A30
Arribas S., Colina L., Bellocchi E., Maiolino R., Villar-Martín M., 2014, A&A, 568, A14
Arribas S. et al., 2024, A&A, 688, A146
Bacchini C. et al., 2024, A&A, 687, A115
Bacon R. et al., 2010, in McLean I. S., Ramsay S. K., Takami H., eds, Proc. SPIE Conf. Ser. Vol. 7735, Ground-Based and Airborne Instrumentation for Astronomy III. SPIE, Bellingham, p. 773508
Baker W. M. et al., 2025a, Nat. Astron., 9, 141
Baker W. M. et al., 2025b, A&A, 697, A90
Barišić I. et al., 2025, ApJ, 983, 139
Barsanti S. et al., 2025, MNRAS, 538, 2660
Bassini L., Feldmann R., Gensior J., Hayward C. C., Faucher-Giguère C.-A., Cenci E., Liang L., Bernardini M., 2023, MNRAS, 525, 5388
Bezanson R. et al., 2018, ApJ, 858, 60
Boardman N., Wild V., Heckman T., Sanchez S. F., Riffel R., Riffel R. A., Zasowski G., 2023, MNRAS, 520, 4301
Bolatto A. D. et al., 2017, ApJ, 846, 159
Bouché N. F. et al., 2022, A&A, 658, A76
Bournaud F., Elmegreen B. G., Elmegreen D. M., 2007, ApJ, 670, 237
Boyett K. et al., 2024, MNRAS, 535, 1796
Brammer G. B., van Dokkum P. G., Coppi P., 2008, ApJ, 686, 1503
Brook C. B., Stinson G., Gibson B. K., Roškar R., Wadsley J., Quinn T., 2012, MNRAS, 419, 771
Bundy K. et al., 2015, ApJ, 798, 7
Bunker A. J., NIRSPEC Instrument Science Team, JADESs Collaboration, 2020, in da Cunha E., Hodge J., Afonso J., Pentericci L., Sobral D., eds, Proc. IAU Symp. 32, Uncovering Early Galaxy Evolution in the ALMA and JWST Era. Kluwer, Dordrecht, p. 342
Burkert A. et al., 2010, ApJ, 725, 2324
Byler N., Dalcanton J. J., Conroy C., Johnson B. D., 2017, ApJ, 840, 44
Calzetti D., Armus L., Bohlin R. C., Kinney A. L., Koornneef J., Storchi-Bergmann T., 2000, ApJ, 533, 682
Cappellari M., 2016, ARA&A, 54, 597
Cappellari M. et al., 2007, MNRAS, 379, 418
Cappellari M. et al., 2011, MNRAS, 416, 1680
Carniani S. et al., 2024, A&A, 685, A99
Cattaneo A. et al., 2009, Nature, 460, 213
Charlot S., Fall S. M., 2000, ApJ, 539, 718
Ciotti L., Bertin G., 1999, A&A, 352, 447
Conroy C., Gunn J. E., White M., 2009, ApJ, 699, 486
Courteau S., 1997, AJ, 114, 2402
Covelo-Paz A. et al., 2025, A&A, 694, A178
Croom S. M. et al., 2012, MNRAS, 421, 872
Croom S. M. et al., 2024, MNRAS, 529, 3446
D'Eugenio F. et al., 2024, Nat. Astron., 8, 1443
De Breuck C. et al., 2014, A&A, 565, A59
de Graaff A. et al., 2024a, A&A, 684, A87
de Graaff A., Pillepich A., Rix H.-W., 2024b, ApJ, 967, L40
Dekel A., Burkert A., 2014, MNRAS, 438, 1870
Dekel A. et al., 2009, Nature, 457, 451
Dekel A., Ginzburg O., Jiang F., Freundlich J., Lapiner S., Ceverino D., Primack J., 2020, MNRAS, 493, 4126
Della Bruna L. et al., 2020, A&A, 635, A134
Dib S., Bell E., Burkert A., 2006, ApJ, 638, 797
Dickinson M. et al., 2004, ApJ, 600, L99
Dillamore A. M., Belokurov V., Kravtsov A., Font A. S., 2024, MNRAS, 527, 7070
Duan Q. et al., 2024, preprint (arXiv:2411.04944)
Duan Q. et al., 2025, MNRAS, 540, 774
Dubois Y., Peirani S., Pichon C., Devriendt J., Gavazzi R., Welker C., Volonteri M., 2016, MNRAS, 463, 3948
Duncan K. et al., 2019, ApJ, 876, 110
Eisenstein D. J. et al., 2023, preprint (arXiv:2306.02465)
Ejdetjärn T., Agertz O., Östlin G., Rey M. P., Renaud F., 2024, MNRAS, 534, 135
El-Badry K., Wetzel A., Geha M., Hopkins P. F., Kereš D., Chan T. K., Faucher-Giguère C.-A., 2016, ApJ, 820, 131
El-Badry K. et al., 2018, MNRAS, 473, 1930

Emsellem E. et al., 2007, MNRAS, 379, 401
Endsley R. et al., 2024, MNRAS, 533, 1111
Epinat B., Amram P., Marcelin M., 2008, MNRAS, 390, 466
Epinat B., Amram P., Balkowski C., Marcelin M., 2010, MNRAS, 401, 2113
Fall S. M., Efstathiou G., 1980, MNRAS, 193, 189
Feng Y., Di Matteo T., Croft R., Tenneti A., Bird S., Battaglia N., Wilkins S., 2015, ApJ, 808, L17
Ferreira L. et al., 2022, ApJ, 938, L2
Ferreira L. et al., 2023, ApJ, 955, 94
Florian J., Ziegler B., Hirschmann M., Papaderos P., Choi E., Frigo M., Gomes J.-M., Somerville R. S., 2020, A&A, 635, A41
Forbes J. C. et al., 2023, ApJ, 948, 107
Förster Schreiber N. M., Wuyts S., 2020, ARA&A, 58, 661
Förster Schreiber N. M. et al., 2006, The Messenger, 125, 11
Förster Schreiber N. M. et al., 2009, ApJ, 706, 1364
Förster Schreiber N. M. et al., 2018, ApJS, 238, 21
Foster C. et al., 2025, Publ. Astron. Soc. Aust., 42, e035
Freeman K. C., 1970, ApJ, 160, 811
Gabor J. M., Bournaud F., 2014, MNRAS, 437, L56
Gatto A. et al., 2015, MNRAS, 449, 1057
Genzel R. et al., 2008, ApJ, 687, 59
Genzel R. et al., 2011, ApJ, 733, 101
Genzel R. et al., 2017, Nature, 543, 397
Genzel R. et al., 2020, ApJ, 902, 98
Giavalisco M. et al., 2004, ApJ, 600, L93
Girard M., Dessauges-Zavadsky M., Combes F., Chisholm J., Patrício V., Richard J., Schaerer D., 2019, A&A, 631, A91
Glazebrook K., 2013, Publ. Astron. Soc. Aust., 30, e056
Graham A. W., Driver S. P., 2005, Publ. Astron. Soc. Aust., 22, 118
Green A. W. et al., 2014, MNRAS, 437, 1070
Green A. W. et al., 2018, MNRAS, 475, 716
Greene T. P. et al., 2017, J. Astron. Tel. Instrum. Syst., 3, 035001
Hainline K. N. et al., 2024, ApJ, 964, 71
Harrison C. M., 2017, Nat. Astron., 1, 0165
Harvey T. et al., 2025, ApJ, 978, 89
Hasheminia M., Mosleh M., Hosseini-ShahiSavandi S. Z., Tacchella S., 2024, ApJ, 975, 252
Helton J. M. et al., 2024a, ApJ, 962, 124
Helton J. M. et al., 2024b, ApJ, 974, 41
Herard-Demanche T. et al., 2025, MNRAS, 537, 788
Hodge J. A., Carilli C. L., Walter F., de Blok W. J. G., Riechers D., Daddi E., Lentati L., 2012, ApJ, 760, 11
Hoffman M. D., Gelman A., 2011, preprint (arXiv:1111.4246)
Hopkins P. F., Quataert E., Murray N., 2011, MNRAS, 417, 950
Hopkins P. F. et al., 2023, MNRAS, 525, 2241
Hubble E. P., 1926, ApJ, 64, 321
Huško F., Lacey C. G., Baugh C. M., 2022, MNRAS, 509, 5918
Inami H. et al., 2022, MNRAS, 515, 3126
Inoue A. K., 2011, Earth Planets Space, 63, 1027
Jain S., Tacchella S., Mosleh M., 2024, Open J. Astrophys., 7, 113
Ji Z., Giavalisco M., 2023, ApJ, 943, 54
Ji Z., Giavalisco M., 2024, preprint (arXiv:2410.00099)
Ji Z. et al., 2024, preprint (arXiv:2401.00934)
Johnson H. L. et al., 2018, MNRAS, 474, 5076
Johnson B. D., Leja J., Conroy C., Speagle J. S., 2021, ApJS, 254, 22
Jones O. C. et al., 2023, MNRAS, 523, 2519
Jones G. C. et al., 2024, A&A, 682, A122
Ju M. et al., 2025, ApJ, 978, L39
Kannan R. et al., 2025, preprint (arXiv:2502.20437)
Kashino D., Lilly S. J., Matthee J., Eilers A.-C., Mackenzie R., Bordoloi R., Simcoe R. A., 2023, ApJ, 950, 66
Klessen R. S., Hennebelle P., 2010, A&A, 520, A17
Kohandel M., Pallottini A., Ferrara A., Carniani S., Gallerani S., Vallini L., Zanella A., Behrens C., 2020, MNRAS, 499, 1250
Kohandel M., Pallottini A., Ferrara A., Zanella A., Rizzo F., Carniani S., 2024, A&A, 685, A72
Kormendy J., Ho L. C., 2013, ARA&A, 51, 511
Kormendy J., Kennicutt R. C., Jr, 2004, ARA&A, 42, 603
Krajnović D. et al., 2011, MNRAS, 414, 2923
Kretschmer M., Agertz O., Teyssier R., 2020, MNRAS, 497, 4346
Kretschmer M., Dekel A., Teyssier R., 2022, MNRAS, 510, 3266
Kriek M., Conroy C., 2013, ApJ, 775, L16
Krumholz M. R., Burkhart B., 2016, MNRAS, 458, 1671
Krumholz M. R., Burkhart B., Forbes J. C., Crocker R. M., 2018, MNRAS, 477, 2716
Lapiner S. et al., 2023, MNRAS, 522, 4515
Laporte N. et al., 2017, ApJ, 837, L21
Law D. R. et al., 2022, ApJ, 928, 58
Le Bail A. et al., 2024, A&A, 688, A53
Leja J., Carnall A. C., Johnson B. D., Conroy C., Speagle J. S., 2019, ApJ, 876, 3
Lelli F., Di Teodoro E. M., Fraternali F., Man A. W. S., Zhang Z.-Y., De Breuck C., Davis T. A., Maiolino R., 2021, Science, 371, 713
Lelli F. et al., 2023, A&A, 672, A106
Leroy A. K., Walter F., Brinks E., Bigiel F., de Blok W. J. G., Madore B., Thornley M. D., 2008, AJ, 136, 2782
Leroy A. K. et al., 2009, AJ, 137, 4670
Li Z. et al., 2023, preprint (arXiv:2310.09327)
Li J. et al., 2024, ApJ, 976, 70
Lilly S. J., Carollo C. M., Pipino A., Renzini A., Peng Y., 2013, ApJ, 772, 119
Looser T. J. et al., 2024, Nature, 629, 53
Madau P., Dickinson M., 2014, ARA&A, 52, 415
Mai Y. et al., 2024, MNRAS, 533, 3878
Mandelker N., Dekel A., Ceverino D., DeGraf C., Guo Y., Primack J., 2017, MNRAS, 464, 635
Mannucci F., Cresci G., Maiolino R., Marconi A., Gnerucci A., 2010, MNRAS, 408, 2115
Marconcini C. et al., 2024, MNRAS, 533, 2488
Marshall M. A., Wilkins S., Di Matteo T., Roper W. J., Vijayan A. P., Ni Y., Feng Y., Croft R. A. C., 2022, MNRAS, 511, 5475
Matharu J. et al., 2023, ApJ, 949, L11
Matthee J. et al., 2024, ApJ, 963, 129
McClymont W. et al., 2025a, preprint (arXiv:2503.00106)
McClymont W. et al., 2025b, preprint (arXiv:2503.04894)
Miller S. H., Bundy K., Sullivan M., Ellis R. S., Treu T., 2011, ApJ, 741, 115
Mo H. J., Mao S., White S. D. M., 1998, MNRAS, 295, 319
Mosleh M., Hosseinnejad S., Hosseini-ShahiSavandi S. Z., Tacchella S., 2020, ApJ, 905, 170
Muñoz-Mateos J. C., Gil de Paz A., Boissier S., Zamorano J., Jarrett T., Gallego J., Madore B. F., 2007, ApJ, 658, 1006
Naab T. et al., 2014, MNRAS, 444, 3357
Naidu R. P. et al., 2024, preprint (arXiv:2410.01874)
Nakazato Y., Ceverino D., Yoshida N., 2024, ApJ, 975, 238
Neeleman M., Prochaska J. X., Kanekar N., Rafelski M., 2020, Nature, 581, 269
Nelson E. J. et al., 2016, ApJ, 828, 27
Nelson D. et al., 2019, MNRAS, 490, 3234
Nelson E. J. et al., 2023, ApJ, 948, L18
Nelson E. et al., 2024, ApJ, 976, L27
Nestor Shachar A. et al., 2023, ApJ, 944, 78
Newman S. F. et al., 2012, ApJ, 761, 43
Newman S. F. et al., 2013, ApJ, 767, 104
Newman A. B., Belli S., Ellis R. S., 2015, ApJ, 813, L7
Newman A. B., Belli S., Ellis R. S., Patel S. G., 2018, ApJ, 862, 126
Oesch P. A. et al., 2023, MNRAS, 525, 2864
Oh S. et al., 2024, MNRAS, 531, 4017
Oklopčić A., Hopkins P. F., Feldmann R., Kereš D., Faucher-Giguère C.-A., Murray N., 2017, MNRAS, 465, 952
Oppenheimer B. D., Davé R., 2008, MNRAS, 387, 577
Oppenheimer B. D., Davé R., Kereš D., Fardal M., Katz N., Kollmeier J. A., Weinberg D. H., 2010, MNRAS, 406, 2325
Ostriker E. C., Shetty R., 2011, ApJ, 731, 41
Pallottini A., Ferrara A., 2023, A&A, 677, L4
Pandya V. et al., 2024, ApJ, 963, 54

Papovich C. et al., 2023, ApJ, 949, L18
Parlanti E., Carniani S., Pallottini A., Cignoni M., Cresci G., Kohandel M., Mannucci F., Marconi A., 2023, A&A, 673, A153
Parlanti E. et al., 2024, A&A, 684, A24
Pasha I., Miller T. B., 2023, J. Open Source Softw., 8, 5703
Pelliccia D. et al., 2020, ApJ, 896, L26
Phan D., Pradhan N., Jankowiak M., 2019, preprint (arXiv:1912.11554)
Pillepich A. et al., 2019, MNRAS, 490, 3196
Planck Collaboration VI, 2020, A&A, 641, A6
Pope A. et al., 2023, ApJ, 951, L46
Price S. H. et al., 2016, ApJ, 819, 80
Price S. H. et al., 2020, ApJ, 894, 91
Price S. H. et al., 2022, A&A, 665, A159
Puskás D. et al., 2025, MNRAS, 540, 2146
Qu Y., Di Matteo P., Lehnert M., van Driel W., Jog C. J., 2010, A&A, 515, A11
Rathjen T.-E., Naab T., Walch S., Seifried D., Girichidis P., Wünsch R., 2023, MNRAS, 522, 1843
Reines A. E., Volonteri M., 2015, ApJ, 813, 82
Rieke M., 2020, in da Cunha E., Hodge J., Afonso J., Pentericci L., Sobral D., eds, Proc. IAU Symp. 352, Uncovering Early Galaxy Evolution in the ALMA and JWST Era. Kluwer, Dordrecht, p. 337
Rieke M. J. et al., 2023, ApJS, 269, 16
Rigamonti F., Cortese L., Bollati F., Covino S., Dotti M., Fraser-McKelvie A., Haardt F., 2024, A&A, 686, A98
Rizzo F., Vegetti S., Powell D., Fraternali F., McKean J. P., Stacey H. R., White S. D. M., 2020, Nature, 584, 201
Rizzo F. et al., 2023, A&A, 679, A129
Rizzo F. et al., 2024, A&A, 689, A273
Robertson B. E. et al., 2023, ApJ, 942, L42
Robertson B. et al., 2024, ApJ, 970, 31
Romeo A. B., Agertz O., 2014, MNRAS, 442, 1230
Romeo A. B., Burkert A., Agertz O., 2010, MNRAS, 407, 1223
Rowland L. E. et al., 2024, MNRAS, 535, 2068
Saldana-Lopez A. et al., 2025, preprint (arXiv:2501.17145)
Sales L. V., Navarro J. F., Theuns T., Schaye J., White S. D. M., Frenk C. S., Crain R. A., Dalla Vecchia C., 2012, MNRAS, 423, 1544
Sandles L. et al., 2024, A&A, 691, A305
Sawant P. et al., 2025, A&A, 694, A82
Schneider R., Maiolino R., 2024, A&AR, 32, 2
Scholtz J. et al., 2024, A&A, 687, A283
Semenov V. A., Conroy C., Smith A., Puchwein E., Hernquist L., 2025a, ApJ, 990, 18
Semenov V. A., Conroy C., Hernquist L., 2025b, ApJ, 989, 14
Semenov V. A., Conroy C., Chandra V., Hernquist L., Nelson D., 2024c, ApJ, 972, 73
Sersic J. L., 1968, Atlas de Galaxias Australes. Observatorio Astronomico, Cordoba, Argentina
Sharda P., Krumholz M. R., Wisnioski E., Forbes J. C., Federrath C., Acharyya A., 2021, MNRAS, 502, 5935
Sharma G., Upadhyaya V., Salucci P., Desai S., 2024, A&A, 689, A318
Shetty R., Ostriker E. C., 2012, ApJ, 754, 2
Shuntov M. et al., 2025, A&A, 695, A20
Silk J., Rees M. J., 1998, A&A, 331, L1
Simard L., Mendel J. T., Patton D. R., Ellison S. L., McConnachie A. W., 2011, ApJS, 196, 11
Simmonds C. et al., 2024, MNRAS, 535, 2998
Simmonds C. et al., 2025, preprint (arXiv:2508.04410)
Simons R. C. et al., 2016, ApJ, 830, 14
Simons R. C. et al., 2017, ApJ, 843, 46
Simons R. C. et al., 2019, ApJ, 874, 59
Simons R. C. et al., 2021, ApJ, 923, 203
Stott J. P. et al., 2016, MNRAS, 457, 1888
Sugahara Y. et al., 2021, ApJ, 923, 5
Sun F. et al., 2022, ApJ, 936, L8
Sun F. et al., 2023a, ApJ, 953, 53
Sun G., Faucher-Giguère C.-A., Hayward C. C., Shen X., Wetzel A., Cochrane R. K., 2023b, ApJ, 955, L35
Sun F. et al., 2024, ApJ, 961, 69
Sun F. et al., 2025a, preprint (arXiv:2503.15587)
Sun F. et al., 2025b, ApJ, 980, 12
Swinbank A. M. et al., 2011, ApJ, 742, 11
Swinbank A. M. et al., 2017, MNRAS, 467, 3140
Tacchella S. et al., 2015, Science, 348, 314
Tacchella S., Dekel A., Carollo C. M., Ceverino D., DeGraf C., Lapiner S., Mandelker N., Primack Joel R., 2016a, MNRAS, 457, 2790
Tacchella S., Dekel A., Carollo C. M., Ceverino D., DeGraf C., Lapiner S., Mandelker N., Primack J. R., 2016b, MNRAS, 458, 242
Tacchella S. et al., 2019, MNRAS, 487, 5416
Tacchella S., Forbes J. C., Caplar N., 2020, MNRAS, 497, 698
Tacchella S. et al., 2022, ApJ, 927, 170
Tacchella S. et al., 2023, MNRAS, 522, 6236
Tacconi L. J. et al., 2013, ApJ, 768, 74
Tacconi L. J. et al., 2018, ApJ, 853, 179
Tacconi L. J., Genzel R., Sternberg A., 2020, ARA&A, 58, 157
Tan V. Y. Y. et al., 2024, preprint (arXiv:2412.07829)
Tiley A. L. et al., 2016, MNRAS, 460, 103
Tohill C., Bamford S. P., Conselice C. J., Ferreira L., Harvey T., Adams N., Austin D., 2024, ApJ, 962, 164
Toomre A., 1964, ApJ, 139, 1217
Tsukui T., Iguchi S., 2021, Science, 372, 1201
Tsukui T., Wisnioski E., Bland-Hawthorn J., Mai Y., Iguchi S., Baba J., Freeman K., 2024, MNRAS, 527, 8941
Tsukui T., Wisnioski E., Bland-Hawthorn J., Freeman K., 2025, MNRAS, 540, 3493
Turner O. J., Harrison C. M., Cirasuolo M., McLure R. J., Dunlop J., Swinbank A. M., Tiley A. L., 2017a, preprint (arXiv:1711.03604)
Turner O. J. et al., 2017b, MNRAS, 471, 1280
Übler H., Naab T., Oser L., Aumer M., Sales L. V., White S. D. M., 2014, MNRAS, 443, 2092
Übler H. et al., 2017, ApJ, 842, 121
Übler H. et al., 2019, ApJ, 880, 48
Übler H. et al., 2021, MNRAS, 500, 4597
Übler H. et al., 2024, MNRAS, 533, 4287
van de Sande J. et al., 2018, Nat. Astron., 2, 483
van den Bosch F. C., 2001, MNRAS, 327, 1334
van der Kruit P. C., Freeman K. C., 2011, ARA&A, 49, 301
van der Wel A. et al., 2014, ApJ, 792, L6
van Donkelaar F., Agertz O., Renaud F., 2022, MNRAS, 512, 3806
Varidel M. R. et al., 2020, MNRAS, 495, 2265
Venturi G. et al., 2024, A&A, 691, A19
Walter F., Brinks E., de Blok W. J. G., Bigiel F., Kennicutt R. C., Jr, Thornley M. D., Leroy A., 2008, AJ, 136, 2563
Wang B., Cappellari M., Peng Y., Graham M., 2020, MNRAS, 495, 1958
Weibel A. et al., 2024, MNRAS, 533, 1808
Whitler L., Stark D. P., Endsley R., Leja J., Charlot S., Chevallard J., 2023, MNRAS, 519, 5859
Williams C. C. et al., 2023, ApJS, 268, 64
Wisnioski E. et al., 2011, MNRAS, 417, 2601
Wisnioski E. et al., 2015, ApJ, 799, 209
Wisnioski E. et al., 2019, ApJ, 886, 124
Witstok J. et al., 2023, Nature, 621, 267
Witten C. et al., 2025, MNRAS, 537, 112
Wright S. A., Larkin J. E., Law D. R., Steidel C. C., Shapley A. E., Erb D. K., 2009, ApJ, 699, 421
Wuyts S. et al., 2011, ApJ, 742, 96
Wuyts E. et al., 2016a, ApJ, 827, 74
Wuyts S. et al., 2016b, ApJ, 831, 149
Yu X. et al., 2019, MNRAS, 486, 4463
Zhang Y., Ouchi M., Nakajima K., Harikane Y., Isobe Y., Xu Y., Ono Y., Umeda H., 2024, ApJ, 970, 19
Zhu L. et al., 2018, Nat. Astron., 2, 233
Zhu Y. et al., 2025, ApJ, 986, 18
Zolotov A. et al., 2015, MNRAS, 450, 2327

APPENDIX A: SAMPLE STATISTICS

In this section, we present some summary tables for the key measurements of this work, as well as provide further insight into the physical distribution of our various sub-samples.

In Tables A1 and A2, we summarize the median values, for our extended and gold samples, of σ_0 and v/σ_0 in bins of redshift (Figs 6, 7, and 8), and stellar mass, SFR, sSFR, and SFR surface density (Figs 9 and 10). For each bin, we specify the range probed by the bin, the median value of the binned quantity, the number of galaxies N contained in the bin, and the average stellar mass $< \log(M_\star[\mathrm{M}_\odot]) >$. For completeness, we also include the average value of the rotational support when computed using the maximum observed velocity $\upsilon_{\mathrm{obs,max}}$ instead of the velocity at the effective radius υ_{re}. We find consistent values, within the uncertainties, for the two measures of rotational support. However we note that $\upsilon_{\mathrm{obs,max}}/\sigma_0$ is on average higher than $\upsilon_{\mathrm{re}}/\sigma_0$.

In Table A3, we summarize the physical properties of the galaxies in the gold sample, along with their best-fitting kinematic measurements.

In order to study possible biases in the sizes probed by galaxies in our sub-samples, we plot the distribution of the best-fitting Hα effective radius r_e in arcseconds, for the gold and samples, on Fig. A1. We find that the two sample follow similar distributions, with the silver sample probing some larger systems at the tail end of the distribution. The cuts made to obtain the gold sample to not bias it in size compared to the silver one.

We further investigate the stellar mass distribution of galaxies in the gold, silver, and extended samples on Fig. A2. The gold and extended samples, which we use to compute our medians and correlations, have similar distributions, with the resolved sample having a slightly longer tail on the low-mass end.

Table A1. Summary table of the medians for the extended galaxies in the gold and silver sample, for bins of redshift (Figs 6, 7, and 8), and stellar mass, SFR, sSFR, and SFR surface density (Figs 9 and 10). For each bin, we specify the range probed by the bin, the median value of the binned quantity, the number of galaxies N contained in the bin, and the average stellar mass $< \log(M_\star[\mathrm{M}_\odot]) >$. We also include the average value of the rotational support when computed using the maximum observed velocity $\upsilon_{\mathrm{obs,max}}$ instead of the velocity at the effective radius υ_{re}.

Bin	Mean value	N	$< \log(M_\star[\mathrm{M}_\odot]) >$	$< \upsilon_{\mathrm{re}}/\sigma_0 >$	$< \upsilon_{\mathrm{obs,max}}/\sigma_0 >$	$< \sigma_0$ [km s^{-1}] $>$
$3.8 < z < 4.2$	4.06	28	9.40	$1.0^{+0.1}_{-0.2}$	$1.5^{+0.2}_{-0.2}$	87^{+12}_{-9}
$4.2 < z < 5.0$	4.61	22	9.01	$1.3^{+0.3}_{-0.3}$	$1.5^{+0.8}_{-0.6}$	59^{+8}_{-7}
$5.0 < z < 6.1$	5.39	31	9.10	$0.6^{+0.1}_{-0.1}$	$0.7^{+0.2}_{-0.1}$	89^{+10}_{-9}
$7.5 < \log(M_\star\ [\mathrm{M}_\odot]) < 9.0$	8.38	26	8.34	$1.4^{+0.3}_{-0.2}$	$2.4^{+0.4}_{-0.3}$	54^{+6}_{-5}
$9.0 < \log(M_\star\ [\mathrm{M}_\odot]) < 9.5$	9.28	21	9.26	$1.0^{+0.3}_{-0.2}$	$1.7^{+0.2}_{-0.3}$	84^{+8}_{-8}
$9.5 < \log(M_\star\ [\mathrm{M}_\odot]) < 10.5$	9.70	33	9.83	$0.6^{+0.1}_{-0.1}$	$1.2^{+0.2}_{-0.2}$	103^{+11}_{-10}
$0 < \log(\mathrm{SFR}_{10}\ [\mathrm{M}_\odot\ \mathrm{yr}^{-1}]) < 0.8$	0.53	33	8.61	$1.3^{+0.2}_{-0.2}$	$2.5^{+0.4}_{-0.4}$	63^{+6}_{-6}
$0.8 < \log(\mathrm{SFR}_{10}\ [\mathrm{M}_\odot\ \mathrm{yr}^{-1}]) < 1.3$	1.02	36	9.46	$0.8^{+0.2}_{-0.1}$	$1.3^{+0.2}_{-0.2}$	89^{+8}_{-8}
$1.3 < \log(\mathrm{SFR}_{10}\ [\mathrm{M}_\odot\ \mathrm{yr}^{-1}]) < 2.5$	1.65	11	10.09	$0.6^{+0.1}_{-0.1}$	$1.1^{+0.2}_{-0.2}$	151^{+25}_{-50}
$0 < \log(\mathrm{sSFR}_{10}\ [\mathrm{M}_\odot\ \mathrm{yr}^{-1}]) < 0.5$	0.28	26	9.62	$0.7^{+0.1}_{-0.1}$	$1.3^{+0.4}_{-0.3}$	81^{+5}_{-6}
$0.5 < \log(\mathrm{sSFR}_{10}\ [\mathrm{M}_\odot\ \mathrm{yr}^{-1}]) < 1.0$	0.69	33	9.28	$0.9^{+0.1}_{-0.2}$	$1.7^{+0.2}_{-0.2}$	90^{+12}_{-13}
$1.0 < \log(\mathrm{sSFR}_{10}\ [\mathrm{M}_\odot\ \mathrm{yr}^{-1}]) < 2.0$	1.28	19	8.23	$1.3^{+0.3}_{-0.3}$	$1.9^{+0.4}_{-0.3}$	61^{+11}_{-7}
$-1.0 < \log(\Sigma_{\mathrm{SFR}_{10}}\ [\mathrm{M}_\odot\ \mathrm{yr}^{-1}\ \mathrm{kpc}^{-2}]) < -0.2$	−0.44	27	8.60	$1.3^{+0.3}_{-0.2}$	$2.4^{+0.4}_{-0.3}$	61^{+6}_{-5}
$-0.2 < \log(\Sigma_{\mathrm{SFR}_{10}}\ [\mathrm{M}_\odot\ \mathrm{yr}^{-1}\ \mathrm{kpc}^{-2}]) < 0.2$	0.04	26	9.39	$0.8^{+0.3}_{-0.1}$	$1.5^{+0.3}_{-0.3}$	95^{+12}_{-17}
$0.2 < \log(\Sigma_{\mathrm{SFR}_{10}}\ [\mathrm{M}_\odot\ \mathrm{yr}^{-1}\ \mathrm{kpc}^{-2}]) < 1.0$	0.31	25	9.68	$0.7^{+0.1}_{-0.1}$	$1.1^{+0.2}_{-0.1}$	95^{+11}_{-8}

Table A2. Summary table of the medians for the gold sample, following the same format as Table A1.

Bin	Mean value	N	$< \log(M_\star[\mathrm{M}_\odot]) >$	$< v_{\mathrm{re}}/\sigma_0 >$	$< v_{\mathrm{obs,max}}/\sigma_0 >$	$< \sigma_0\ (\mathrm{km\,s^{-1}}) >$
$3.8 < z < 4.2$	4.06	16	9.55	$1.0^{+0.1}_{-0.3}$	$1.5^{+0.2}_{-0.2}$	103^{+15}_{-14}
$4.2 < z < 5.0$	4.55	8	9.51	$1.0^{+0.6}_{-0.3}$	$1.5^{+0.8}_{-0.6}$	84^{+8}_{-16}
$5.0 < z < 6.1$	5.29	13	9.45	$0.5^{+0.1}_{-0.1}$	$0.7^{+0.2}_{-0.1}$	102^{+12}_{-20}
$7.5 < \log(M_\star\ [\mathrm{M}_\odot]) < 9.0$	8.56	6	8.48	$1.8^{+0.9}_{-0.3}$	$2.7^{+0.5}_{-0.5}$	51^{+8}_{-7}
$9.0 < \log(M_\star\ [\mathrm{M}_\odot]) < 9.5$	9.39	9	9.32	$1.0^{+0.5}_{-0.3}$	$1.5^{+0.2}_{-0.3}$	86^{+11}_{-8}
$9.5 < \log(M_\star\ [\mathrm{M}_\odot]) < 10.5$	9.72	22	9.87	$0.5^{+0.1}_{-0.1}$	$1.1^{+0.2}_{-0.2}$	119^{+16}_{-12}
$0 < \log(\mathrm{SFR}_{10}\ [\mathrm{M}_\odot\ \mathrm{yr}^{-1}]) < 0.8$	0.75	7	8.77	$1.5^{+0.3}_{-0.3}$	$2.4^{+0.5}_{-0.5}$	65^{+10}_{-10}
$0.8 < \log(\mathrm{SFR}_{10}\ [\mathrm{M}_\odot\ \mathrm{yr}^{-1}]) < 1.3$	1.03	16	9.42	$0.8^{+0.3}_{-0.2}$	$1.5^{+0.2}_{-0.3}$	90^{+8}_{-7}
$1.3 < \log(\mathrm{SFR}_{10}\ [\mathrm{M}_\odot\ \mathrm{yr}^{-1}]) < 2.5$	1.52	14	9.98	$0.5^{+0.1}_{-0.1}$	$0.9^{+0.2}_{-0.2}$	157^{+14}_{-20}
$0 < \log(\mathrm{sSFR}_{10}\ [\mathrm{M}_\odot\ \mathrm{yr}^{-1}]) < 0.5$	0.25	11	9.77	$0.6^{+0.1}_{-0.1}$	$1.1^{+0.5}_{-0.2}$	85^{+4}_{-6}
$0.5 < \log(\mathrm{sSFR}_{10}\ [\mathrm{M}_\odot\ \mathrm{yr}^{-1}]) < 1.0$	0.68	18	9.53	$0.8^{+0.2}_{-0.2}$	$1.4^{+0.2}_{-0.2}$	118^{+15}_{-13}
$1.0 < \log(\mathrm{sSFR}_{10}\ [\mathrm{M}_\odot\ \mathrm{yr}^{-1}]) < 2.0$	1.38	6	8.62	$1.4^{+0.3}_{-0.3}$	$2.1^{+0.8}_{-0.6}$	56^{+14}_{-9}
$-1.0 < \log(\Sigma_{\mathrm{SFR}_{10}}\ [\mathrm{M}_\odot\ \mathrm{yr}^{-1}\ \mathrm{kpc}^{-2}]) < -0.2$	−0.45	5	8.91	$1.6^{+0.8}_{-0.5}$	$2.2^{+0.6}_{-0.4}$	68^{+9}_{-10}
$-0.2 < \log(\Sigma_{\mathrm{SFR}_{10}}\ [\mathrm{M}_\odot\ \mathrm{yr}^{-1}\ \mathrm{kpc}^{-2}]) < 0.2$	0.07	14	9.49	$0.8^{+0.3}_{-0.2}$	$1.5^{+0.2}_{-0.4}$	106^{+26}_{-16}
$0.2 < \log(\Sigma_{\mathrm{SFR}_{10}}\ [\mathrm{M}_\odot\ \mathrm{yr}^{-1}\ \mathrm{kpc}^{-2}]) < 1.0$	0.33	18	9.68	$0.6^{+0.1}_{-0.1}$	$1.0^{+0.2}_{-0.2}$	103^{+14}_{-12}

Table A3. Kinematic measurements and star formation properties for the galaxies in the gold sample.

JADES ID	z	$\log(M_\star[\mathrm{M}_\odot])$	$\log(\mathrm{SFR}\ [\mathrm{M}_\odot\ \mathrm{yr}^{-1}])$	r_{e} (kpc)	v/σ_0	$\sigma_0\ (\mathrm{km\,s^{-1}})$	$\log(M_{\mathrm{dyn}}[\mathrm{M}_\odot])$
192600	5.39	$7.99^{+0.16}_{-0.11}$	$0.86^{+0.04}_{-0.15}$	$0.96^{+0.31}_{-0.20}$	$1.9^{+2.2}_{-0.8}$	< 60	$9.74^{+0.31}_{-0.32}$
1011050	5.19	$9.12^{+0.20}_{-0.16}$	$1.14^{+0.10}_{-0.18}$	$1.06^{+0.07}_{-0.06}$	$1.5^{+3.7}_{-0.8}$	< 48	$9.29^{+0.32}_{-0.33}$
1017070	5.18	$9.18^{+0.28}_{-0.24}$	$1.12^{+0.14}_{-0.16}$	$1.02^{+0.25}_{-0.21}$	$0.3^{+0.4}_{-0.2}$	69^{+11}_{-10}	$9.83^{+0.15}_{-0.16}$
81170	5.39	$9.50^{+0.25}_{-0.25}$	$1.65^{+0.23}_{-0.27}$	$1.36^{+0.10}_{-0.09}$	$0.1^{+0.1}_{-0.1}$	216^{+19}_{-17}	$10.93^{+0.07}_{-0.07}$
1028887	5.19	$9.56^{+0.19}_{-0.19}$	$1.15^{+0.22}_{-0.17}$	$0.98^{+0.06}_{-0.06}$	$0.2^{+0.1}_{-0.1}$	101^{+7}_{-7}	$10.13^{+0.06}_{-0.06}$
1006269	5.44	$9.55^{+0.17}_{-0.18}$	$1.24^{+0.14}_{-0.12}$	$1.01^{+0.08}_{-0.07}$	$0.3^{+0.2}_{-0.1}$	117^{+10}_{-11}	$10.29^{+0.07}_{-0.09}$
1002030	5.18	$9.48^{+0.18}_{-0.24}$	$0.93^{+0.17}_{-0.11}$	$1.21^{+0.15}_{-0.11}$	$0.7^{+0.2}_{-0.2}$	111^{+16}_{-16}	$10.35^{+0.10}_{-0.12}$
191250	5.39	$10.17^{+0.30}_{-0.09}$	$1.69^{+0.24}_{-0.17}$	$2.43^{+0.05}_{-0.05}$	$10.8^{+25.4}_{-5.3}$	< 42	$10.73^{+0.05}_{-0.05}$
1002222	5.29	$9.47^{+0.18}_{-0.44}$	$0.93^{+0.32}_{-0.38}$	$0.90^{+0.14}_{-0.10}$	$0.6^{+0.3}_{-0.3}$	78^{+9}_{-9}	$9.91^{+0.10}_{-0.12}$
214966	5.54	$9.54^{+0.16}_{-0.21}$	$1.21^{+0.19}_{-0.17}$	$1.25^{+0.05}_{-0.05}$	$0.6^{+0.3}_{-0.2}$	127^{+23}_{-31}	$10.47^{+0.12}_{-0.19}$
1025527	5.29	$9.39^{+0.16}_{-0.56}$	$1.02^{+0.13}_{-0.13}$	$0.95^{+0.10}_{-0.09}$	$0.8^{+0.3}_{-0.2}$	111^{+19}_{-19}	$10.28^{+0.12}_{-0.15}$
1001674	5.18	$9.92^{+0.17}_{-0.13}$	$1.60^{+0.20}_{-0.30}$	$1.71^{+0.21}_{-0.16}$	$0.6^{+0.2}_{-0.2}$	197^{+19}_{-20}	$11.00^{+0.10}_{-0.09}$
201125	5.82	$9.96^{+0.10}_{-0.16}$	$1.71^{+0.13}_{-0.18}$	$1.44^{+0.09}_{-0.09}$	$0.6^{+0.2}_{-0.2}$	139^{+13}_{-14}	$10.62^{+0.07}_{-0.07}$
1084873	4.69	$9.33^{+0.21}_{-0.29}$	$1.02^{+0.30}_{-0.27}$	$0.96^{+0.11}_{-0.08}$	$1.8^{+1.1}_{-0.7}$	86^{+23}_{-35}	$10.24^{+0.33}_{-0.42}$
1094616	4.06	$9.40^{+0.16}_{-0.36}$	$1.04^{+0.32}_{-0.17}$	$1.35^{+0.08}_{-0.09}$	$1.9^{+1.9}_{-0.5}$	178^{+11}_{-21}	$11.10^{+0.29}_{-0.12}$
1088814	4.41	$10.60^{+0.13}_{-0.36}$	$1.59^{+0.49}_{-0.35}$	$2.21^{+0.06}_{-0.05}$	$0.8^{+0.1}_{-0.1}$	166^{+18}_{-20}	$10.98^{+0.07}_{-0.10}$
1080133	4.42	$9.62^{+0.15}_{-0.15}$	$1.21^{+0.10}_{-0.10}$	$1.64^{+0.14}_{-0.11}$	$0.2^{+0.2}_{-0.1}$	206^{+27}_{-39}	$10.97^{+0.13}_{-0.17}$
1085659	4.06	$10.17^{+0.13}_{-0.42}$	$1.27^{+0.41}_{-0.20}$	$1.33^{+0.12}_{-0.09}$	$0.6^{+0.2}_{-0.2}$	84^{+10}_{-12}	$10.14^{+0.09}_{-0.11}$
1083165	4.15	$9.78^{+0.09}_{-0.13}$	$0.96^{+0.22}_{-0.16}$	$1.13^{+0.07}_{-0.06}$	$0.6^{+0.2}_{-0.1}$	112^{+10}_{-12}	$10.33^{+0.08}_{-0.10}$
1065488	4.15	$8.01^{+0.42}_{-0.15}$	$0.75^{+0.08}_{-0.08}$	$1.31^{+0.34}_{-0.27}$	$1.6^{+0.5}_{-0.5}$	79^{+10}_{-12}	$10.27^{+0.21}_{-0.21}$
1025101	4.91	$8.99^{+0.29}_{-0.20}$	$0.95^{+0.17}_{-0.14}$	$0.95^{+0.04}_{-0.04}$	$15.4^{+52.8}_{-8.8}$	< 38	$10.45^{+0.47}_{-0.35}$
1090526	3.96	$9.93^{+0.12}_{-0.24}$	$1.08^{+0.38}_{-0.23}$	$2.35^{+0.14}_{-0.12}$	$0.4^{+0.5}_{-0.3}$	94^{+30}_{-38}	$10.47^{+0.21}_{-0.37}$
1089583	3.93	$9.01^{+0.16}_{-0.35}$	$0.72^{+0.29}_{-0.12}$	$1.10^{+0.17}_{-0.12}$	$2.0^{+0.5}_{-0.4}$	93^{+12}_{-14}	$10.44^{+0.16}_{-0.18}$
1090054	4.82	$9.62^{+0.04}_{-0.06}$	$1.07^{+0.06}_{-0.04}$	$1.07^{+0.04}_{-0.05}$	$1.8^{+0.2}_{-0.1}$	89^{+4}_{-4}	$10.36^{+0.03}_{-0.03}$
1082948	3.91	$10.68^{+0.08}_{-0.20}$	$1.96^{+0.38}_{-0.44}$	$1.95^{+0.13}_{-0.10}$	$0.8^{+2.4}_{-0.6}$	< 23	$8.72^{+0.46}_{-0.61}$

Table A3 – *continued*

JADES ID	z	$\log(M_\star[\mathrm{M}_\odot])$	$\log(\mathrm{SFR}\ [\mathrm{M}_\odot\ \mathrm{yr}^{-1}])$	r_e (kpc)	v/σ_0	σ_0 (km s^{-1})	$\log(M_\mathrm{dyn}[\mathrm{M}_\odot])$
1000110	4.06	$9.52^{+0.34}_{-0.08}$	$1.30^{+0.15}_{-0.11}$	$1.49^{+0.04}_{-0.04}$	$1.1^{+0.1}_{-0.1}$	166^{+7}_{-7}	$10.88^{+0.03}_{-0.04}$
1015037	4.38	$9.55^{+0.05}_{-0.09}$	$0.79^{+0.30}_{-0.10}$	$0.89^{+0.09}_{-0.07}$	$0.4^{+0.2}_{-0.2}$	86^{+14}_{-15}	$9.96^{+0.13}_{-0.16}$
1091153	4.07	$10.37^{+0.14}_{-0.14}$	$1.99^{+0.24}_{-0.23}$	$1.47^{+0.06}_{-0.05}$	$0.4^{+0.2}_{-0.1}$	154^{+17}_{-16}	$10.69^{+0.08}_{-0.09}$
1094903	3.87	$10.34^{+0.08}_{-0.23}$	$1.32^{+0.20}_{-0.20}$	$1.54^{+0.05}_{-0.05}$	$0.3^{+0.1}_{-0.1}$	192^{+12}_{-12}	$10.89^{+0.05}_{-0.05}$
1079264	4.05	$8.73^{+0.56}_{-0.30}$	$1.17^{+0.26}_{-0.08}$	$2.17^{+0.21}_{-0.17}$	$1.2^{+1.1}_{-0.4}$	< 73	$10.07^{+0.24}_{-0.43}$
1091614	4.06	$9.69^{+0.21}_{-0.41}$	$0.94^{+0.12}_{-0.12}$	$1.40^{+0.17}_{-0.12}$	$0.2^{+0.3}_{-0.1}$	99^{+21}_{-31}	$10.28^{+0.17}_{-0.30}$
1027279	4.15	$9.47^{+0.13}_{-0.29}$	$0.93^{+0.28}_{-0.11}$	$2.69^{+0.84}_{-0.61}$	$3.3^{+2.6}_{-1.2}$	76^{+18}_{-30}	$11.00^{+0.44}_{-0.46}$
1013488	3.80	$9.57^{+0.11}_{-0.33}$	$1.19^{+0.25}_{-0.11}$	$0.94^{+0.05}_{-0.04}$	$1.1^{+0.1}_{-0.1}$	119^{+7}_{-8}	$10.38^{+0.06}_{-0.06}$
1009935	4.89	$9.65^{+0.11}_{-0.25}$	$0.88^{+0.20}_{-0.24}$	$0.82^{+0.08}_{-0.07}$	$1.0^{+1.3}_{-0.5}$	< 65	$9.45^{+0.27}_{-0.47}$
1090891	3.92	$9.74^{+0.44}_{-0.22}$	$1.45^{+0.17}_{-0.11}$	$1.40^{+0.07}_{-0.06}$	$1.1^{+0.1}_{-0.1}$	186^{+6}_{-6}	$10.94^{+0.04}_{-0.04}$
1008197	4.40	$8.76^{+0.21}_{-0.24}$	$0.55^{+0.15}_{-0.12}$	$0.87^{+0.19}_{-0.13}$	$1.3^{+1.0}_{-0.5}$	63^{+18}_{-22}	$9.85^{+0.18}_{-0.19}$
1029814	4.16	$8.38^{+0.18}_{-0.17}$	$0.70^{+0.06}_{-0.06}$	$1.50^{+0.45}_{-0.32}$	$3.9^{+1.5}_{-1.2}$	49^{+10}_{-14}	$10.38^{+0.31}_{-0.28}$

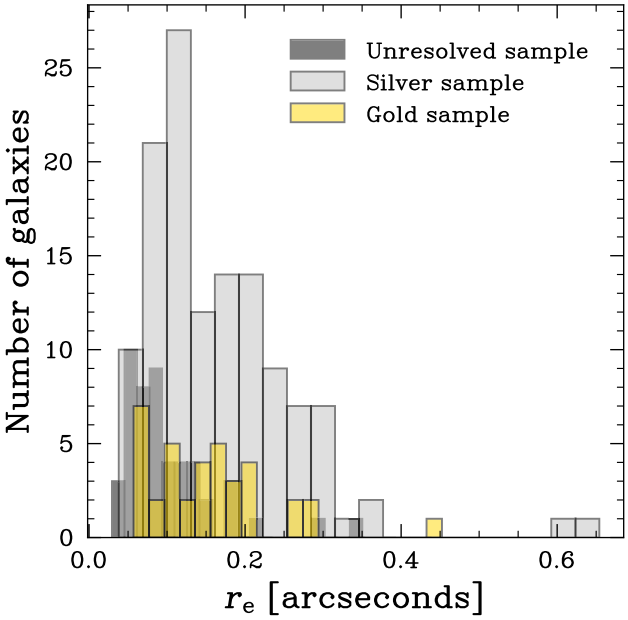

Figure A1. Effective radii r_e, in arcseconds, of the galaxies in our gold and silver sample.

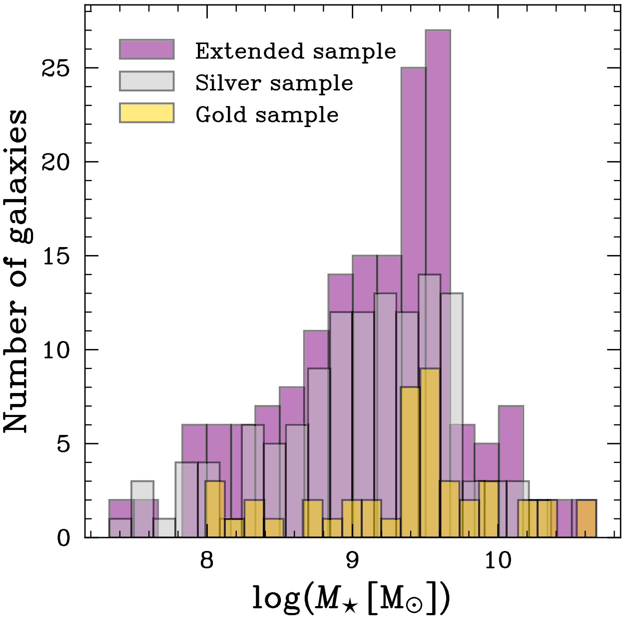

Figure A2. Stellar mass distribution of the galaxies in our gold, silver sample, and extended samples.

APPENDIX B: PCC ANALYSIS

We conduct a partial correlation coefficients (PCC) analysis in order to study the underlying correlations present in Fig. 9. As shown on Fig. B1, we infer the correlation between v/σ_0 (left panel) and σ_0 (right panel) and a range of parameters when controlling for stellar mass (pink) and SFR (purple), which are the parameters with the highest degree of influence. For both v/σ_0 and σ_0, the correlation is stronger for SFR when controlling for mass than vice-versa, which suggests that these two kinematic parameters are fundamentally related to SFR. The correlation with mass is therefore in part driven by the existing correlation with SFR, through the SFMS. Fig. B1 also highlights the strong dependence of v/σ_0 on σ_0 at high redshift where most galaxies do not have stable discs and hence have rotational velocities not strongly correlated with stellar mass.

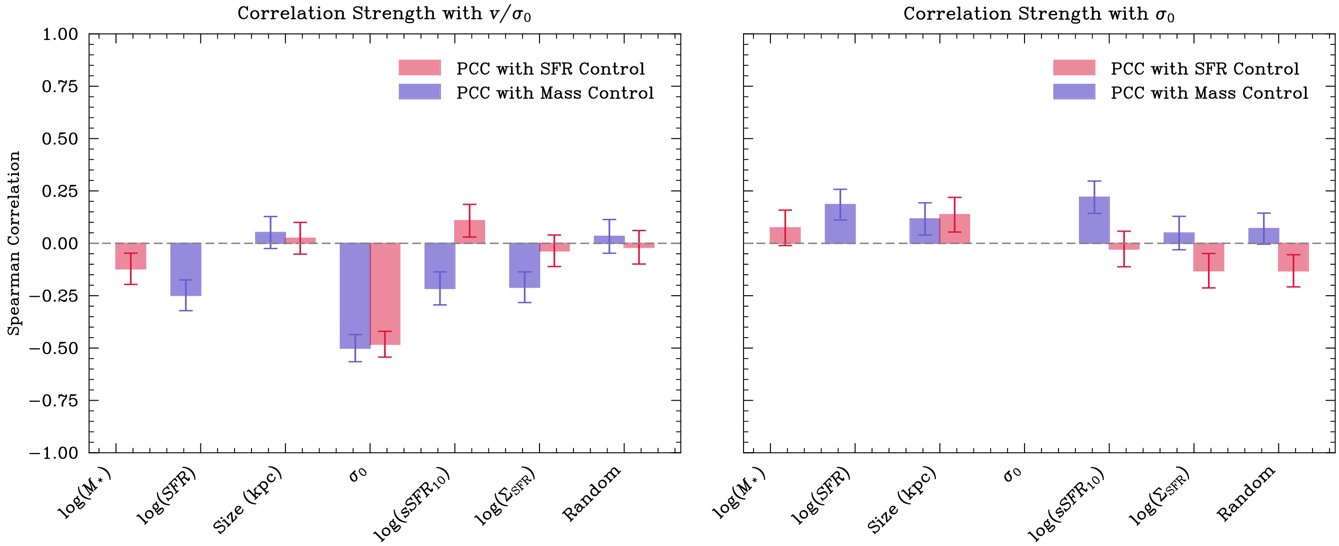

Figure B1. Results from a PCC analysis of the dependence of v/σ_0 and σ_0 on different galaxy parameters.

It is important to note that our sample size (≈ 160 when considering only the gold and silver samples) is relatively small and not well suited for PCC analyses, which typically have sample of the order of ∼ 1000. This can be seen through the biased correlation found for the randomized 'control' array in the case of σ_0. Having a larger sample helps mitigate the effect of outliers, for instance through the use of binning. For this reason, we do not include this analysis in the main body of the paper nor push this analysis further.

APPENDIX C: IMPACT OF SELECTION CUTS ON INFERRED CORRELATIONS

We will now discuss how the correlations presented in Sections 4.2.1 and 4.2.2 change if we only select rotation-supported galaxies and if we compute the rotational support v/σ_0 with $v_{\mathrm{obs,max}}$ instead of the velocity at the effective radius v_{re}. The results are summarized on Table C1, for correlations between σ_0 and v/σ_0 and $\log(M_\star\ [\mathrm{M}_\odot])$, SFR, sSFR, and SFR surface density. We find that the quantitative results do not change between scenarios, but the strength (ρ) and significance (p) of the correlations change. For the $\mathrm{v}/\sigma_0 > 1$ case, the correlations typically get weaker, but this is mostly driven by the significant decrease in sample size. For the $v_{\mathrm{rot}} = v_{\mathrm{obs,max}}$ case, the coefficients ρ stay consistent within 10 per cent.

APPENDIX D: FURTHER INVESTIGATION OF THE EFFECT OF SF ON KINEMATICS

We present in this section additional tests done to study the origin of the $\sigma_0 - \mathrm{SFR}$ correlation shown on Figs 9 and 10. As discussed in Section 4.2.1, this correlation naturally arises from models where gravitational instabilities, driven by radial transport of gas through the disc, and stellar feedback inject turbulence into the ISM. Both of these processes are linked to star formation, hence producing the observed trend. However, it is unclear which of these processes is the dominant driver at high redshift. The low masses probed $\log M_\star\ [\mathrm{M}_\odot] \lesssim 10$ make galaxies more unstable to gravitational instabilities, but also increase the impact of stellar feedback on the gas.

On Fig. D1 we show the $\sigma_0 - \mathrm{SFR}$ relation for the gold and silver sample in three redshift bins, along with the Spearman rank coefficient ρ and p-value p, computed for the resolved galaxies only. We see that in each bin, which all probe ≈ 0.2 Gyr, we do not find significant correlations. This implies that the $\sigma_0 - \mathrm{SFR}$ relation shown in Fig. 9, which is calculated for the extended sample across the full redshift range $z \sim 4 - 6$ probed by the work, could be mainly explained by the redshift evolution of the SFR and the stellar masses. However, we note that these bins suffer from reduced sample sizes compared to the full sample, so this naturally decreases the significance of any correlations.

Table C1. Spearman correlation coefficients (ρ) and p-values (p) for the four parameters cited in the paper, for v/σ_0 and σ_0 in the case where the full (extended) sample is used, when only rotationally supported galaxies $\mathrm{v}/\sigma_0 > 1$ are used, and when we use $v_{\mathrm{rot}} = v_{\mathrm{obs,max}}$ instead of $v_{\mathrm{rot}} = v_{\mathrm{re}}$.

Sample	v/σ_0 (full)	v/σ_0 ($\mathrm{v}/\sigma_0 > 1$)	v/σ_0 ($v_{\mathrm{rot}} = v_{\mathrm{obs,max}}$)	σ_0 (full)	σ_0 ($\mathrm{v}/\sigma_0 > 1$)
$\log(M_\star\ [\mathrm{M}_\odot])$	$\rho = -0.41$ $p < 0.001$	$\rho = -0.12$ $p = 0.416$	$\rho = -0.27$ $p = 0.014$	$\rho = 0.37$ $p = 0.001$	$\rho = 0.27$ $p = 0.071$
SFR_{10}	$\rho = -0.39$ $p < 0.001$	$\rho = -0.18$ $p = 0.242$	$\rho = -0.35$ $p = 0.001$	$\rho = 0.42$ $p < 0.001$	$\rho = 0.22$ $p = 0.149$
sSFR_{10}	$\rho = 0.26$ $p = 0.019$	$\rho = 0.05$ $p = 0.746$	$\rho = 0.12$ $p = 0.277$	$\rho = -0.20$ $p = 0.078$	$\rho = -0.20$ $p = 0.199$
Σ_{SFR}	$\rho = -0.35$ $p = 0.001$	$\rho = -0.25$ $p = 0.102$	$\rho = -0.40$ $p < 0.001$	$\rho = 0.30$ $p = 0.007$	$\rho = 0.16$ $p = 0.283$

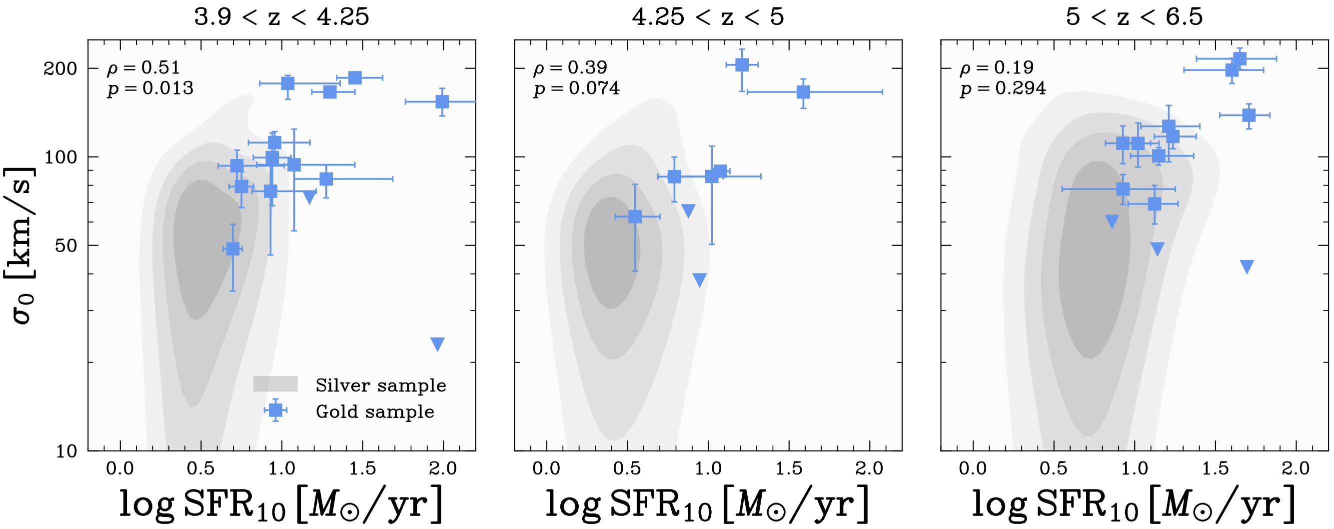

Figure D1. σ_0 – SFR relation for our gold (blue squares) and silver (grey contours) samples in three redshift bins spanning ≈ 0.2 Gyr each. We show the Spearman rank correlation coefficients (ρ) and p-values (p) computed from the extended galaxies only, and find no significant correlations in the individual bins.

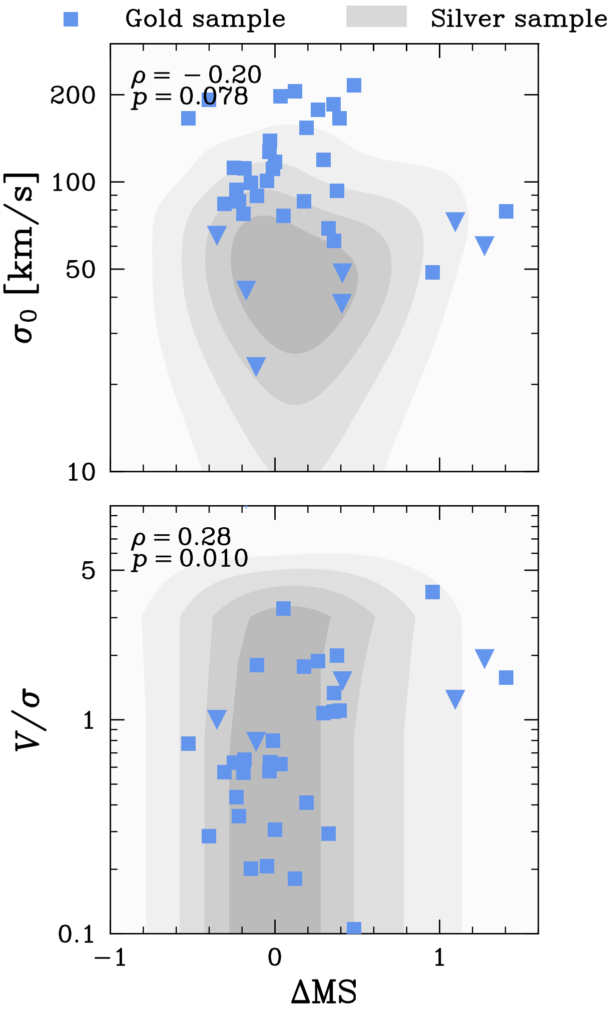

Figure D2. Evolution of σ_0 (top panel) and v/σ_0 (bottom panel) with the offset from the SFMS (Simmonds et al. 2025) $\Delta\mathrm{MS} = \mathrm{SFR}/\mathrm{SFR}_{\mathrm{MS}}$. We plot our gold (blue squares) and silver (grey contours) samples, and find no significant trends, as highlighted by the Spearman correlation coefficients ρ and p-values p, which are computed for the extended sample.

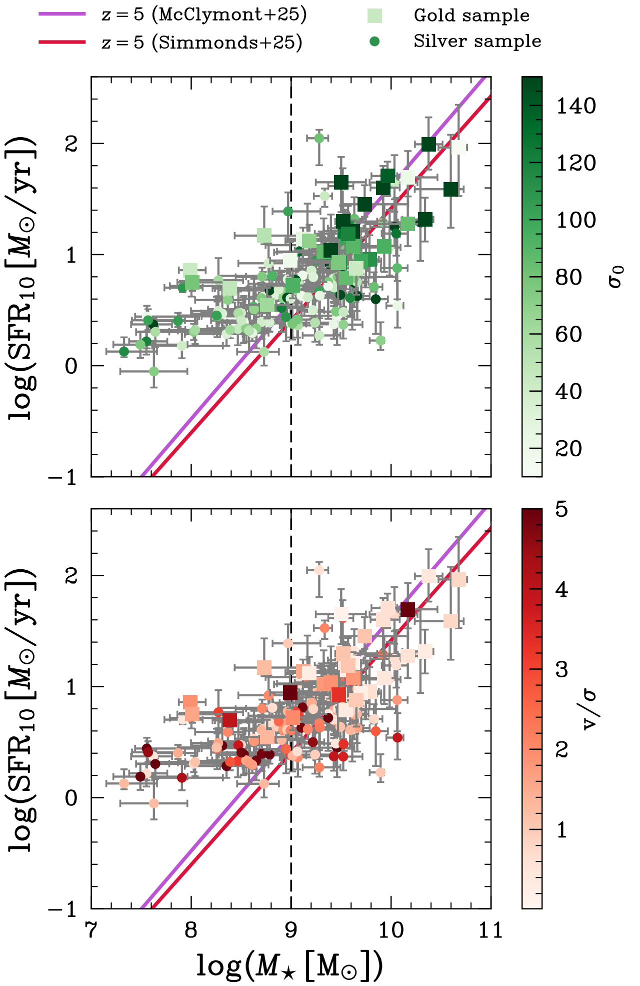

Figure D3. Distribution of our gold (squares) and silver (circles) samples on the $M_\star$ – SFR plane, colourcoded by intrinsic velocity dispersion σ_0 (top panel) and rotational support v/σ_0 (bottom panel). We plot the SFMS prescriptions from McClymont et al. (2025a) and (Simmonds et al. 2025).

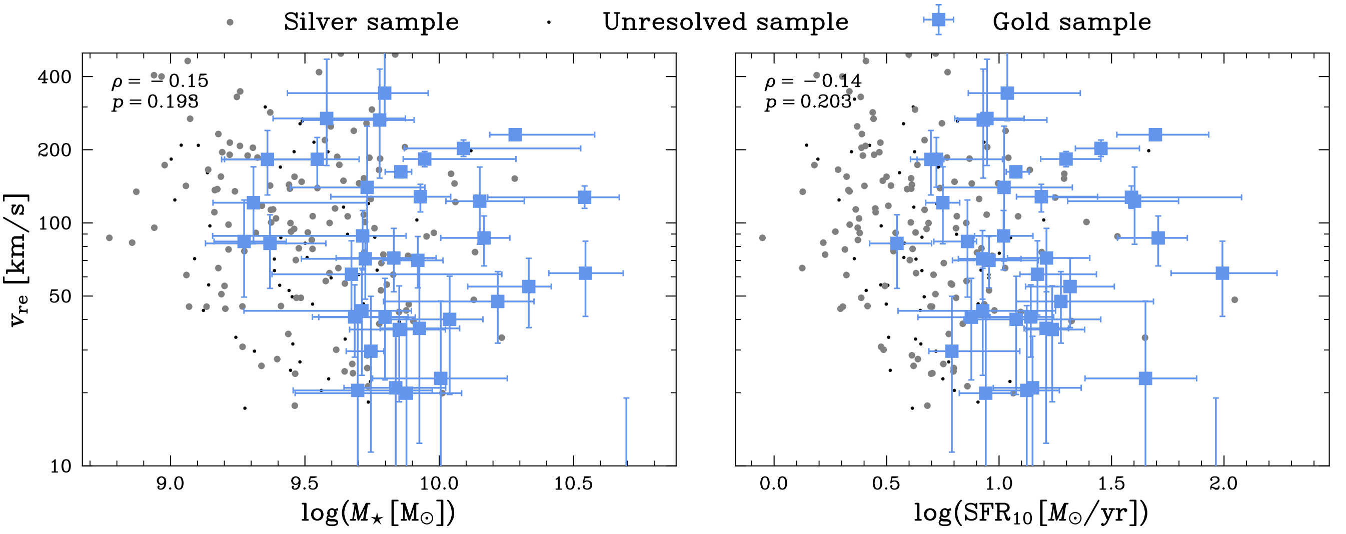

Figure D4. Rotational velocity $v_{\rm rot} = v_{\rm re}$ as a function of stellar mass $\log M_\star$ [M$_\odot$] (left panel) and SFR (right panel), for the gold (blue squares), silver (grey circles), and unresolved (black dots) samples.

We further investigate the role of stellar feedback and gravitational instabilities by exploring trends with the offset from the main sequence $\Delta{\rm MS} = {\rm SFR}/{\rm SFR}_{\rm MS}$, as shown on Fig. D2 for our gold and silver samples. We use the SFMS prescription from Simmonds et al. (2025) (Fig. 2). Although we find no correlation between σ_0 and ΔMS, we find a slight positive correlation between σ_0 and ΔMS ($\rho = 0.19$), although the significance $p = 0.094$ is low. However, the trend is not significant enough to draw conclusions. This is overall consistent with findings from Übler et al. (2019).

Finally, we explore the distribution of σ_0 and v/σ_0 on the $M_\star - {\rm SFR}$ plane and plot our results on Fig. D3. There is no clear trend relating the kinematics to this plane, it appears that on average, galaxies with high rotational support $v/\sigma_0 > 3$ lie close to the SFMS. An in-depth study of these results would require the study of individual galaxies on this plane in order to try to uncover the drivers of rotational support in each case, but this is beyond the scope of this work.

When studying correlations between v/σ_0 and physical properties such as SFR and stellar masses, it is interesting the study the role of both $v = v_{\rm rot}$ and σ_0 in driving the observed trends. On Fig. D4 we show the relations between the rotational velocity and $\log M_\star$ [M$_\odot$] and SFRs. We find no correlation in both cases, meaning that at these redshifts $z \gtrsim 4$ and stellar masses $\log M_\star$ [M$_\odot$] $\lesssim 10$, rotational velocity does not strongly depend on stellar mass. This implies that the correlations measured on Fig. 9 are mainly driven by the evolution of σ_0.

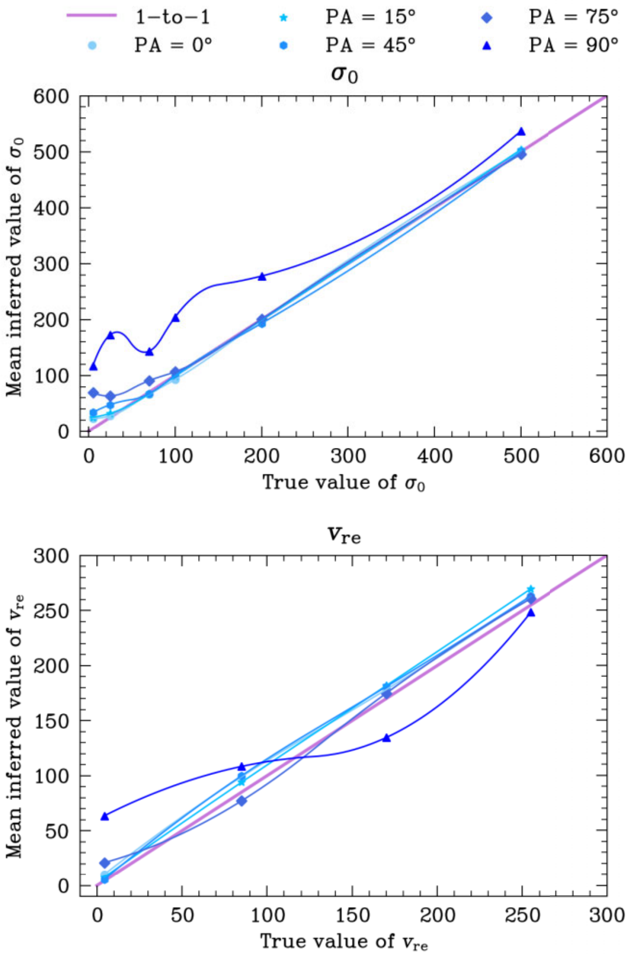

Figure E1. Results of recovery tests for σ_0 (top panel) and $v_{\rm re}$ (bottom panel), for mock galaxies with a range of PAs PA $= 0 - 90°$. The mean values are computed by averaging over tests done with a range of rotational velocities $v_{\rm re} = 5$–250 km s^{-1}, for σ_0, and velocity dispersions $\sigma_0 = 5$–500 km s^{-1}, for $v_{\rm re}$.

APPENDIX E: GEKO RECOVERY TESTS

In this section, we present the key recovery tests done for our tool GEKO. The full presentation of the code and the tests will be done in an upcoming dedicated paper (Danhaive et al., in preparation). On Fig. E1 we show the results for the recovery of the key model-derived parameters σ_0 and $v_{\rm re}$ (which are used to compute v/σ_0), for different angles of mock galaxies with respect to the dispersion direction PA $= 90°$. These tests are done on mock data, with an integrated S/N = 40, and a range of velocity dispersions $\sigma_0 = 5 - 500$ km s^{-1} and rotational velocities $v_{\rm re} = 5$–250 km s^{-1}. The values plotted

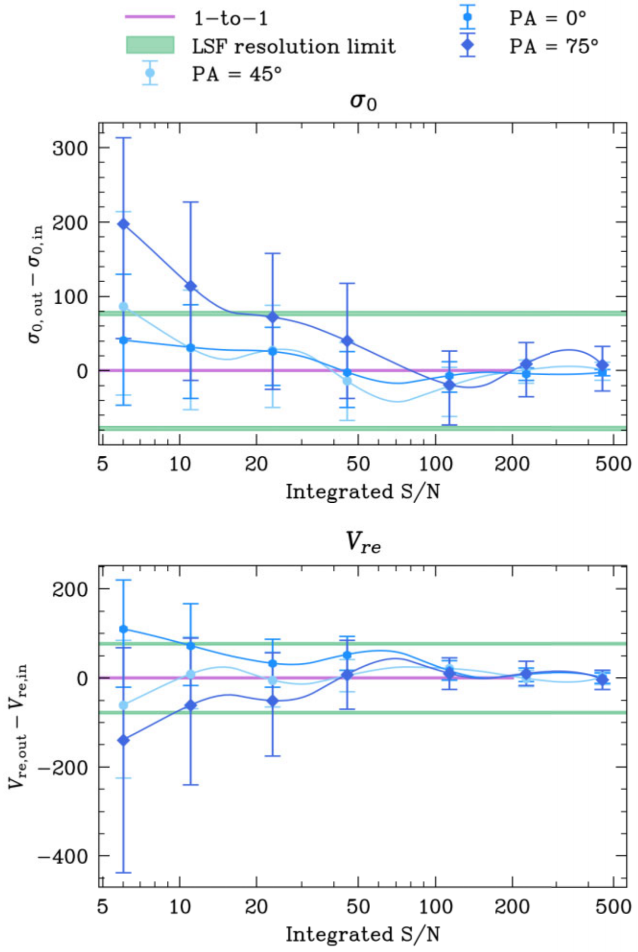

Figure E2. Results of recovery tests for σ_0 (top panel) and v_{re} (bottom panel) for integrated S/N = 6 − 500. The mock galaxy has $\sigma_0 = 100$ km s^{-1} and $v_{\mathrm{re}} \approx 170$ km s^{-1}.

on Fig. E1 are averaged over all values of v_{re} for the σ_0 recovery test and vice-versa. When the galaxy is parallel to the dispersion direction, we are not able to accurately recover σ_0, which is artificially boosted. This unphysical value of σ_0 is driven by the degeneracy between morphology,velocity, and velocity dispersion when the galaxy is parallel to the slit. For this reason, we discard galaxies with PA > 75°. As shown on Fig. E1, our results converge to the true values, within uncertainties, when PA < 75°, which is why we use this cut to define our sample. We obtain the best recovery when galaxies as perpendicular to the dispersion direction, PA = 0°. We can further see that, for cases PA < 15°, we are able to recover values of $\sigma_0 \approx 20$ km s^{-1}, which is well below the instrument LSF $\sigma_0 \approx 80$ km s^{-1}.

We also test the effect of integrated S/N on our ability to recover kinematic parameters for our mock galaxies. We show the results on Fig. E2, for $\sigma_0 = 100$ km s^{-1} and $v_{\mathrm{re}} = 170$ km s^{-1}. Beyond S/N = 10, the recovered value of σ_0 is consistent with the true input value within the uncertainties. We set S/N > 10 as our cut for the silver sample, and S/N > 20 for the gold sample. The uncertainty decreases with increasing S/N and decreasing PA.

APPENDIX F: COMPARISON TO $z < 4$ MEASUREMENTS

In this section, we briefly introduce the studies we compare our measurements to (Figs 8, 7, and 10) and discuss how their methods differ from those used in this work and how that may affect the direct comparisons we make.

The MOSFIRE Deep Evolution Field (MOSDEF) survey data are described in Price et al. (2020), and is obtained using the MOSFIRE spectrograph on the Keck telescope. This survey is comprised of rest-frame optical 2D moderate-resolution spectra $R \sim 3000 - 3600$ for galaxies in the CANDELS field at $z \sim 1.4 - 3.8$. The kinematic analysis is restricted to galaxies whose major axis is roughly aligned with the slit and that are spatially resolved. Their final sample is made up of ∼ 700 galaxies detected in Hα, [O III], and Hβ, in order of availability. Their kinematic modelling is similar to the one adopted in this paper. They assume an intrinsic axis ratio (i.e. axis ratio for an edge-on view) $(b/a)_0 = 0.19$, and model the velocities with an arctangent model and a constant velocity dispersion across the galaxy. Using inferred posterior distributions, they compute σ_0 and the rotational support, which they define as $v_{2.2}/\sigma_0$ where $v_{2.2} = V(r = 2.2r_s)$. This is important to note as typically $v_{2.2} > v_{\mathrm{re}}$, which can boost the v/σ_0 measurements compared to those in this work.

The K-band multi-object spectrograph (KMOS)^{3D} survey data described in Wisnioski et al. (2015) is obtained using the KMOS IFS on Keck. Galaxies are observed in Hα across five deep fields (COSMOS, GOODS-S, GOODS-N, UDS, and AEGIS) and span redshifts $z \sim 0.7 - 2.7$. For the kinematic fitting, each spaxel is fit with a 1D Gaussian model including the instrument LSF. The velocity dispersions are computed in the outer regions that are less affected by beam smearing. They define the rotational support v/σ_0 with $v_{\mathrm{rot}} = v_{\mathrm{obs}}/\sin i$, where v_{obs} is an observed velocity difference from the maximal and minimal velocities of the velocity axis profile. This overall velocity gradient is usually greater than the velocity measured at the effective radius, which could bias the measurements high compared to this work.

The SIGMA survey (Simons et al. 2016, 2017) is a Keck/MOSFIRE survey, which targeted 97 $z \sim 2$ star-forming galaxies in the GOODS-S, GOODS-N, and UDS fields, detected in Hα or [O III]. The kinematic modelling assumes an arctangent velocity model and $q_0 = 0.2$. The velocity used for the rotational support represents the asymptotic velocity measured in the flat outer end of the rotation curve.

The KMOS Deep Survey (KDS) survey is described in (Turner et al. 2017b). Galaxies at $z \sim 3.5$ are observed through their [O III] emission, where the ionized gas kinematics are computed using an arctangent model. The rotational velocity is computed as the best-fitting velocity at $r = 2r_e$, which is comparable to the velocity at the radius enclosing 80 per cent of the total light v_{80} (Tiley et al. 2016). In the thin disc model, we expect the rotation curve to increase beyond r_e, where it is measured in this work, so the velocities at $r = 2r_e$ could be higher. However, the velocities for a thick exponential disc $n = 1$ would peak at $r \approx 1.38r_e$, so the relation between velocities at $r = r_e$ and $r = 2r_e$ varies depending on the object.

The KROSS survey (Johnson et al. 2018) is also a KMOS survey which observed ∼ 800 star-forming galaxies at $z \sim 1$ using Hα. The kinematic modelling assumes an intrinsic axis ratio $q_0 = 0.2$ and computes the velocity for the rotational support as the velocity at $r = 2r_e$. Both this velocity and the velocity dispersion are computed along the major kinematic axis. However, different from our work, the velocity curve is modelled as an exponential disc. At the small radii probed by the grism data, this curve is similar to the arctangent curve we use, so this should not affect our comparison. The Multi-Unit Spectroscopic Explorer (MUSE; Bacon et al. 2010) samples is presented in (Swinbank et al. 2017) and covers galaxies at redshifts $0.28 < z < 1.49$. The MUSE measurements shown in this work are those presented in Johnson et al. (2018), and are corrected, when necessary, to match measurements for the KROSS sample and provide an accurate comparison. The kinematics for these two samples are both derived from ionized gas.

The Sydney/AAO Multi-object Integral-field spec- trograph (SAMI; Croom et al. 2012) Galaxy Survey (Allen et al. 2015; Green et al. 2018) is a census of local Universe galaxies, probing both stellar and gas kinematics. The SAMI measurements shown in this work are from Varidel et al. (2020).

The SINS/zC-SINF AO survey (Förster Schreiber et al. 2018) is a survey of 35 galaxies at $z \sim 2$, probing kinematics and star formation with Hα and [N II] lines. The rotational velocity is chosen as the maximum observed velicity difference along the kinematic major axis, similar to Wisnioski et al. (2015). An isotropic velicity dispersion σ_0 is assumed. (Förster Schreiber et al. 2018) report kinematic measurements consistent with those from the KMOS survey at similar redshifts (Wisnioski et al. 2015; Wuyts et al. 2016b; Übler et al. 2017), and are hence comparable.

The Gassendi Hα survey of SPirals (GHASP; Epinat, Amram & Marcelin 2008; Epinat et al. 2010) contains Fabry-Perot observations of Hα in 203 local galaxies. For the kinematic modelling, Epinat et al. (2010) a thin planar disc is assumed, and a variety of rotation curves are used based on how well they fit the observed rotation in each system. However, all remain failry consistent with our arctagent curve within the radii probed in this work. The nature of the data and the modelling approach make a one-to-one comparison difficult, but none the less provide an indication of galaxy kinematics in the local Universe.

The the Mapping Nearby Galaxies at Apache Point Observatory (MaNGA; Bundy et al. 2015) survey measurements shown for comparison in this work are from Yu et al. (2019). The sample contains spatially resolved Hα measurements for 2716 galaxies in the local Universe. The velocity dispersion is inferred by staking the 1D Hα line from each spaxel and correcting for the instrument resolution and beam smearing.

The de Graaff et al. (2024a) measurements are obtained using the *JWST* NIRSpec MSA 2D spectra. The assumptions adopted in the kinematic modelling are the same as the ones used in this work. However, the NIRSpec slits suffer from slit-losses, which are described in the paper and accounted for in the forward-modelling of the instrument.

The sample from Parlanti et al. (2023) is selected from the public ALMA data archive and is composed of 22 galaxies at high redshift ($4.2 < z < 7.6$). The galaxies are observed in the [C II] or [O III] emission lines, or both. The rotational velocity is modelled using a bulge component and an exponential disc component. The rotational velocity is defined as the maximum observed velocity, which is typically higher than the velocity measured at r_e, as previously discussed. The cold gas measurements from the [C II] emission line have lower velocity dispersions on average, as shown in (Parlanti et al. 2023), than measurements from ionized gas ([O III] and Hα).

We also compare our results with predictions from the TNG simulations (Pillepich et al. 2019), where they compute kinematic properties in the following way. The rotational velocity $v_{\rm rot}$ is the absolute maximum of a galaxy's rotation curve along its structural major axis, from its edge-on projection and within twice the stellar half-mass radius. The dispersion σ_0 is the value of the velocity dispersion from a face-on projection of a galaxy, averaged in pixels of 0.5 ckpc a side that lie along the structural major axis and between one and two the stellar half-mass radius.

We do not discuss the cold gas local Universe measurements as they are only shown in Fig. 7 to compare to local Universe measurements of ionized gas (for further details, see Übler et al. 2019).

APPENDIX G: GOLD SAMPLE FITS

Here we present the GEKO summary plot, which shows the best-fitting model compared to the grism data, of all of the objects in the gold sample, whose properties are summarized in Table A3. For a full description of the structure of this plot see Section 3.4 and Fig. 4. We note that hot or dead pixels are masked in the fitting process, but not in the summary plots.

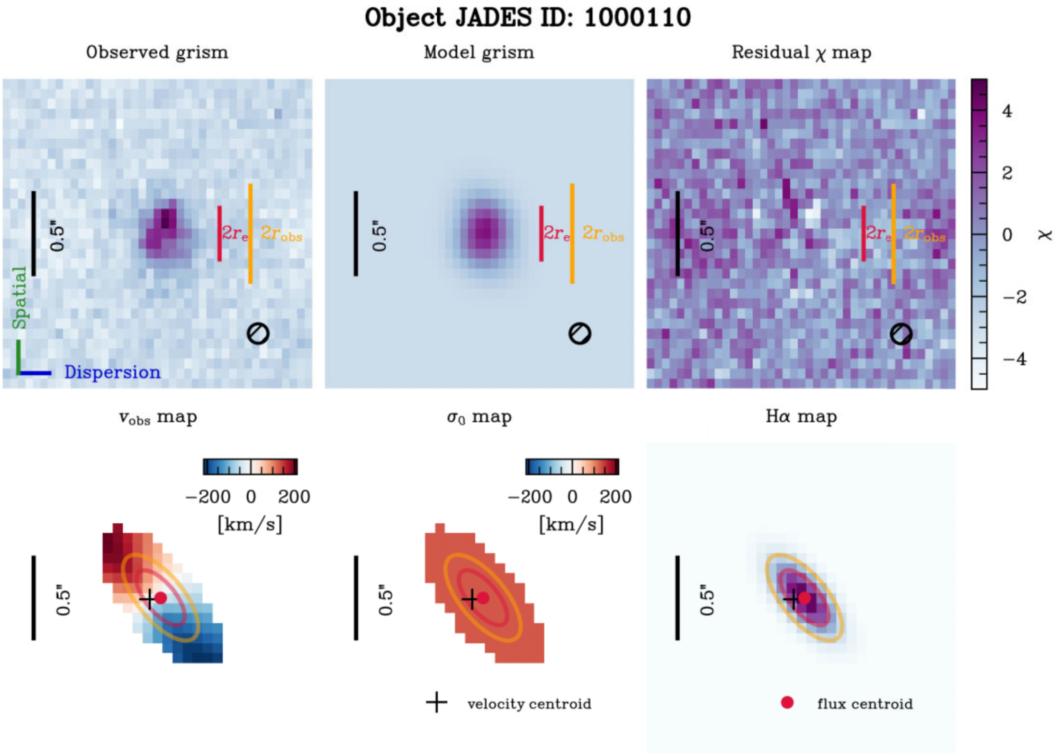

Figure G1. GEKO summary plots for the objects in the gold sample. The JADES ID for each object is marked at the top. The left-hand panel shows the residuals of the model with respect to the observed grism, along with the best-fitting velocity, velocity dispersion, and intrinsic emission maps. For a full description of the structure of this plot see Section 3.4 and Fig. 4.

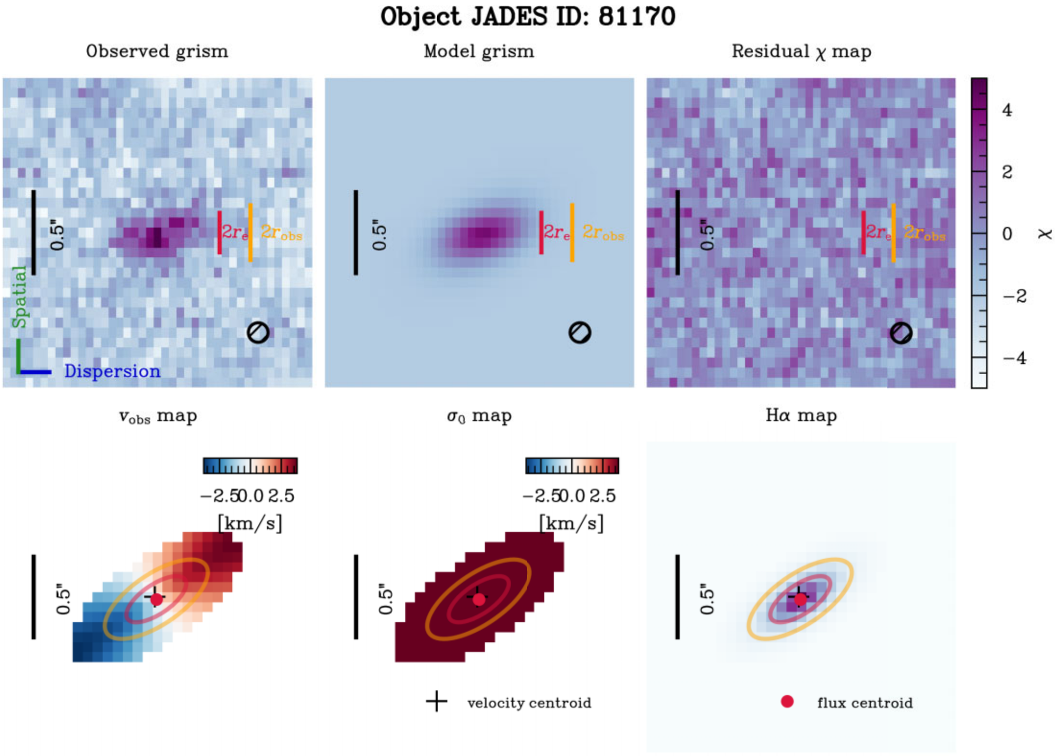

Figure G1. – *continued*

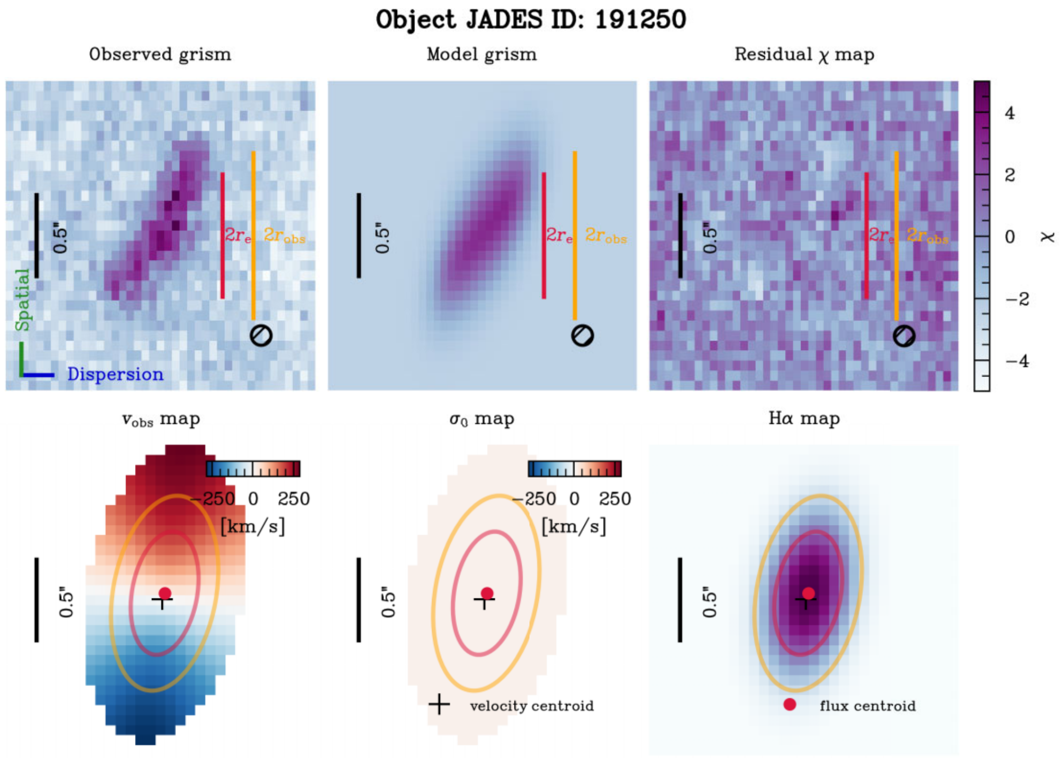

Figure G1. – *continued*

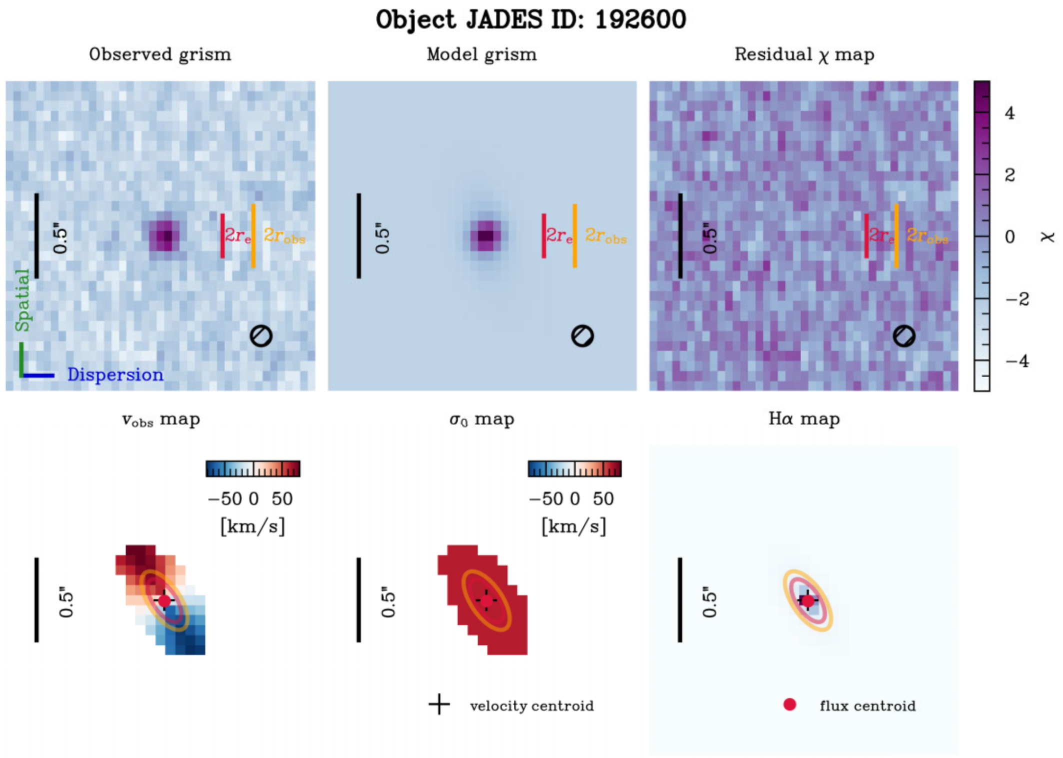

Figure G1. – *continued*

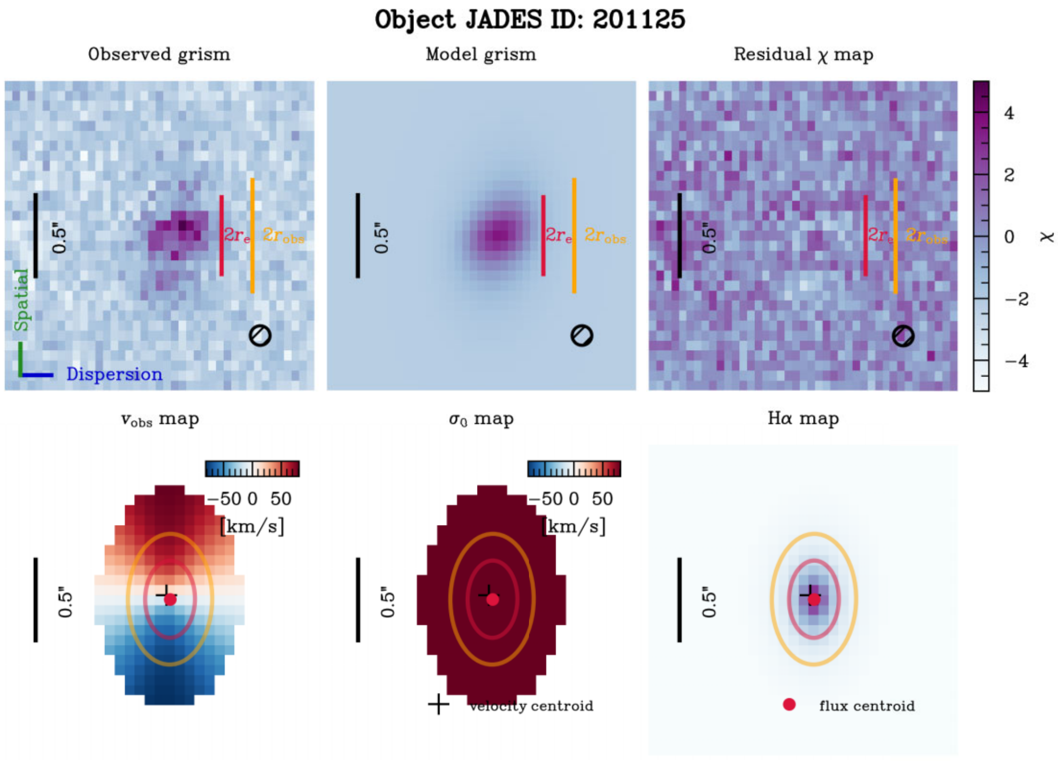

Figure G1. – *continued*

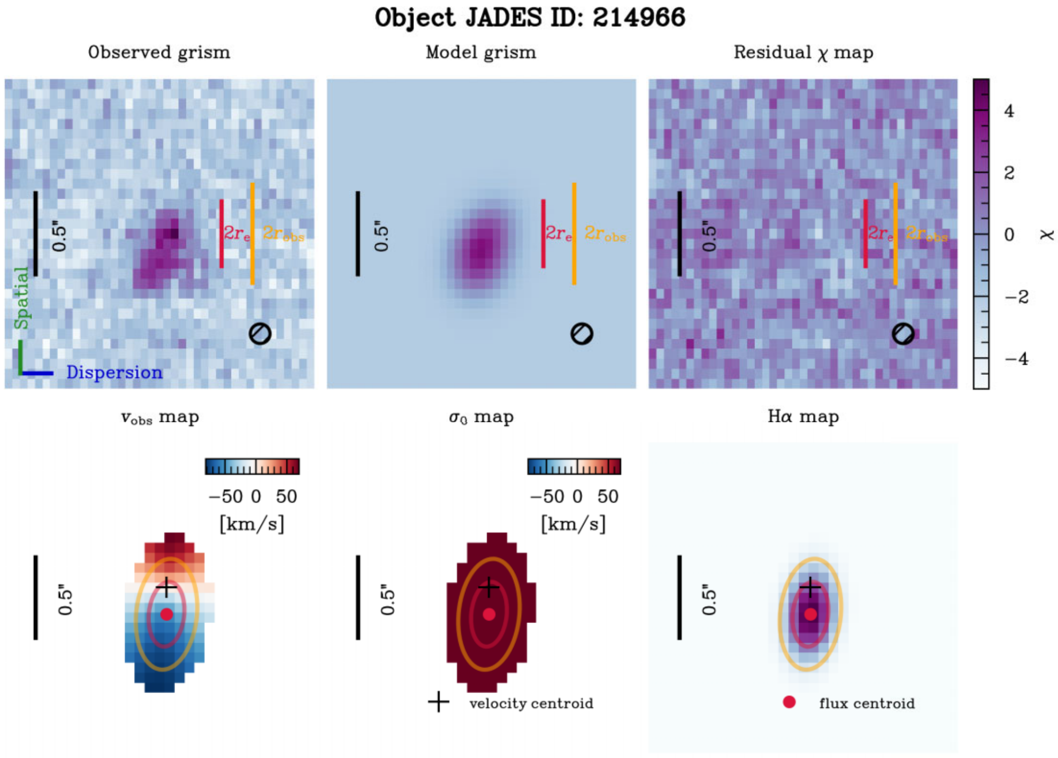

Figure G1. – *continued*

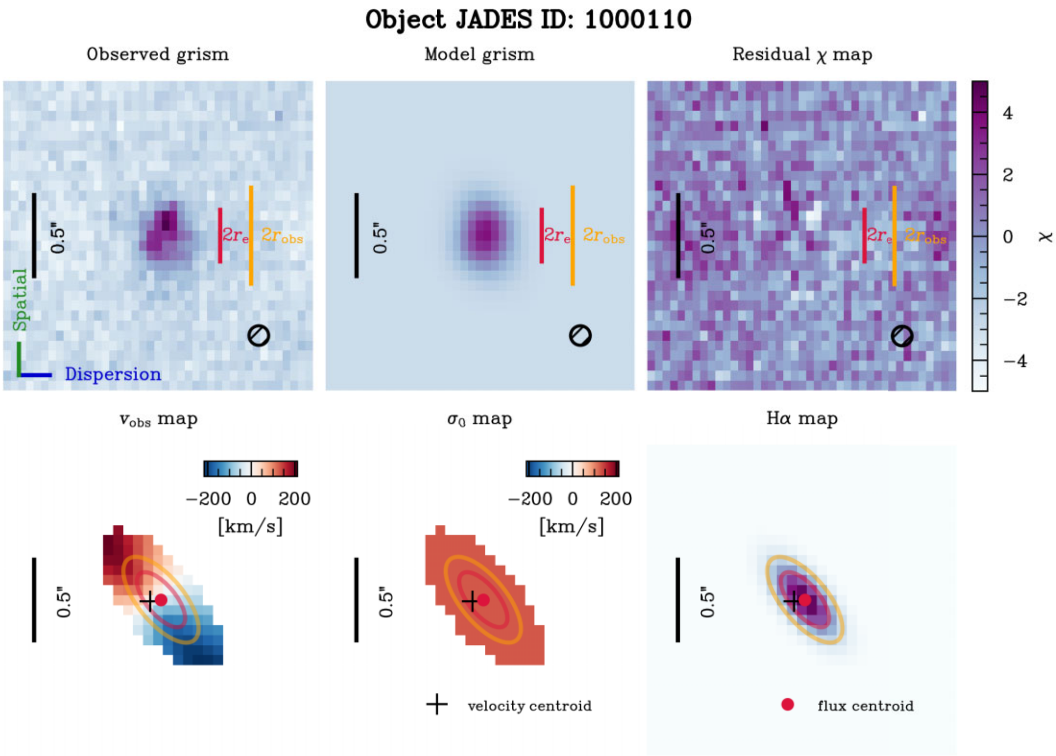

Figure G1. – *continued*

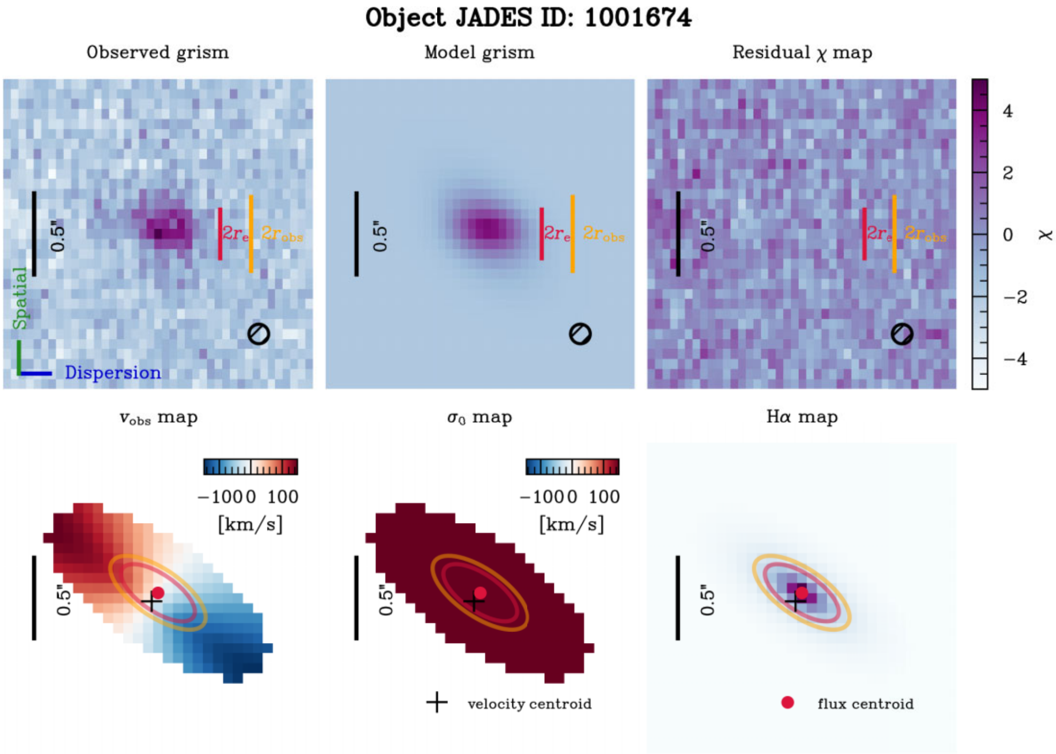

Figure G1. – *continued*

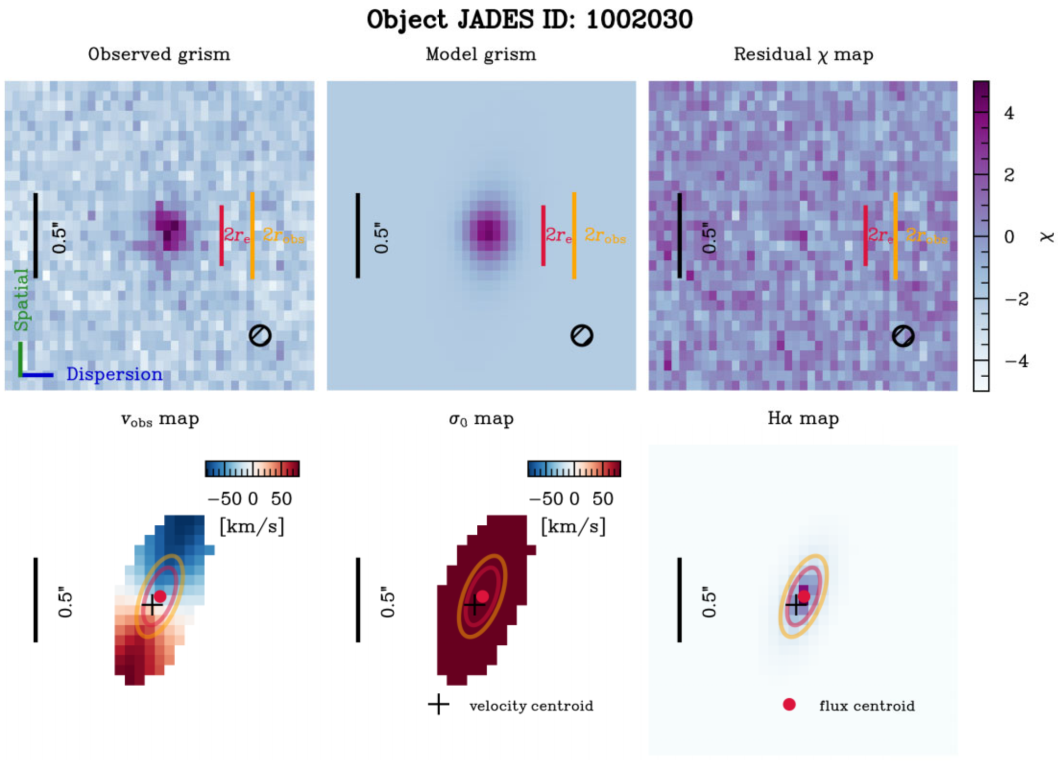

Figure G1. – *continued*

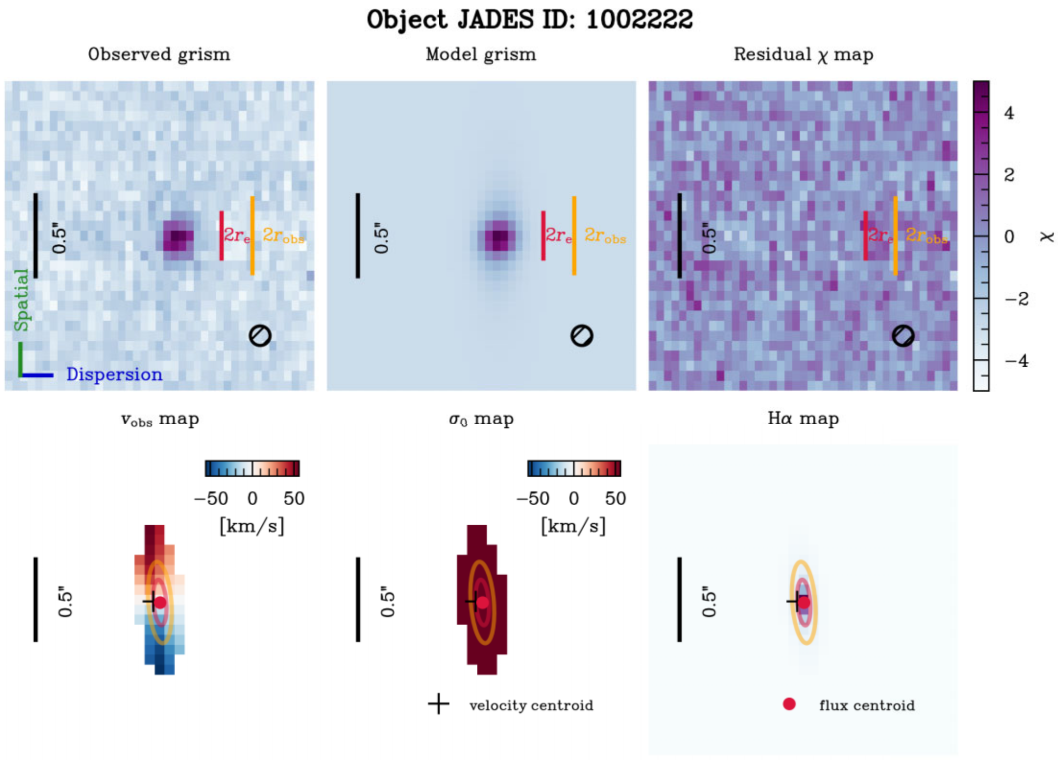

Figure G1. – *continued*

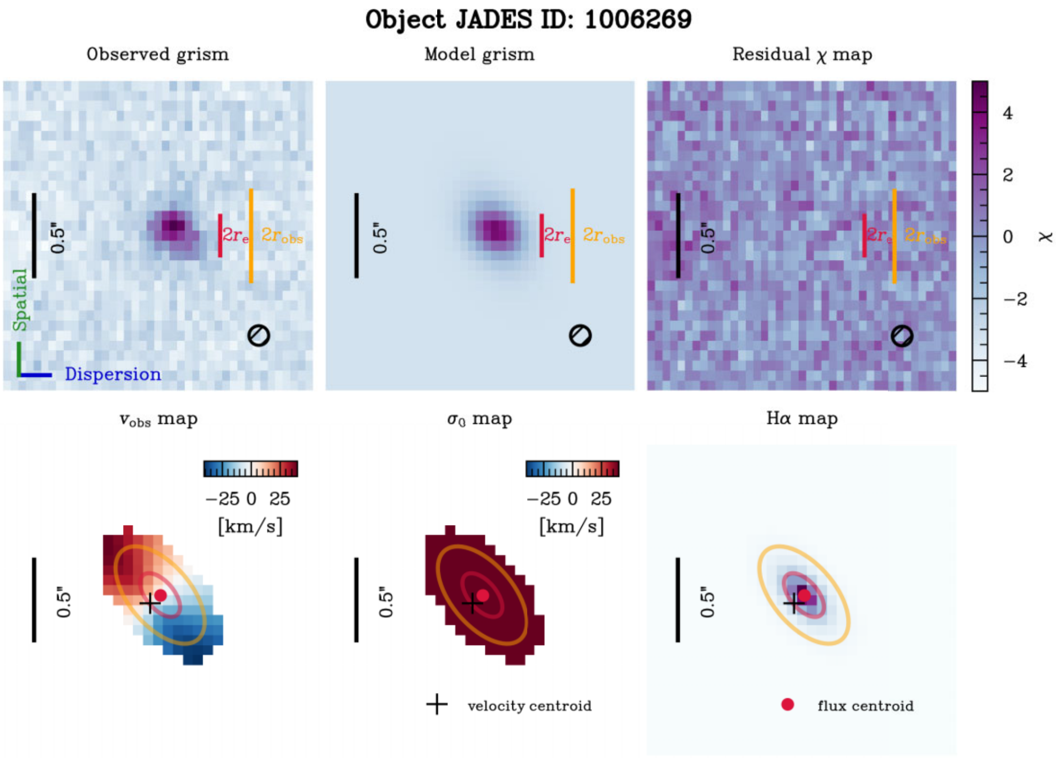

Figure G1. – *continued*

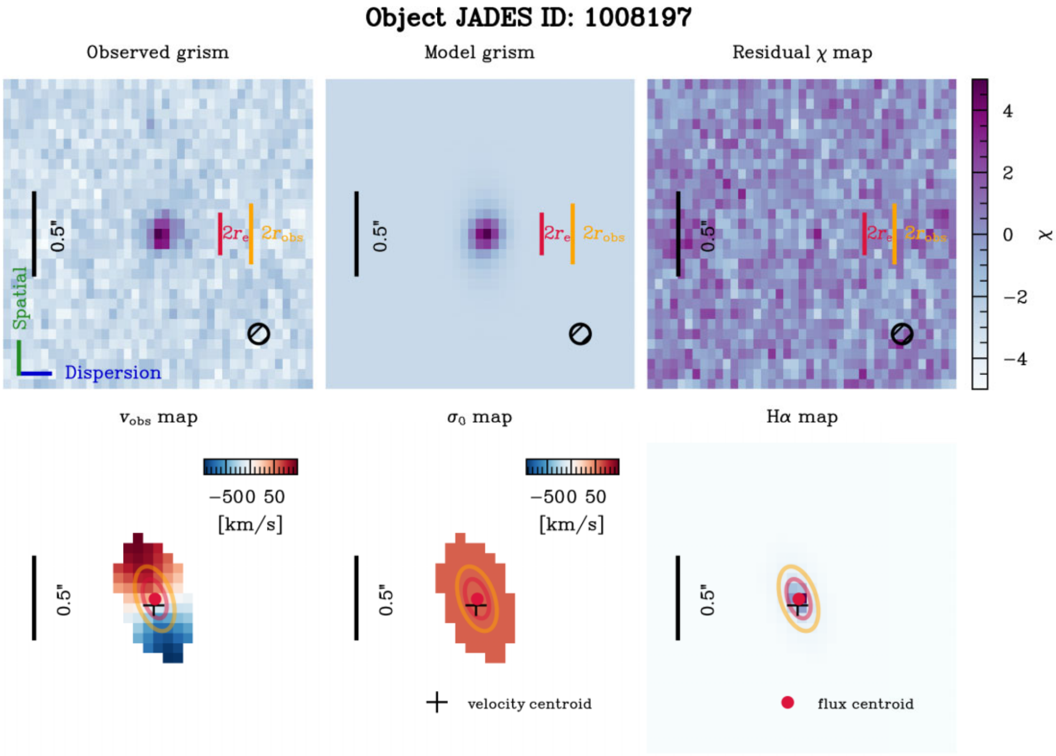

Figure G1. – *continued*

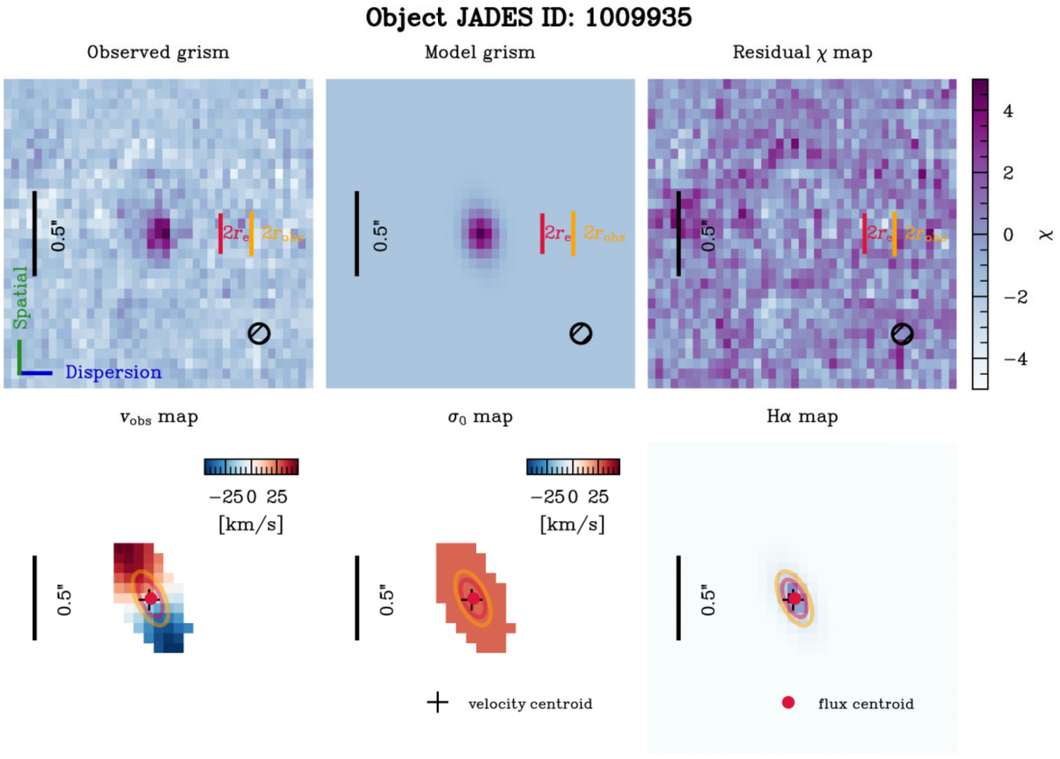

Figure G1. – *continued*

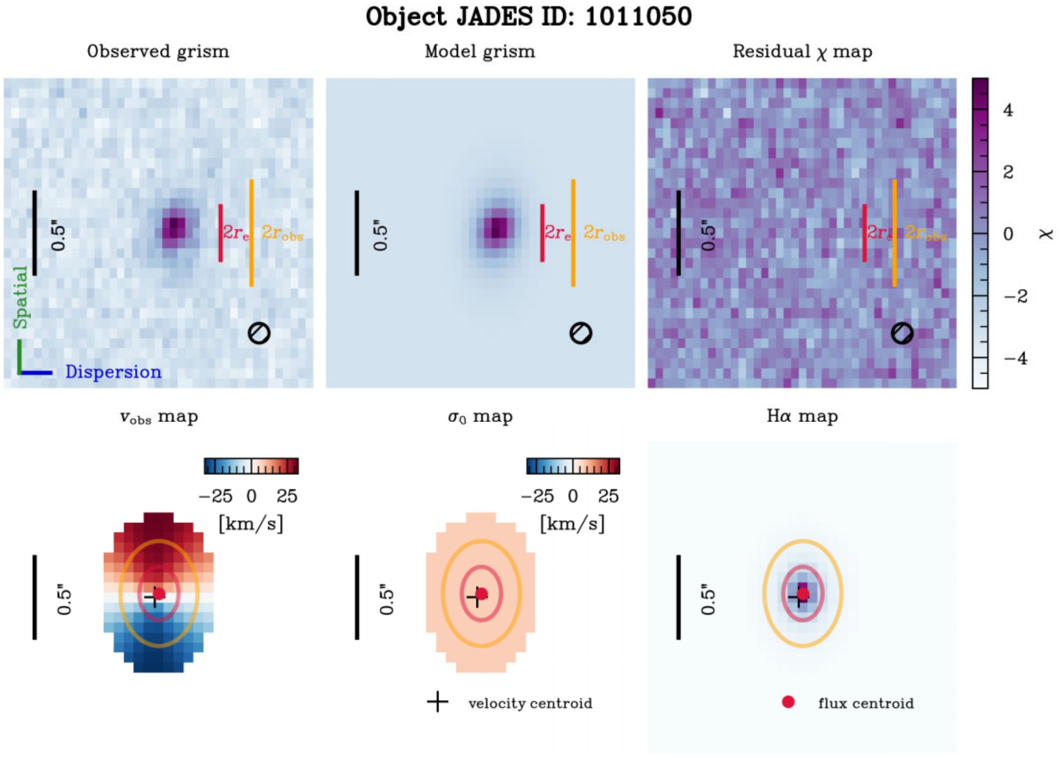

Figure G1. – *continued*

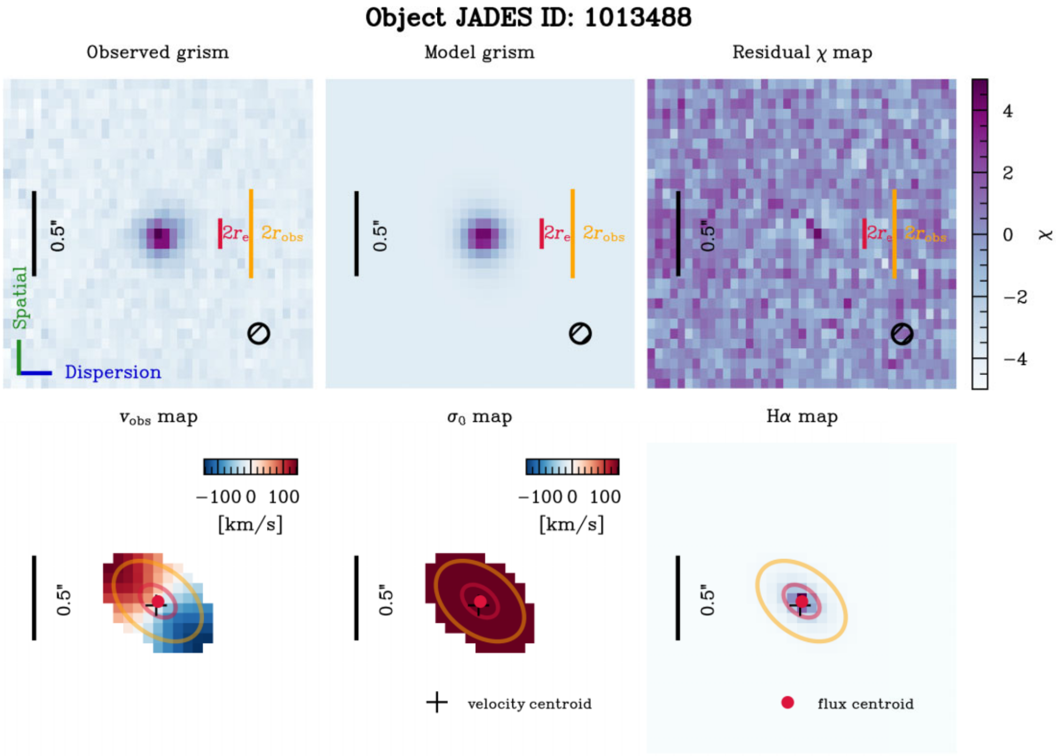

Figure G1. – *continued*

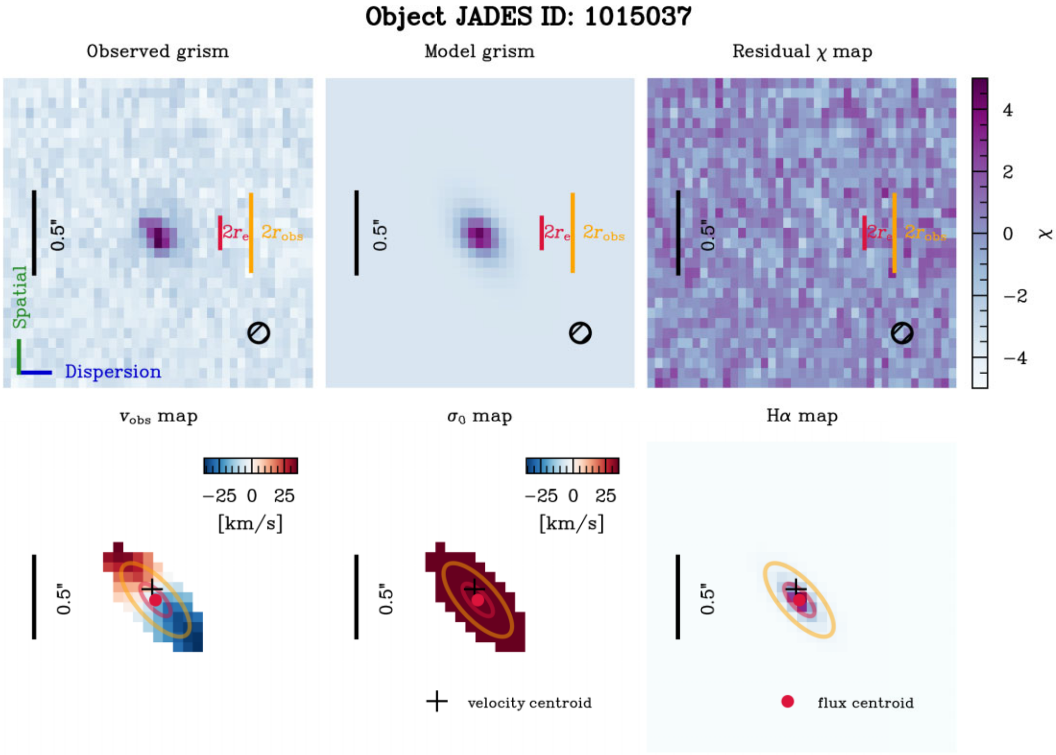

Figure G1. – *continued*

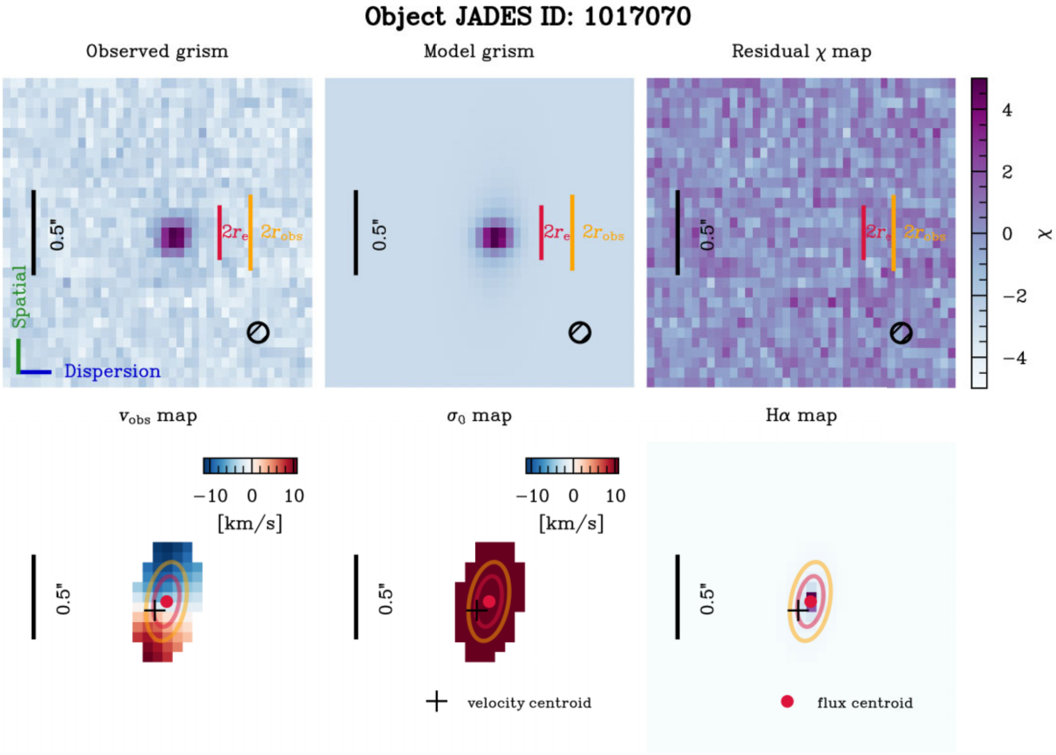

Figure G1. – *continued*

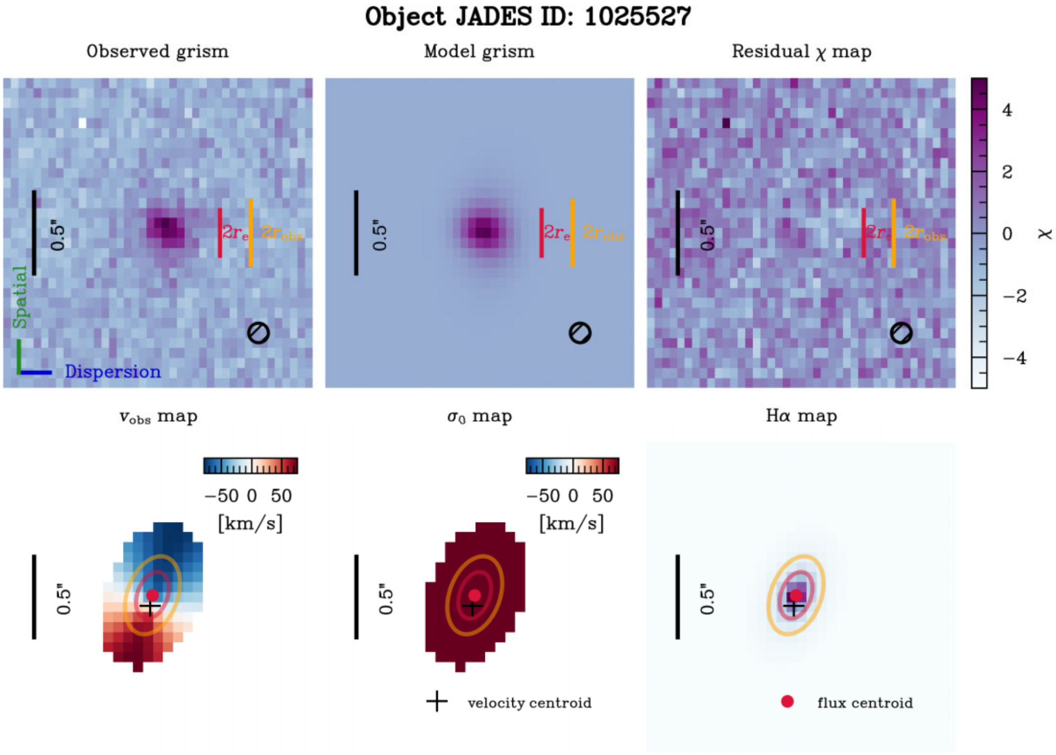

Figure G1. – *continued*

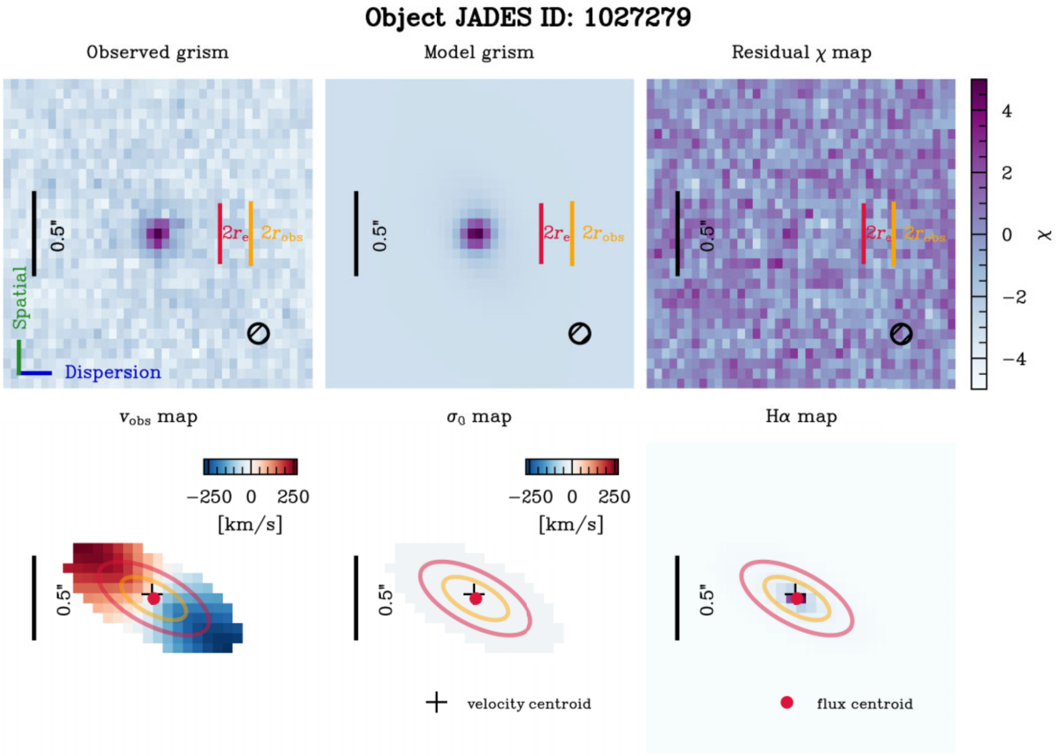

Figure G1. *– continued*

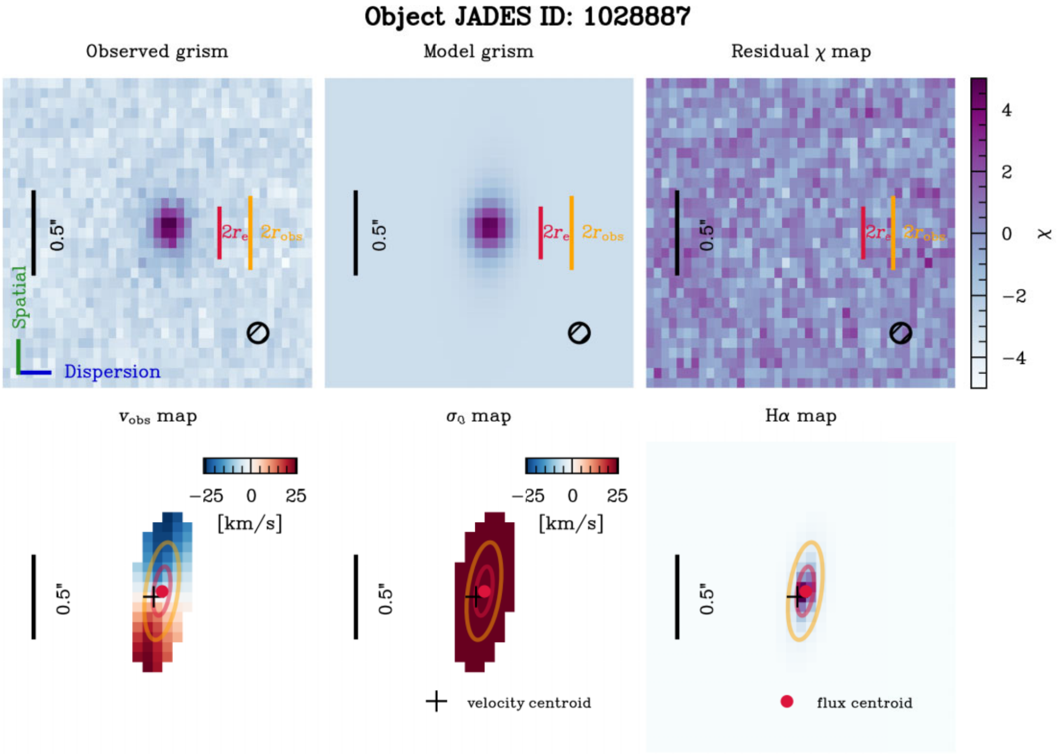

Figure G1. *– continued*

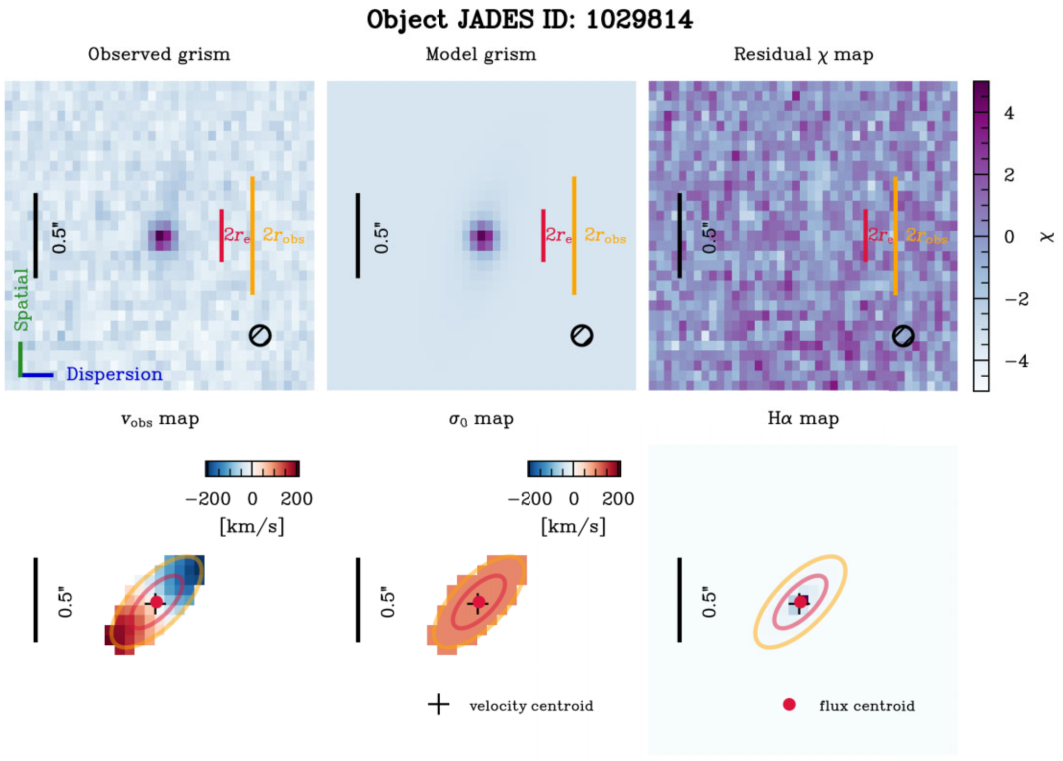

Figure G1. – *continued*

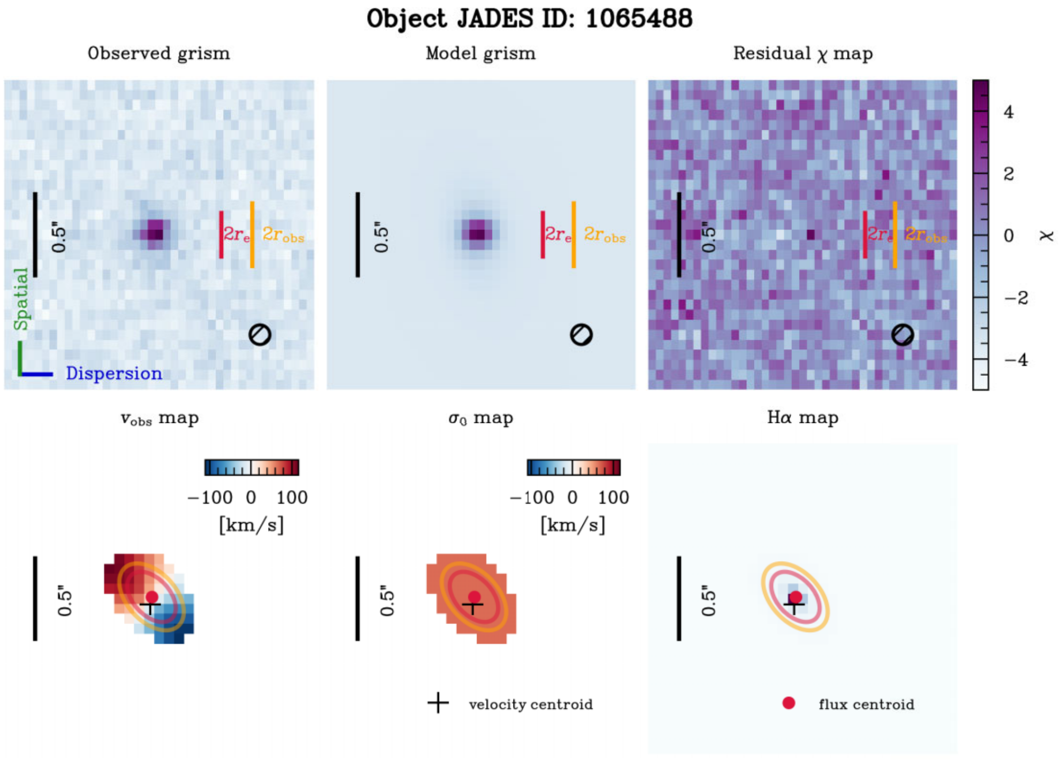

Figure G1. – *continued*

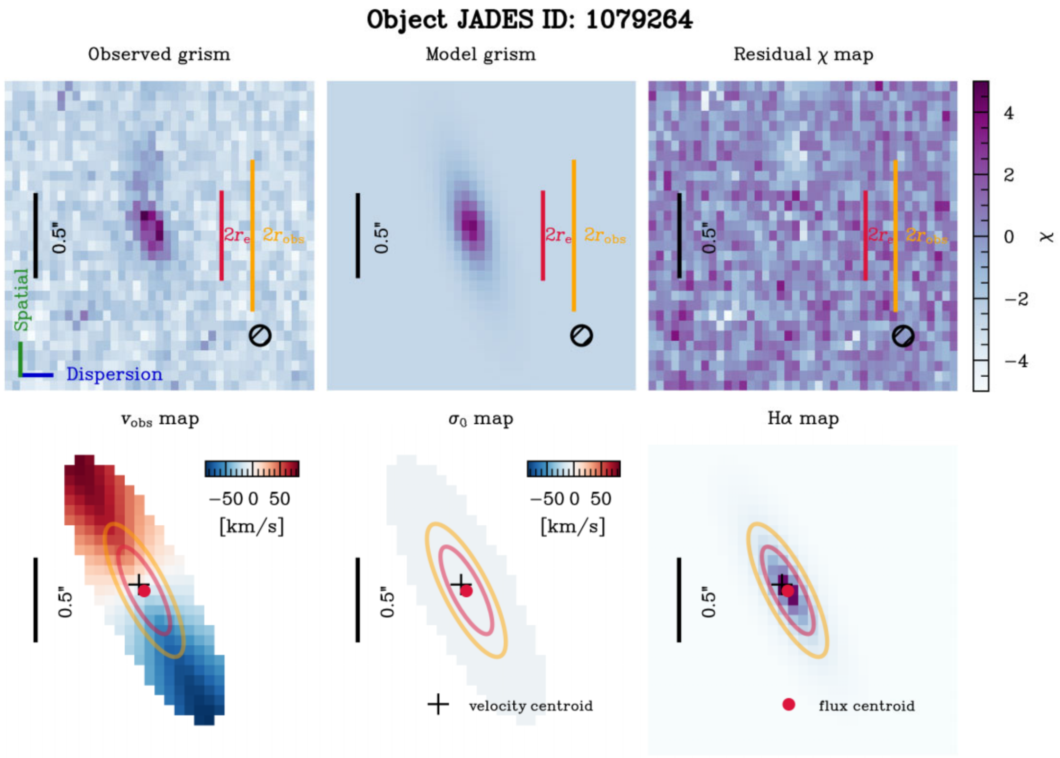

Figure G1. – *continued*

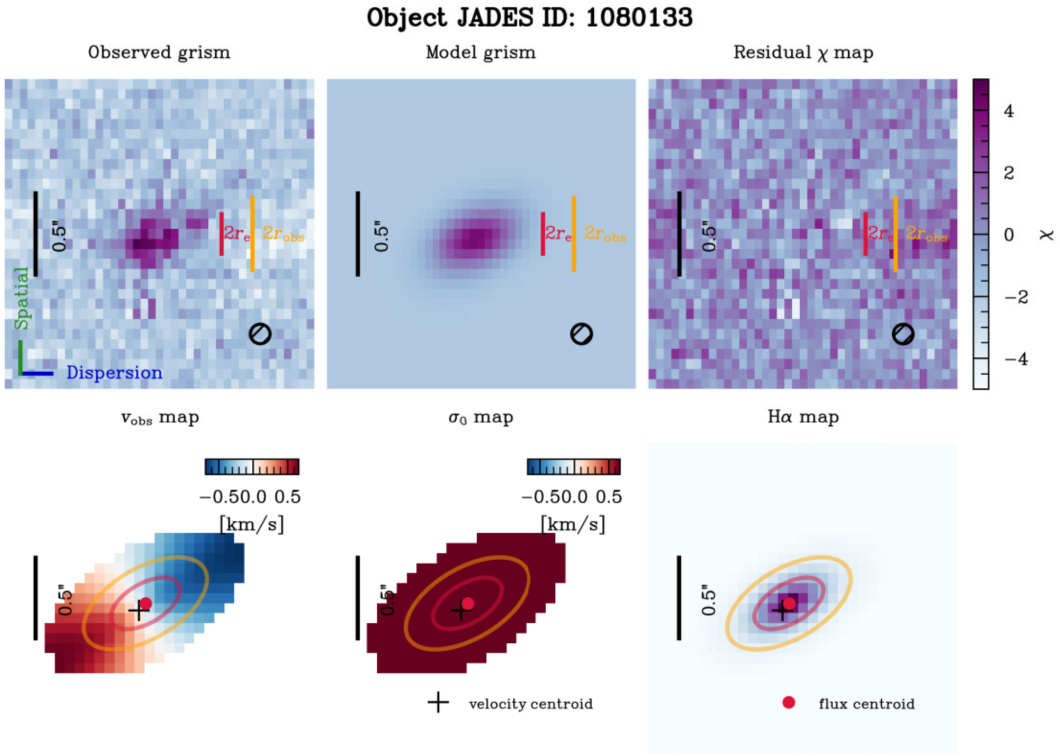

Figure G1. – *continued*

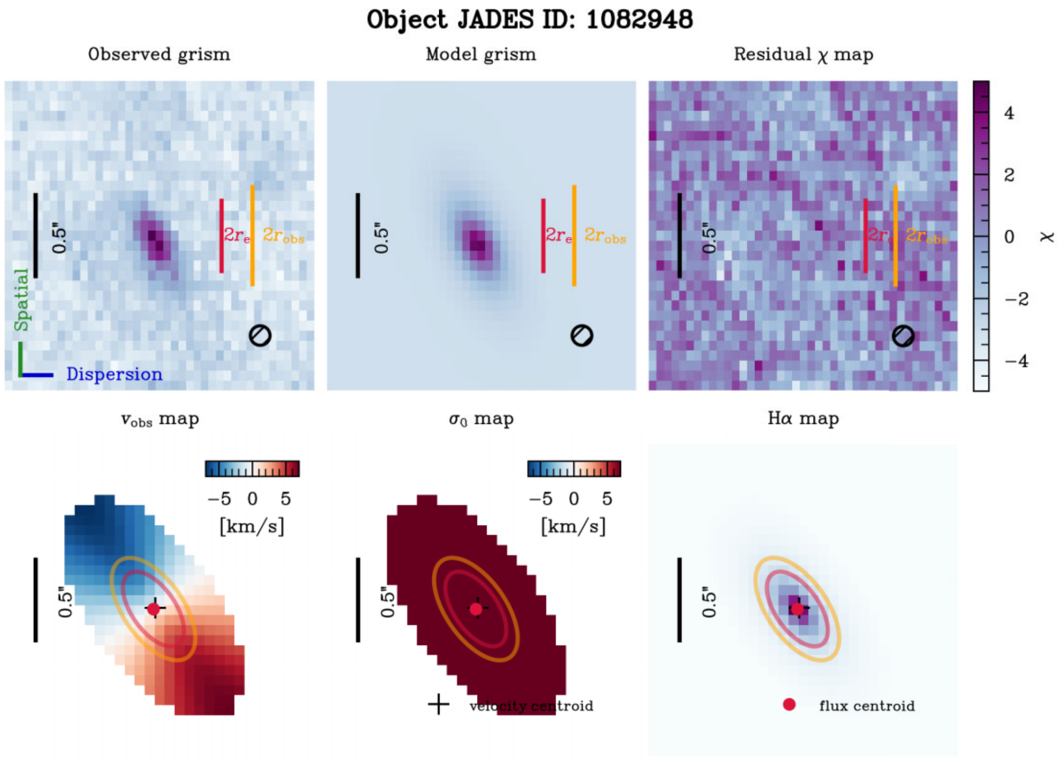

Figure G1. – *continued*

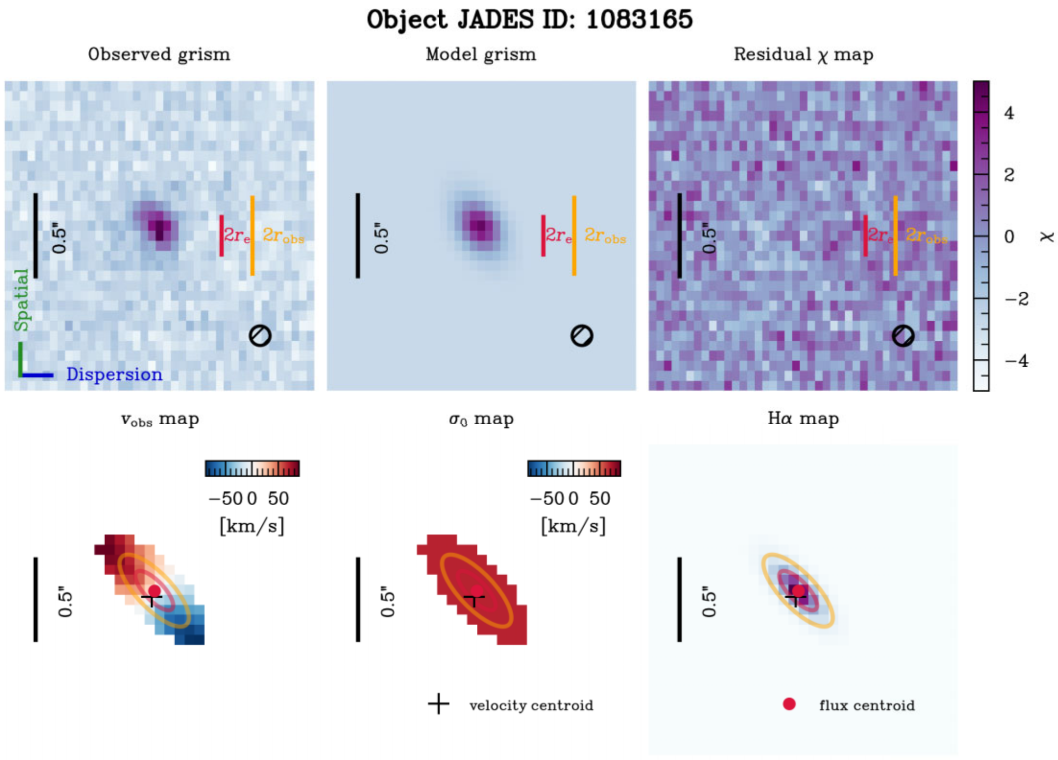

Figure G1. – *continued*

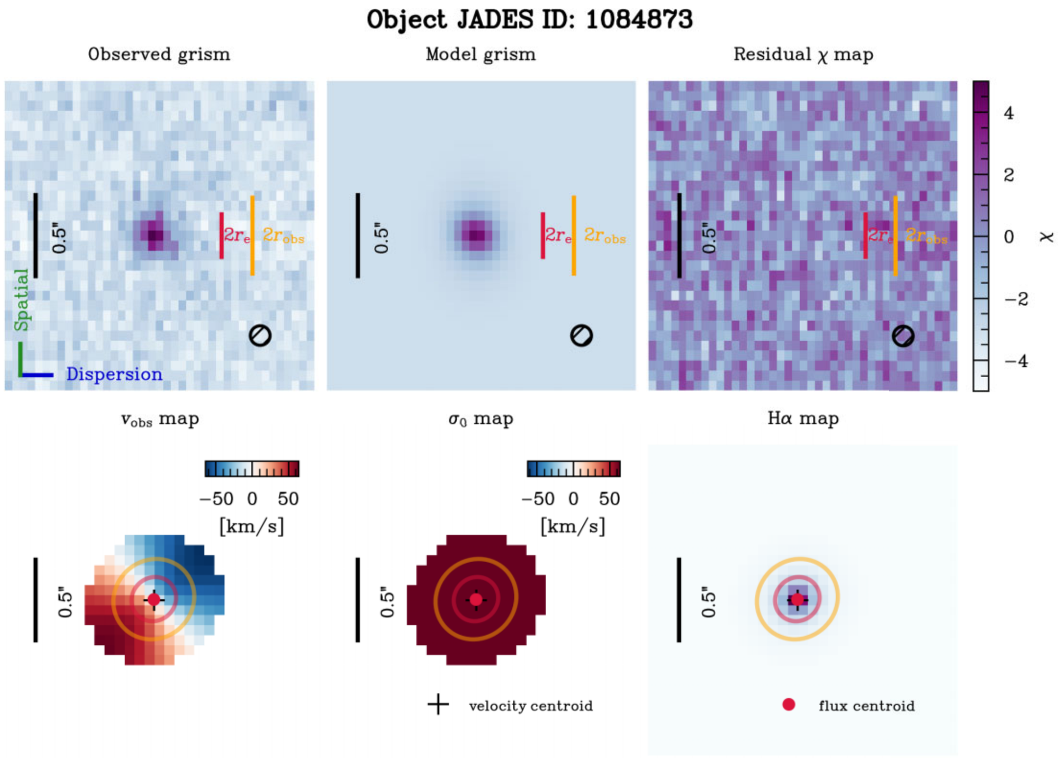

Figure G1. – *continued*

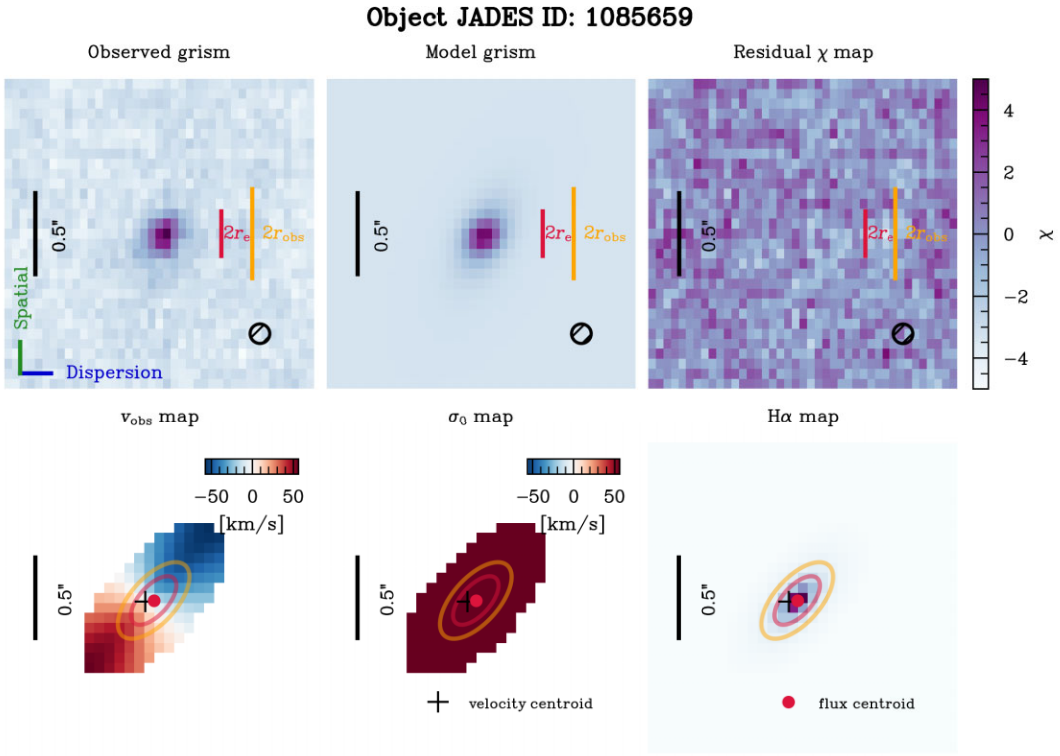

Figure G1. – *continued*

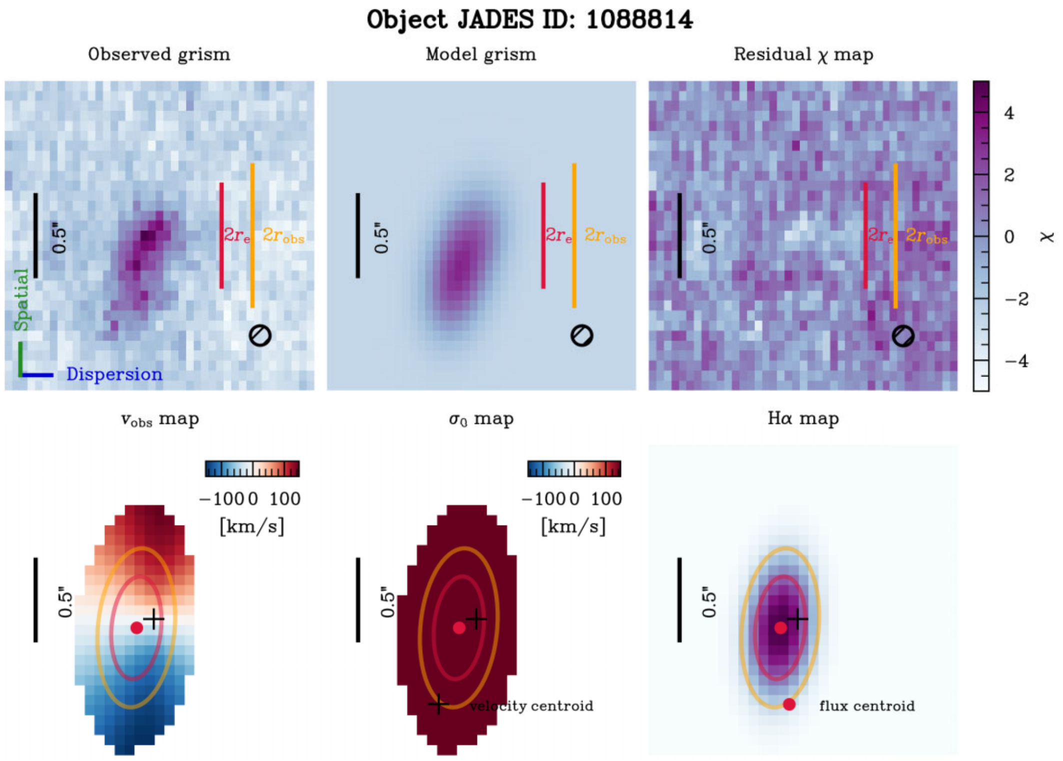

Figure G1. – *continued*

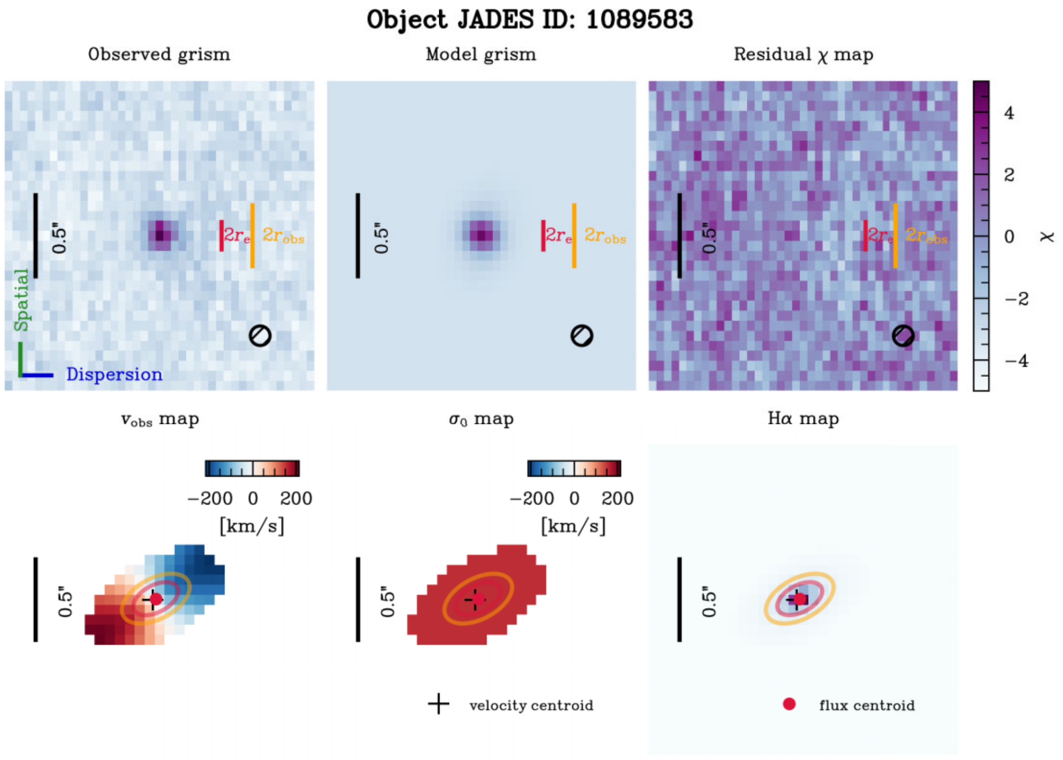

Figure G1. – *continued*

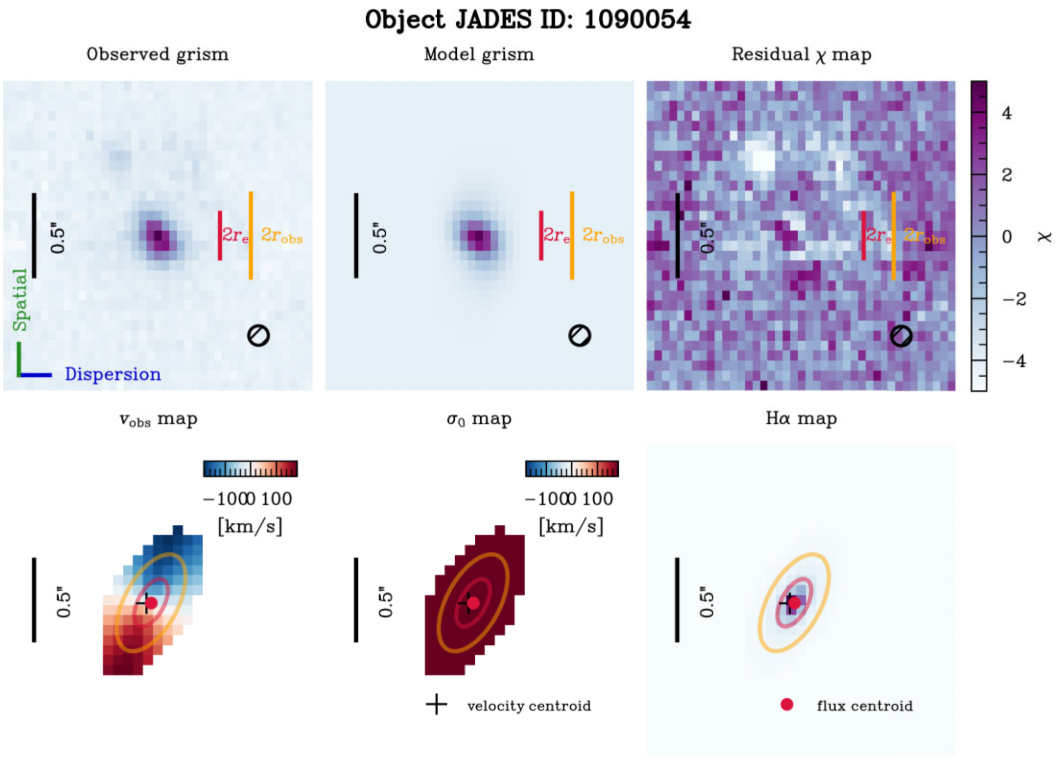

Figure G1. – *continued*

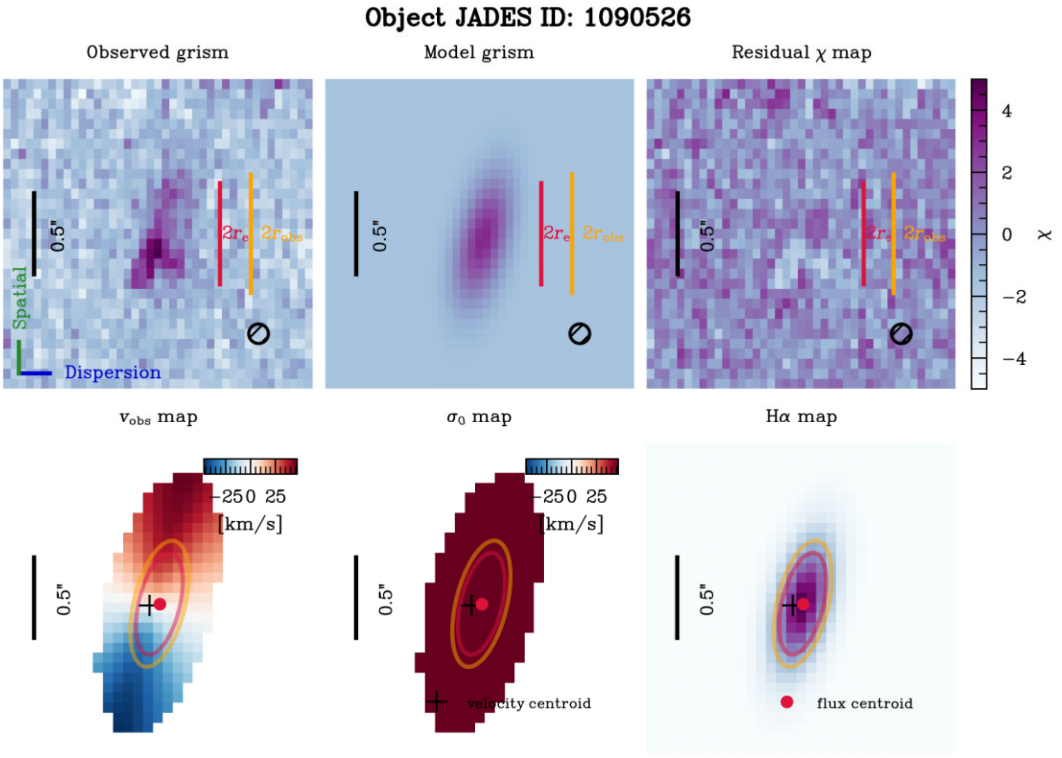

Figure G1. – *continued*

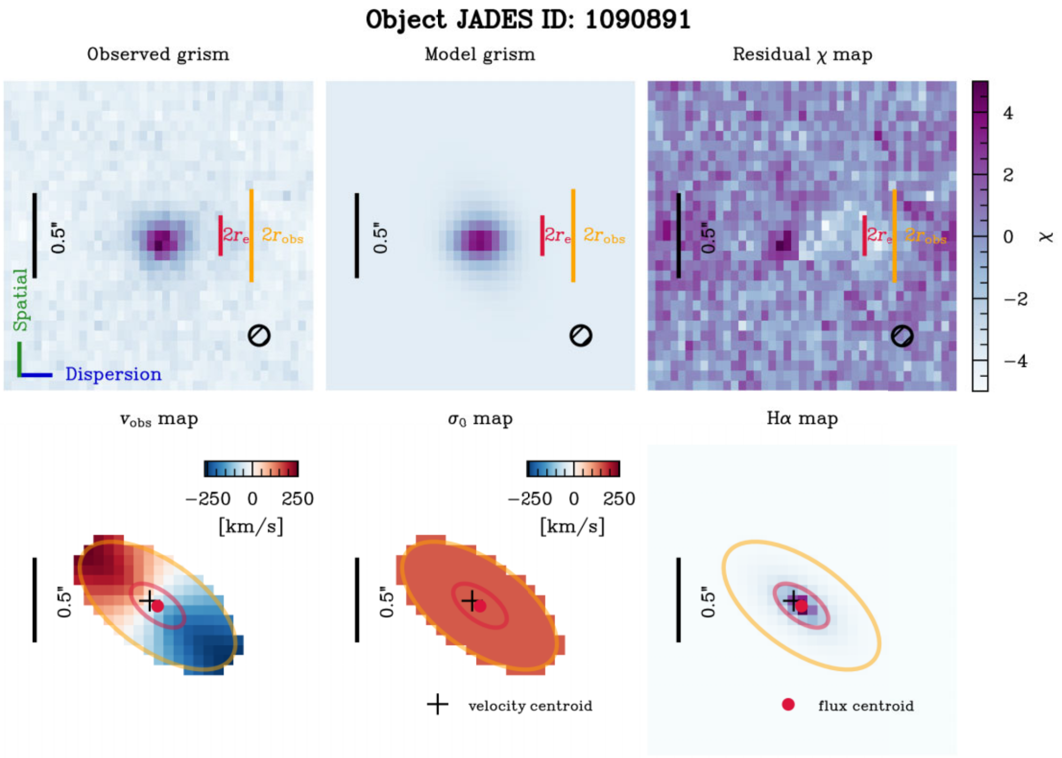

Figure G1. – *continued*

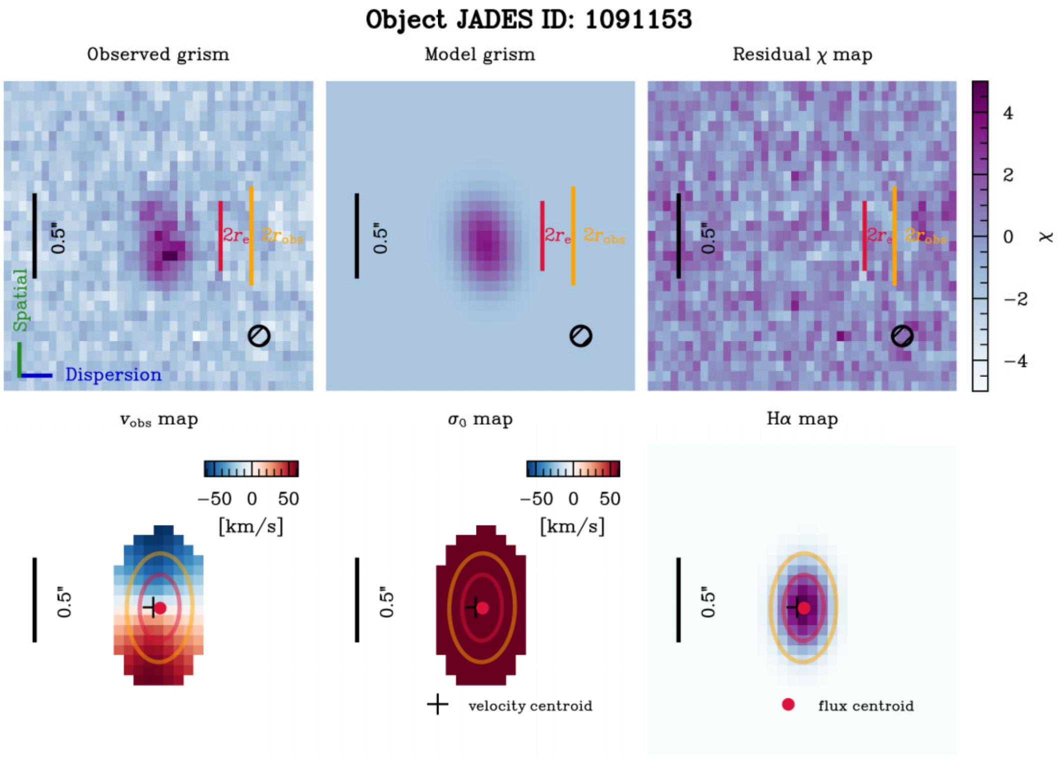

Figure G1. – *continued*

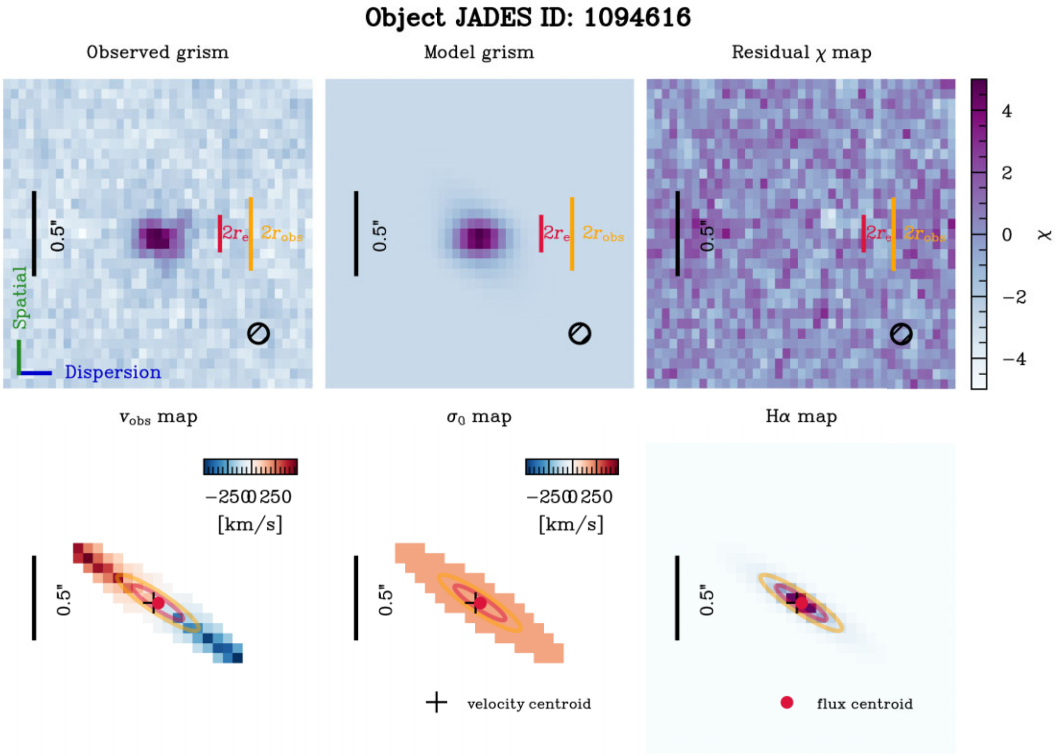

Figure G1. – *continued*

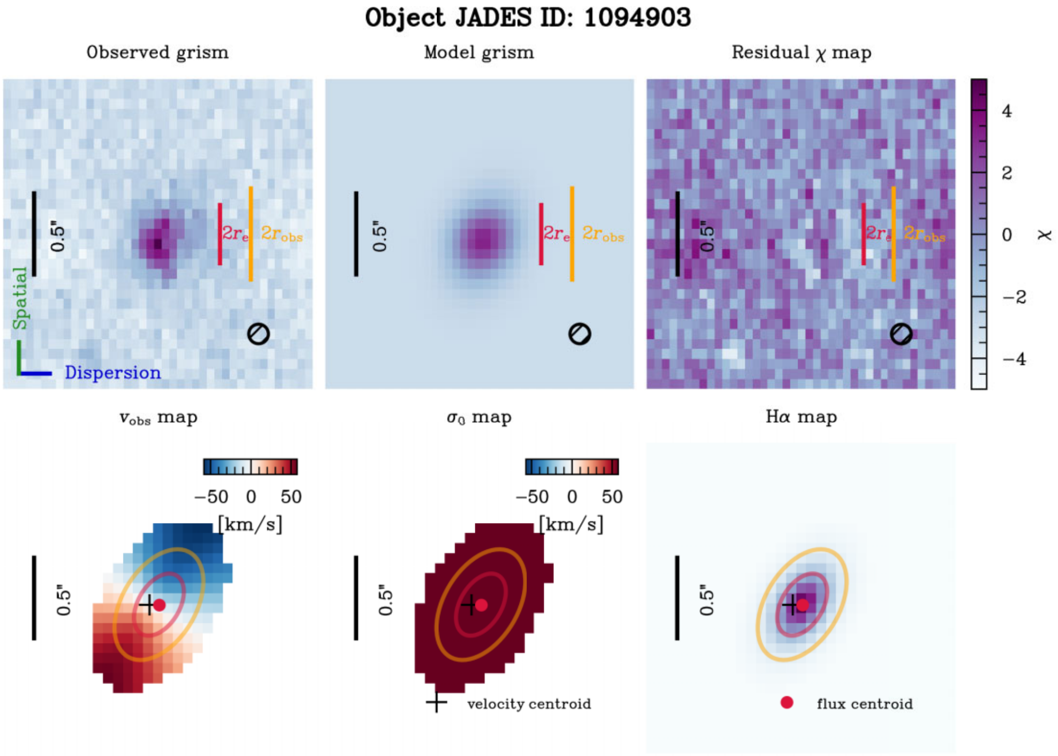

Figure G1. – *continued*

This paper has been typeset from a TEX/LATEX file prepared by the author.